UNIVERSIDAD DE INVESTIGACIÓN DE TECNOLOGÍA EXPERIMENTAL YACHAY

Escuela de Ciencias Físicas y Nanotecnología

TÍTULO: The Electronic Structure of the Magnetite Fe_3O_4 (100) Surface: Implications for the Fabrication of Fe_3O_4 Nanoparticles

Trabajo de integración curricular presentado como requisito para la obtención del título de Ingeniero en Nanotecnología

Autor:

Tipán Quishpe Byron Xavier

Tutor:

P.h.D. Henry Pinto

Urcuquí, agosto 2019

Urcuquí, 28 de agosto de 2019

SECRETARÍA GENERAL
(Vicerrectorado Académico/Cancillería)
ESCUELA DE CIENCIAS FÍSICAS Y NANOTECNOLOGÍA
CARRERA DE NANOTECNOLOGÍA
ACTA DE DEFENSA No. UITEY-PHY-2019-00018-AD

En la ciudad de San Miguel de Urcuquí, Provincia de Imbabura, a los 28 días del mes de agosto de 2019, a las 09:00 horas, en el Aula Sala Capitular de la Universidad de Investigación de Tecnología Experimental Yachay y ante el Tribunal Calificador, integrado por los docentes:

Presidente Tribunal de Defensa	Dr. MEDINA DAGGER, ERNESTO ANTONIO, Ph.D.
Miembro No Tutor	Dr. MOWBRAY , DUNCAN JOHN , Ph.D.
Tutor	Dr. PINTO ESPARZA, HENRY PAUL , Ph.D.

Se presenta el(la) señor(ita) estudiante TIPAN QUISHPE, BYRON XAVIER, con cédula de identidad No. 1723405955, de la ESCUELA DE CIENCIAS FÍSICAS Y NANOTECNOLOGÍA, de la Carrera de NANOTECNOLOGÍA, aprobada por el Consejo de Educación Superior (CES), mediante Resolución RPC-SO-13-No.156-2015, con el objeto de rendir la sustentación de su trabajo de titulación denominado: The Electronic Structure of the Magnetite Fe3O4 (100) Surface: Implications for the Fabrication of Fe3O4 Nanoparticles, previa a la obtención del título de INGENIERO/A EN NANOTECNOLOGÍA.

El citado trabajo de titulación, fue debidamente aprobado por el(los) docente(s):

Tutor	Dr. PINTO ESPARZA, HENRY PAUL , Ph.D.

Y recibió las observaciones de los otros miembros del Tribunal Calificador, las mismas que han sido incorporadas por el(la) estudiante.

Previamente cumplidos los requisitos legales y reglamentarios, el trabajo de titulación fue sustentado por el(la) estudiante y examinado por los miembros del Tribunal Calificador. Escuchada la sustentación del trabajo de titulación, que integró la exposición de el(la) estudiante sobre el contenido de la misma y las preguntas formuladas por los miembros del Tribunal, se califica la sustentación del trabajo de titulación con las siguientes calificaciones:

Tipo	Docente	Calificación
Presidente Tribunal De Defensa	Dr. MEDINA DAGGER, ERNESTO ANTONIO, Ph.D.	10,0
Miembro Tribunal De Defensa	Dr. MOWBRAY , DUNCAN JOHN , Ph.D.	9,6
Tutor	Dr. PINTO ESPARZA, HENRY PAUL , Ph.D.	10,0

Lo que da un promedio de: 9.8 (Nueve punto Ocho), sobre 10 (diez), equivalente a: APROBADO

Para constancia de lo actuado, firman los miembros del Tribunal Calificador, el/la estudiante y el/la secretario ad-hoc.

TIPAN QUISHPE, BYRON XAVIER
Estudiante

Dr. MEDINA DAGGER, ERNESTO ANTONIO, Ph.D.
Presidente Tribunal de Defensa

Dr. PINTO ESPARZA, HENRY PAUL , Ph.D.
Tutor

Dr. MOWBRAY , DUNCAN JOHN , Ph.D.
Miembro No Tutor

CIFUENTES TAFUR, EVELYN CAROLINA
Secretario Ad-hoc

Autoría

Yo, **BYRON XAVIER TIPAN QUISHPE**, con cédula de identidad 1723405955, declaro que las ideas, juicios, valoraciones, interpretaciones, consultas bibliográficas, definiciones y conceptualizaciones expuestas en el presente trabajo; así cómo, los procedimientos y herramientas utilizadas en la investigación, son de absoluta responsabilidad de el/la autora (a) del trabajo de integración curricular. Así mismo, me acojo a los reglamentos internos de la Universidad de Investigación de Tecnología Experimental Yachay.

Urcuquí agosto 2019.

BYRON XAVIER TIPAN QUISHPE

CI:1723405955

Autorización de Publicación

Yo, **BYRON XAVIER TIPAN QUISHPE**, con cédula de identidad 1723405955, cedo a la Universidad de Tecnología Experimental Yachay, los derechos de publicación de la presente obra, sin que deba haber un reconocimiento económico por este concepto. Declaro además que el texto del presente trabajo de titulación no podrá ser cedido a ninguna empresa editorial para su publicación u otros fines, sin contar previamente con la autorización escrita de la Universidad.

Asimismo, autorizo a la Universidad que realice la digitalización y publicación de este trabajo de integración curricular en el repositorio virtual, de conformidad a lo dispuesto en el Art. 144 de la Ley Orgánica de Educación Superior

Urcuquí, agosto 2019.

BYRON XAVIER TIPAN QUISHPE

CI:1723405955

Acknowledgements

First of all, I am grateful for my mother, Mayra Quishpe, for showing me all the love a mother can have for her son, the courage to get ahead in difficult times and the inspiration to be a great person.

To my grandparents, María Beatriz Ballagán and Juan Quishpe, thanks for all the love and good lessons I have received from them.

To my aunts, Angela, Gulnara del Pilar, and Cristina thanks for being great examples of strong, determined and loving women. Great daughters and mothers who always knew how to give me excellent advice and love.

To my brothers and sisters Ximena, Yomara, Alex and Marco, to my cousins, Juan, Santiago, Bruno, and Nicolás, to my nephew Leandro thanks for all the beautiful moments we have had growing up together.

To Ph.D. Henry P. Pinto for giving me all his knowledge to carry out this project, for his words of encouragement and his confidence in me to achieve great results thank you very much.

To Ph.D. Gema Gonzáles for being a great teacher, advisor, and person who motivated me during all the work, who offered support and above all confidence in me thank you very much.

To my classmates, Vanessa Hinojosa, Cristian Proaño and Cristhian Chingo, for always being in the difficult moments and in those moments full of joy I show you all my gratitude.

To my best friend Shary Mosquera, to my boyfriend Jeanpierre Pilataxi, I thank you for showing me the true meaning of love.

To my friends among them: Natasha Jurado, Alex Galarraga, Gloria Ordóñez, Patricia Rengel, Maria Jose Ayala, Cristian Guzman, Paul Alvarado, Carlos Lopez, Robin Paspuel, Dario Castro, Fabián Puga, Cristian Salas, and Alex Escobar. My most sincere thanks for your friendship.

Finally, I would like to acknowledge the generous computing provided by Supercomputer QUINDE I of Yachay EP thought the grant "Multiscale Modeling of Materials " and Ing. Fabian Jimenez for all the technical support when using QUINDE.

Resumen

La Magnetite (Fe$_3$O$_4$) es un fascinante óxido metálico de transición ferrimagnético (FiM) que muestra una transición de metal-aislante de primer orden (Verwey) a la temperatura T$_V$ ∼ 121 K por debajo de la cual el cristal cambia su simetría de estructura cúbica *Fd$\bar{3}$m* a una simetría ortormbica *Pmca*. Estudios recientes sugieren que el inicio de esta transición es un efecto del ordenamiento de carga que induce la formación de localización de electrones dentro de la red que sufre una distorsión de Jahn-Teller. El estudio de las superficies de Fe$_3$O$_4$ también es de interés científico, ya que tanto la carga como los efectos de ordenación orbital pueden estar presentes incluso a temperatura ambiente. Esos efectos, junto con las propiedades magnéticas de la superficie y la presencia de defectos como el oxígeno o las vacantes de hierro, podrían desempeñar un papel fundamental en la manipulación atómica de este material para aplicaciones tecnológicas interesantes como sensores, espintrónica, prensas de resonancia magnética ultrasensibles y aplicaciones biomédicas. Los cálculos de estructura electrónica utilizando la teoría de densidad funcional (DFT) brindan una herramienta poderosa para investigar las propiedades de las superficies de Fe$_3$O$_4$ (100) a nanoescala. Este estudio considerará todas las posibles terminaciones superficiales del hierro, incluidas las vacantes de oxígeno. Estos cálculos DFT serán capaces de predecir la estructura y energía de la superficie/interfaz, las propiedades magnéticas, la espectroscopía fotoelectrónica ultravioleta (UPS) y la microscopía de efecto tunel (STM). Los resultados obtenidos se discutirán a la luz de los datos experimentales disponibles. Experimentalmente, la síntesis de nanopartículas de magnetita (MNP) se realizó con el fin de correlacionar los datos experimentales y de simulación. La síntesis de MNP se llevó a cabo mediante un proceso químico húmedo y se caracterizó por microscopía electrónica de transmisión (TEM). Finalmente, los datos experimentales se compararon con los datos computacionales para comprender la orientación de las nanopartículas, la energía de los electrones en la superficie y su estructura atómica.

Palabras Clave: Teoría Funcional de la Densidad, Transición de Verwey, Material Ferrimagnético, Coprecipitación Química, Estabilidad de la Superficie.

Abstract

Fe_3O_4 is a fascinating ferrimagnetic (FiM) transition metal-oxide that shows first-order metal-insulator (Verwey) transition at temperature $T_V \sim 121$ K below which the crystal changes its symmetry from cubic $Fd\bar{3}m$ to orthorhombic structure $Pmca$. Recent studies suggest that the onset of this transition is a charge-ordering effect that induces the formation of electron localization within the lattice that undergoes a Jahn-Teller distortion. The study of Fe_3O_4 surfaces is also of scientific interest since both charge and orbital ordering effects might be present even at room temperature. Those effects together with the surface magnetic properties and the presence of defects like oxygen or iron vacancies could play a fundamental role towards the atomic manipulation of this material for interesting technological applications such as sensors, spintronics, ultrasensitive magnetic-resonance probes and biomedical applications. Electronic structure calculations using density-functional theory (DFT) provide a powerful tool to investigate the properties of $Fe_3O_4(100)$ surfaces at the nanoscale. This study will consider all the possible surface terminations of iron including oxygen vacancies. These DFT calculations will be capable of predicting the surface/interface structure and energy, magnetic properties, simulated ultraviolet photoelectron spectroscopy (UPS) and scanning tunneling microscopy (STM). The obtained results will be discussed in the light of available experimental data. Experimentally, the synthesis of magnetite nanoparticles (MNPs) was done in order to correlate experimental and simulation data. The synthesis of MNPs was carried out through a wet chemical process and characterized by transmission electron microscopy (TEM). Finally, the experimental data were compared with the computational data to understand the orientation of the nanoparticles, energy of the electrons in the surface and their atomic structure.

Keywords: Density functional theory, Verwey transition, Ferrimagnetic material, Chemical co-precipitation, Surface Stability.

Contents

List of Figures

List of Tables

Chapter 1

Introduction

Magnetite (Fe_3O_4) has been studied for many years since its discovery 2500 years ago by Thales of Miletus.[1] Fe_3O_4 is part of a group of oxides called transition metal oxides (TMOs). In general terms, the TMOs have some electronic properties related to external d-electrons.[2] Some of them show metallic character, load density wave, charge ordering, defects of order, superconductivity among others.[3] A few interesting applications of this group of oxides are eco-friendly energy storage, components in catalysis, gas sensors, resistance random access memory and others.[4–7] However, Fe_3O_4 is a complex material which our knowledge and motivates a deep study of its structural and electronic properties.

The crystal structure of Fe_3O_4 has a composition of Fe^{2+} and Fe^{3+} cations that are surrounded by oxygen anions. Fe_3O_4 below 858 K is a ferrimagnetic (FiM) material that crystallizes in a cubic structure with $Fd\bar{3}m$ symmetry. However, Fe_3O_4 experiences a charge ordering (CO) around 121 K due to the phenomenon so-called the Verwey transition.[8] This transition occurs due to a change in the symmetry of the crystal lattice and the electrical conductivity. The temperature at which Fe_3O_4 undergoes this transition is called the Verwey temperature (T_V).[9] Under T_V, Fe_3O_4 suffers a first-order phase transition, where its electrical conductivity decreases by two orders of magnitude.[1] This phenomenon is due to ordering in its crystalline structure where some cations of Fe are re-ordered to change its symmetry to a monoclinic $P2/m$ symmetry cell with orthorhombic *Pmca* pseudosymmetry constraints on the atomic positions.[10]

The density-functional theory (DFT) is a valuable computational tool in the study of many body systems in atomic, molecular and solid state physics.[11] DFT is based on introducing an electronic correlation using functional electronic density. The concept of functional is explained as a function whose domain is

represented by a set of functions. This theory uses the Honenberg-Kohn theorem in which it is shown that the ground state energy and electronic density is determined by a single functional. According to Kohn and Sham, the electronic energy can be expressed as a sum of several terms which can be represented as functions of electronic density.[12] One of these important terms is the exchange and correlation (XC) energy. The precision of the DFT calculations is based on the choice of XC functionals and the integrity of the set of bases, while the efficiency of the same refers to the numerical algorithms used. John Perdew described a hierarchy of XC functionals where shows that the generalized gradient approximation (GGA) implies an E_{XC} dependent on the electronic density as well as its local gradient.[13]

Certain simulation studies in DFT have been carried out to explain properties of Fe_3O_4 such as Verwey transitions, segregation, structural properties, stability adsorption and redox behavior among others.[14-16] Li *et al*. shows a detailed study of the structure, stability, and magnetic properties for Fe_3O_4 (110) surfaces using DFT calculations. The results obtained from the density of states (DOS) of each type of surface modeled are compared between them.[17] Similarly, Zhu *et al*. develops a similar study for Fe_3O_4 (111) surfaces with some variations in their DFT calculations.[18] Other investigations deepen the study of Verwey's transition and CO. Piekarz *et al*. uses a group of theoretical models to reproduce the total energy of the system, magnetic moments and band gap of Fe_3O_4 with symmetry $Fd\bar{3}m$ and $P2/c$.[19] In general, DFT calculations have proven to be a great tool for the study of this material.

Experimentally, Fe_3O_4 has been synthesized in the form of magnetite nanoparticles (MNPs) using various types of growth methods at the same time they have been characterized using different types of techniques. Some of these synthesis methods are the high-temperature solution-phase reaction, co-precipitation, hydrothermal process, and even green synthesis.[20-25] The size and morphology of the MNPs have been determined by transmission electron microscopy (TEM)[26] at the same time the atomic structure is documented through scanning tunneling microscopy (STM) , and the binding energies of electrons in a surface are determined by ultraviolet photoelectron spectroscopy (UPS).[27-29]

The study of surfaces through DFT calculations have shown a relationship in the synthesis of MNPs. A clear example is the research carried out by Andrés *et al*. In this exhaustive work an understanding of the formation of Ag nanoparticles based on his superficial energy.[30] Using DFT results, it is possible to predict the type of surface that would be expected to be obtained in the synthesis of MNPs.

This work has been organized according to the following structure. First, chapter 2 presents a brief review of key concepts in the study of Fe_3O_4 while chapter 3 shows the computational and experimental methodologies applied in this work, and chapter 4 presents the results obtained from the last section and

the discussion of them. Finally, the conclusions and outlook are presented in chapter 5.

1.1 Problem Statement

DFT calculations for Fe_3O_4 have provide reliable predictions in recent years. However, this novel material has not been fully understood in terms of its electronic and magical properties. The Verwey transition is a clear example of the importance of understanding the electronic and magnetic properties of magnetite. The metallic or insulating character is strongly linked to the morphology and properties previously defined. At the same time, these properties can directly influence the synthesis of MNPs in order to predict their morphology, surface stability, energy of bond between Fe and O, among other characteristics of the material.

1.2 General and Specific Objectives

Study the structural and electronic properties of the different types of $Fe_3O_4(100)$ surfaces using DFT calculations.

- Understand the structural and electronic properties of bulk Fe_3O_4 using DFT calculations.

- Model $Fe_3O_4(100)$ surfaces with different types of vacancies of reconstructions that includes surface oxygen vacancies and iron termination.

- Analyze the differences between the electronic and structural properties of the surfaces according to the types of oxygen vacancies and iron terminations.

- Evaluate surface stability for each $Fe_3O_4(100)$ surfaces modeling case.

- Generate the UPS spectra STM images of the different types of $Fe_3O_4(100)$ surfaces.

- Finding a correlation between the experimental results of the synthesis of MNPs, results of previous research and the simulations using DFT.

Chapter 2

Theoretical Background

2.1 Ferromagnetic Order

Magnetism is a direct consequence of the non-zero spin associated of the electrons. According to Néel, there are several types of magnetic substances which are diamagnetic, paramagnetic, ferromagnetic and ferrimagnetic. The paramagnetic (diamagnetic) materials generate an induced magnetic field in the (opposite) direction of the external magnetic field.[31]
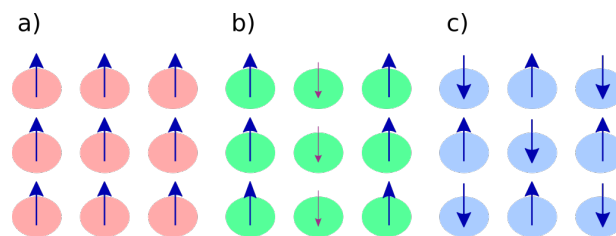
Figure 2.1: Possible ordered arraignment of electron spines. The spheres represent ordered atoms while the blue and purple arrows represent the spin direction of the electrons. Schematics of a) ferromagnetic and b) ferrimagnetic states, and c) antiferromagnetic non-magnetic state.

In Figure 2.1, the ferromagnetic (FM) state is one in which the spins of all the electrons point in the same direction. The magnetic moment is the average of electron spins per atom. A particular case is ferrimagnetism. This phenomenon is evident in complex compounds such as some metal oxides. In ferrimagnetism, the magnetic moments are organized in an antiparallel orientation; however, there is a net

magnetization due to the difference in magnitude between them. The net magnetization of ferrimagnetic (FiM) materials is lower than FM materials. The antiferromagnetic (AFM) state indicates that the spins of the electrons are pointing in the opposite way between atoms.[31] However, Néel proposes that an AFM material could become a paramagnetic material at a certain temperature because the thermal energy is strong enough to energetically overcome the magnetic order of the material.[32]

2.2 The Magnetite Crystal

Spinel structures are compounds where divalent and trivalent cations are found surrounded by oxygen atoms in a cubic sublattice. The general formula of these compounds is AB_2O_4. An important type of magnetic materials are the spinel ferrites. These are compounds with the general formula $MeFe_2O_4$, where Me represent a metal element. In these compounds, there are two important crystallographic sites. The tetrahedral A-sites are surrounded by 4 oxygen atoms while the octahedral B-sites are surrounded by 8 oxygen atoms. The normal spinel is a type of this material in which the Me^{2+} ions occupy the tetrahedral sites while the M^{3+} ions occupy the octahedral sites. In the opposite case, Me^{2+} and Me^{3+} ions occupy the octahedral and tetrahedral sites, respectively. These materials are the inverse spinels. A very interesting case is the mixed spinel where the two ions appear in the two sites A and B.[31]

Magnetite (Fe_3O_4) is an inverse spinel crystal that belongs to a group of substances called transition metal oxides (TMOs). Fe_3O_4 plays an important role in the study of magnetism. Fe_3O_4 was the essential material to understand the model of ferromagnetism studied by Néel.[1] According to Néel, a FiM material is subject to the interaction between magnetic atoms that are aligned antiparallel. However, these interactions are not equal; *i.e.*, there is a net magnetization despite the AFM configuration. Three factors explain this type of phenomena: differences in magnetic atoms, different types of crystallographic sites, and both in combination.[33] For Fe_3O_4, the FiM order is expressed below the Neel's temperature T_N= 860 K.[34]

Above T = 121 K, Fe_3O_4 is a metallic iron oxide formed by a mixture of Fe^{2+} and Fe^{3+} ions.[36] In Figure 2.2, Fe_3O_4 crystallizes as an inverse spinel structure with a spatial group $Fd\bar{3}m$ with a lattice parameter of 8.396 Å.[8] The oxygen anions form a face-centered cubic (fcc) sublattice where the Fe cations are located in interstitial spaces. The Fe cations are distributed in two configurations within the crystal. The Fe^{3+} cations occupy the tetrahedral coordination sites A, Fe_A, while Fe^{2+} and Fe^{3+} cations occupy the octahedral coordination sites B, Fe_B, in equal proportion.[37] According to Néel's theory of FiM, the Fe^{3+} ions have 5 unpaired electrons, so that it has a magnetic moment of +5 μ_B; whereas the Fe^{2+} ions
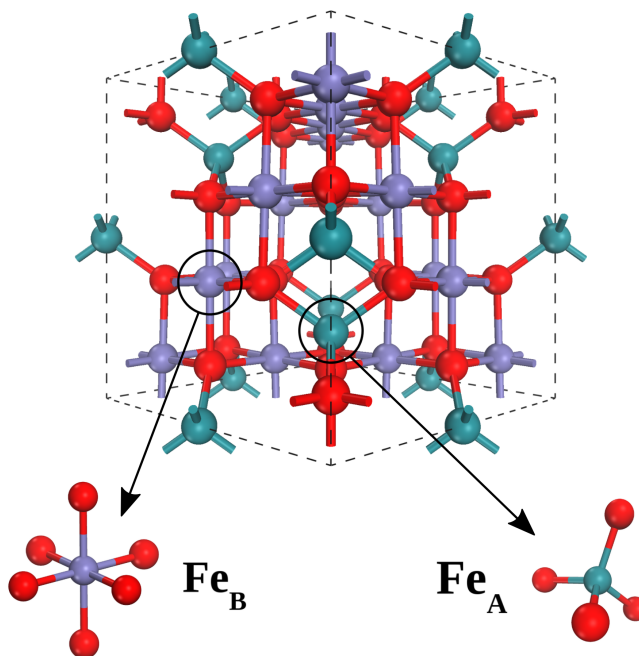
Figure 2.2: The crystal structure of Fe_3O_4 described as a cubic packing with symmetry $Fd\bar{3}m$.[35] The red spheres represents the oxygen ion, arranged in a fcc sublattice, while the green (blue) spheres denotes the iron atoms occupying the tetrahedral (octahedral) site Fe_A (Fe_B)

have 4 unpaired electrons, so that it has a magnetic moment of 4 μ_B. However, the position of the ions determines the sign of the contributions. The Fe^{3+} cation has a sign variation in its magnetic contribution. Fe_A^3 contribute $-5\mu_B$ while Fe_B^3 contribute $+5\mu_B$ to the magnetic moment, whereas the Fe^{2+} cation always contributes $+4\mu_B$. Therefore, according to Neel's rules, the total magnetic moment of a unit cell of Fe_3O_4 will be $+4\mu_B$ per formula unit.[31]

An important property of Fe_3O_4 is the change in symmetry that it undergoes at 121 K. Under these conditions, the Verwey transition of spinel structure of high temperature ($Fd\bar{3}m$)[8] suffers a phase transition where it drops its symmetry to an orthorhombic *Pmca* symmetry[10]. This structural change in Fe_3O_4 induces a significant drop in its conductivity by two orders of magnitude.[38] Figure 2.3 shows the experimental measurements of Fe_3O_4 conductivity at different temperatures. This observation inspired Verwey to propose a transition of order-disorder in an ionic model. This model explains that above the Verwey
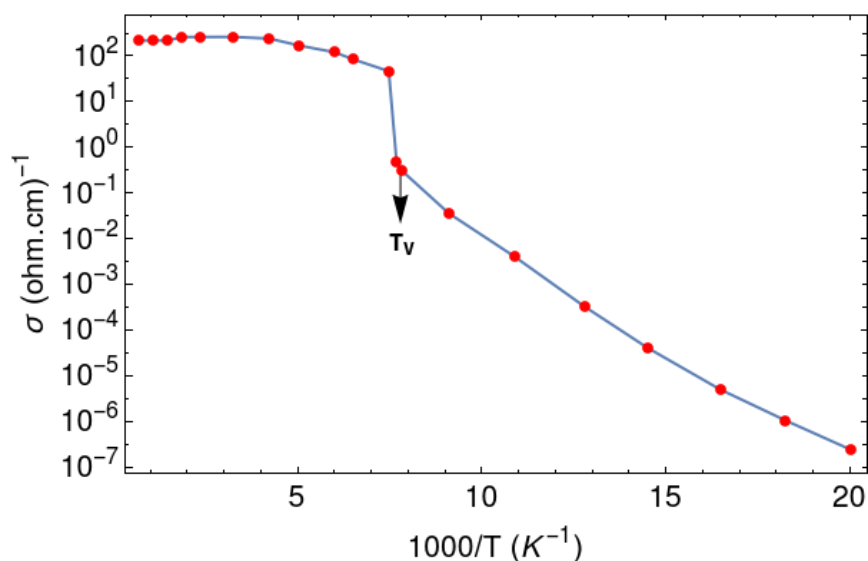
Figure 2.3: Verwey Transition for Fe_3O_4. Around 125 K there is a decrease two orders of magnitude of its electrical conductivity. Adapted from Ref. 9.

temperature (T_V) the ions Fe^{3+} and Fe^{2+} experience a dynamic disorder. Below T_V, the ions of Fe^{3+} and Fe^{2+} are ordered, thus the electrons reduce their mobility.[1] Nevertheless, this model of charge ordering (CO) is not sufficiently precise to explain the complete behavior of Fe_3O_4 with the temperature. One of the most compelling pieces of evidence for this is found in nuclear magnetic resonance. The Mössbauer probes for hyperfine iron fields, show more than two intermediate load states are associated with temperatures below 121 K. This means the idea of a single unique 3d state for transitional oxides is not a viable description for these systems.[16]

Considering possible technological applications, Fe_3O_4 is a material of great interest in the field of biomedicine and the science of materials.[39–41] A clear example is the functionalization of magnetite nanoparticles (MNPs) for the use *in vivo* and *in vitro* applications. MNPs are an interesting alternative for conventional biolabels.[42] According to recent research, Wang *et al.* have proposed the use of ultrasensitive magnetic microarrays to identify the binding sites of DNA and certain proteins. The sensor is capable of detecting the change in the electrical resistance produced by magnetic nanoparticles of a single magnetic domain.[43] Additionally, the creation of magnetic nanocomposites using Fe_3O_4 is also a broad field of research.[44–47] Sen *et al.* proposed a novel method for the fabrication of a magnetic mesoporous silica-Fe_3O_4 nanocomposite. This nanocomposite functions as a specific magnetic separator because it can bind

or elude DNA while extracting RNA from bacteria.[48] However, Fe_3O_4 does not only have applications in biomedicine, but also much research has been conducted with the purpose of exploiting the properties of Fe_3O_4. According to Rajput *et al.*, MNPs can be used to absorb chromium and lead in water using their magnetic properties, high surface area, chemical stability, easy synthesis, and low toxicity.[49] All this research demonstrates the need to fully understand Fe_3O_4 as one of the most important magnetic materials.

2.3   Density Functional Theory

Density-functional theory (DFT) is a powerful method for studying the electronic structure of many-body systems such as atoms, molecules, and compounds among others. The importance of this theory lies in its practical and successful application to quantum mechanics. For this reason, it is necessary to understand the Schrödinger equation. The nonrelativistic time-independent case presents a simplified form for this equation, that is, $H\Psi = E\Psi$; where, H and Ψ represent the Hamiltonian operator and the wavefunction, respectively. For a system comprised of N electrons and M nuclei, the Schrödinger equation is

$$\left[-\frac{\hbar^2}{2m} \sum_i \nabla_i^2 + \frac{1}{2} \sum_{i \neq j} \frac{e^2}{|\mathbf{r_i} - \mathbf{r_j}|} - \sum_{i,I} \frac{e^2 Z_I}{|\mathbf{r_i} - \mathbf{R_I}|} - \frac{\hbar^2}{2} \sum_I \frac{\nabla_I^2}{M_I} + \frac{1}{2} \sum_{I \neq J} \frac{e^2 Z_I Z_J}{|\mathbf{R_I} - \mathbf{R_J}|} \right] \Psi = E\Psi, \qquad (2.1)$$

where electrons with mass m and charge e are denoted by lower case subscripts and nuclei with mass M_I and charge Z_I are denoted by upper case subscripts; in this expression, each term represents: the electronic kinetic energy, the electron-electron Coulomb interactions, the electron-nuclei Coulomb interactions, the nuclear kinetic energy, and the nucleus-nucleus Coulomb interactions, respectively. In this case, Ψ is the many-body electronic wave function which depends on each of the spatial electronic coordinates of each N electrons as well as on the spatial coordinates of each M nuclei, *i.e.*, $\Psi = \Psi(\mathbf{r}_1, \ldots, \mathbf{r}_N; \mathbf{R}_1, \ldots, \mathbf{R}_N)$. Finally, E represents the ground state energy of the many body system.

The Born-Oppenheimer approach postulates that the movement of the nucleus and electrons can be separated because the electron mass is much smaller than the mass of the nucleus. The electrons respond instantaneously to the change of position of the nucleus. For this reason the position of the nucleus is a parameter that is reflected in the potential of the equation of Schrödinger delimiting the wave function of

the electrons.[50] The equation can be rewritten as follows

$$\left[-\sum_i \frac{\nabla_i^2}{2} + \sum_i V_n(\mathbf{r}_i) + \frac{1}{2} \sum_{i \neq j} \frac{1}{|\mathbf{r}_i - \mathbf{r}_j|} \right] \Psi = E\Psi, \tag{2.2}$$

where $V_n(\mathbf{r})$ is the Coulomb potential of the nuclei experienced by the electrons (*cf*. Eq. 2.1). Considering the Born-Oppenheimer approximation, the independent electron approximation and the Pauli's exclution principle, the wavefunction Ψ can be approximated as an Slater determinant:

$$\Psi(r_1, ..., r_N) = \frac{1}{\sqrt{N!}} \begin{vmatrix} \phi_1(\mathbf{r}_1) & \cdots & \phi_1(\mathbf{r}_N) \\ \vdots & \ddots & \vdots \\ \phi_N(\mathbf{r}_1) & \cdots & \phi_N(\mathbf{r}_N) \end{vmatrix}. \tag{2.3}$$

Within this approximation, the electron charge density can be expressed as the sum of individual probabilities of finding electrons in an occupied state i:

$$n(r) = \sum_i |\phi_i(r)|^2. \tag{2.4}$$

DFT is based on two important theorems proposed by Hohenberg and Kohn[51] and the set of equations by Kohn-Sham (KS)[52]. The first theorem states that the energy of the ground state of the Schrödinger equation is a unique functional of the electron density, where a one-to-one mapping is proposed between the fundamental state wavefunction and the electronic density of the ground state. Therefore the energy E in the ground state can be expressed as $E[n(\mathbf{r})]$ where $n(\mathbf{r})$ is the electronic density.[12] The second theorem states that the electron density that minimizes the energy of the original functional is the true electronic density corresponding to the full solution of the Schrödinger equation.[53]

These theorems reveal that in the ground state the total energy is determined by the electronic density, that is, the total energy is a functional of the electronic density. The energy can be expressed based on electronic density, kinetic energy and Coulomb energy as

$$E = \int n(\mathbf{r}) V_n(\mathbf{r}) d\mathbf{r} + <\Psi|\widehat{T} + \widehat{W}|\Psi>, \tag{2.5}$$

where $\widehat{T}$ and $\widehat{W}$ represent the operators of the kinetic and Coulomb energy, respectively. The functional

associated with the energy is expressed as

$$E\left[n\right] = \int n\left(\mathbf{r}\right) V_n\left(\mathbf{r}\right) d\mathbf{r} + <\Psi\left[n\right]|\widehat{T} + \widehat{W}|\Psi\left[n\right]>, \tag{2.6}$$

the first term in the functional depends explicitly on the electronic density. However, the two additional terms the dependence on electronic density is implicit. In this case, the functional can be expressed in terms of the electron density n that can be obtained from the single electron wavefunctions as

$$E\left[n\right] = E_{known}\left[n\right] + E_{XC}\left[n\right]. \tag{2.7}$$

This equation is a didactic way to separate analytically the known terms E_{known} and the rest in E_{XC}. The following contributions formed the term E_{known}

$$E_{known}\left[n\right] = -\frac{\hbar^2}{2m}\sum_i\int\psi_i^*\nabla_i^2\psi_i d^3r + \int V\left(\mathbf{r}\right)n\left(\mathbf{r}\right)d^3r + \frac{e^2}{2}\int\int\frac{n\left(r\right)n\left(\mathbf{r}'\right)}{\left|\mathbf{r}-\mathbf{r}'\right|}d^3rd^3r' + E_{ion}, \tag{2.8}$$

where electron kinetic energies, the Coulomb interactions between the electrons and the nuclei, the Coulomb interactions between pairs of electrons, and the Coulomb interactions between pairs of nuclei are represented in order in the equation. Finally, the term not previously defined (E_{XC}) is termed as the exchange and correlation (XC) energy. This term includes all the quantum mechanical effects not considered in the other terms (E_{known}).[12]

The electronic density of the ground state minimizes the total energy $E[n]$ of the system, this is known as Hohenberg-Kohn variational principle that leads to a set of equations for non-interacting electrons also known as the Kohn-Sham (KS) equations .[53]

$$\left[-\frac{\hbar^2}{2m}\nabla^2 + V\left(\mathbf{r}\right) + V_H\left(\mathbf{r}\right) + V_{XC}\left(\mathbf{r}\right)\right]\psi_i\left(\mathbf{r}\right) = \varepsilon_i\psi_i\left(\mathbf{r}\right), \tag{2.9}$$

where the second term within the brackets refers to the potential of the interaction between an electron and the set of atomic nuclei.[12] The third term is called the Hartree potential and is expressed as

$$V_H\left(\mathbf{r}\right) = e^2\int\frac{n\left(\mathbf{r}'\right)}{\left|\mathbf{r}-\mathbf{r}'\right|}d^3r', \tag{2.10}$$

this potential refers to the Coulomb repulsion between the electron of interest and the total electron density of all the electrons in the many-body systems. V_H includes a self-interaction because the electron of interest

is also part of the total density, and this means the potential contains an unphysical interaction between the electron and itself.[54] The correction of this artifact together with the missing many body effects are added in the final potential of the KS equation, V_{XC}. This term is defined mathematically as a functional derivative of the XC energy[53]

$$V_{XC}(\mathbf{r}) = \frac{\delta E_{XC}(\mathbf{r})}{\delta n(\mathbf{r})}. \tag{2.11}$$

Hartree's potential is needed to solve the KS equations; however, finding the potential would involve solving the electron density but this implies to know the single-electron wavefunctions and for this we need to solve the KS equations thus returning an endless cycle. The following self-consistent KS algorithm solves this problem:

1. Propose an initial electronic density; in other words, a trial density $n(\mathbf{r})$.

2. Solve the KS equations using the trial electron density, thus obtaining single particle wave functions $\Psi_i(\mathbf{r})$.

3. Calculate the electron density associated with the wave functions of a single particle in step 2, $n_{KS}(\mathbf{r}) = \sum_i \psi_i^*(\mathbf{r})\psi_i(\mathbf{r})$, where N is the number of electrons.

4. Compare both electronic densities. In the case that they are equal, this density can be used to calculate the total energy. In the case that they are different, the electron density is input to step 2 and start the cycle over again.

However; there is a term that continues to cause problems, and this is the XC functional. Considering, the uniform electron gas, it is possible to derive an approximate XC functional where the electron density is constant at all points in space. Despite the simplicity of this approximation, the advantages it provides are important. Specifically, by assuming the known XC functional of the uniform electron gas is also the XC functional of an inhomogeneous system

$$V_{XC}(\mathbf{r}) = V_{\text{electron gas}}^{XC}[n(\mathbf{r})]. \tag{2.12}$$

For this reason, it is called the local density approximation (LDA) since it only uses the local density to define the approximate XC functional. The next level of approximation uses information about the

local electronic density and the local gradient in the electronic density, so it is called the generalized gradient approximation (GGA). Finally, hierarchies of functional can be developed to include more and more detailed physical information.[12]

2.3.1 Functionals

The LDA was the first successful approximation for the XC functional energy. In this type of approximation, the homogeneous electron gas gives the XC potential at each point in space.[55] The advantages of this approach are its unique value thanks to the theory of uniform spin densities, and higher precision due to the use of methods for unpolarized and fully polarized electron gases.[56] The fact that the density is not uniform is the main drawback with the use of LDA. After all, this approach has provided results that are in good agreement with the experimental results in many materials.[55] However, the LDA presents certain quantitative failures that have been corrected with other types of approximations such as the generalized gradient approximation (GGA).[57]

The GGA take into account gradients of charge densities.[55] Some advantages of the GGA approach are improvements in total energies, atomization energies, energy barriers, and structural energy differences.[58] The combination of both correlations provides a better description of certain properties such as magnetic states.[59] The differences between these two approximations are

$$E_{XC}^{LSDA}\left[n_\uparrow, n_\downarrow\right] = \int n E_{XC}^{inf}\left(n_\uparrow, n_\downarrow\right) d^3\mathbf{r}, \tag{2.13}$$

$$E_{XC}^{GGA}\left[n_\uparrow, n_\downarrow\right] = \int f\left(n_\uparrow, n_\downarrow, \nabla n_\uparrow, \nabla n_\downarrow\right) d^3\mathbf{r}, \tag{2.14}$$

where $E_{XC} = E_x + E_C$ is a functional for the electron spin density up $n_\uparrow(\mathbf{r})$ and down $n_\downarrow(\mathbf{r})$ which must be approximated; E_{XC}^{inf} and f are parametrizable analytical functions.[58]

Standard DFT uses LSDA or spin-polarized (SP)GGA that provides reliable description of many materials but it falls in describing systems where electrons tend to localize with strong interactions, this is the case of transitions metal oxides (TMO). It has been reported that DFT studies on TMO predicts wrongly a metallic ground states instead of the observed insulating state. In the case of Fe_3O_4, DFT predict a semi-metallic state for the low symmetry phase in contrast to the insulating state observed experimentally. Considering the strong correlation problem, DFT can be improved by adapting a Hubbard-U model that

introduces on-site Coulomb interactions for the strongly correlated electrons with angular momentum l. Considering the GGA framework the so-called GGA-U method according to Dudarew, the total energy can be expressed like

$$E^{GGA+U} = E^{GGA} + \frac{\overline{U} - \overline{J}}{2} \sum_{\sigma} \left[\left(\sum_{m} n^{\sigma}_{m,m} \right) - \left(\sum_{m,m'} n^{\sigma}_{m,m'} n^{\sigma}_{m',m} \right) \right], \tag{2.15}$$

where $\overline{U}$ and $\overline{J}$ are the effective on-site Coulomb and exchange parameters, $n^{\sigma}_{m,m'}$ that fell the Hubbard-U interaction and $m = l, -l + 1, ..., l - 1, l$. Finally, the effective interaction parameter is deduced as $U_{eff} = \overline{U} - \overline{J}$, named from now on in this text simply U.[60] This parameter U can be obtained by first-principles calculations or by fitting to some known experimental property (*e.g.* the band gap) or higher level computational result.

2.3.2 Pseudopotentials

Electrons near the nucleus (core electrons) are practically inert in the sense that they do not interact in chemical bonding. Therefore, the core electrons and the nucleus are replaced by pseudopotentials that emulate the actual potential, above certain radius, that binds the valence electrons.[61] The concept of pseudopotentials is approached from a linear combination between a smooth wave-function $|\phi_v\rangle$ and core electron orbitals $|\psi_c\rangle$ that represent the all-electron valence orbital $|\psi_v\rangle$ as $|\psi_v\rangle = |\phi_v\rangle + \sum_c \alpha_{cv} |\psi_c\rangle$. The last expression can be rewritten taking into account that $|\psi_v\rangle$ and $|\psi_c\rangle$ are solutions of the Schrödinger equation with eigenvalues ε_v and ε_c, respectively. The next equation

$$\left[\widehat{H} + \sum_c (\epsilon_v - \epsilon_c) |\psi_c\rangle \langle \psi_c| \right] |\phi_v\rangle = \epsilon_v |\phi_v\rangle, \tag{2.16}$$

shows that ϕ_c the lowest-energy solution of a new Hamiltonian keeping the same eigenvalue that ψ_v. The advantage of replacing the problem of all the electrons using an effective $\widehat{H}$ allows to reduce the computational load thanks to the decrease of the orbitals determined by the equations of KS and avoid the oscillations caused by the orbitals near the nucleus.[62]

The projector-augmented wave (PAW) method explain that the full valence electron function Ψ is split into three parts, so the total electronic energy of the system can also be partitioned appropriately. This method has two important advantages. The first is the calculation of all the electrons from the beginning in

which the full-wave function is calculated for each electron and the second is that it requires a very small number of plane waves to expand the smooth part of the full-wave function of each valence electron.[63]

2.4   Lattice Periodicity and Plane Waves

Perfect crystals are arrange of atoms organized in a definite pattern defined by a tree dimensional lattice. Considering the translational symmetry, the knowledge of atomic structure within the unit cell allows to determine the structure of the whole crystal. Part of the important concepts in crystalline structures is lattice parameters, periodicity, and supercells. These concepts are essentials in the DFT calculations for many-body systems. A crystal structure can be defined by vectors a_1, a_2, and a_3. The concept of primitive cell arises from the need for a cell that contains the minimum amount of atoms needed to define any system.[12]

Bloch's theorem states that solutions to the Schrödinger equation for a periodic system must satisfy the following property

$$\phi_{\mathbf{k}}(\mathbf{r}) = exp\,(i\boldsymbol{k}\cdot\boldsymbol{r})\,u_{\mathbf{k}}\,(\mathbf{r})\,, \qquad (2.17)$$

where $u_{\mathbf{k}}\,(\mathbf{r})$ is periodic, then $u_k\,(\mathbf{r}) = u_{\mathbf{k}}\,(\mathbf{r} + n_1\mathbf{a_1} + n_2\mathbf{a_2} + n_3\mathbf{a_3})$ for integers n_1, n_2 and n_3. Therefore it is possible to solve the Schrödinger equations for different $\mathbf{k}$ in reciprocal space, and then sum over k-points to obtain the electron density.

Reciprocal lattice vectors are vectors that define the reciprocal space and are shown below.

$$\mathbf{b}_1 = 2\pi\frac{\mathbf{a}_2\times\mathbf{a}_3}{\mathbf{a}_1\cdot(\mathbf{a}_2\times\mathbf{a}_3)}, \qquad (2.18)$$

$$\mathbf{b}_2 = 2\pi\frac{\mathbf{a}_3\times\mathbf{a}_1}{\mathbf{a}_2\cdot(\mathbf{a}_3\times\mathbf{a}_1)}, \qquad (2.19)$$

$$\mathbf{b}_3 = 2\pi\frac{\mathbf{a}_1\times\mathbf{a}_2}{\mathbf{a}_3\cdot(\mathbf{a}_1\times\mathbf{a}_2)}. \qquad (2.20)$$

Notice that long vectors in the real space correspond to short vectors in the reciprocal space and vice versa.[64] It is possible to define a Wigner-Seitz cell in the reciprocal lattice, since this cell has many special properties, it is given a name: the Brillouin zone (BZ). The most important point within the BZ is the Γ point which is at $\mathbf{k} = 0$.

For a periodic system, $V(\mathbf{r})$, $V_H(\mathbf{r})$, $V_{XC}(\mathbf{r})$ and $\phi_k(\mathbf{r})$ can be written as a linear combination of plane waves. In the case of $\phi_{\mathbf{k}}(\mathbf{r})$, $u_{\mathbf{k}}(\mathbf{r})$ can be expanded with a special set of plane waves:

$$u_{\mathbf{k}}(\mathbf{r}) = \sum_{\mathbf{G}} C_{\mathbf{G}} exp\left[i\mathbf{G} \cdot \mathbf{r}\right], \tag{2.21}$$

where the summation is over all vector represented by $\mathbf{G} = m_1\mathbf{b}_1 + m_2\mathbf{b}_2 + m_3\mathbf{b}_3$ with integer values for m_i. The set of vectors G is defined as $\mathbf{G} \cdot \mathbf{a}_i = 2\pi m_i$ for any lattice vector $\mathbf{a}_i$. Combining the above equation with the equation (2.17) obtain

$$\phi_{\mathbf{k}}(\mathbf{r}) = \sum_{\mathbf{G}} c_{\mathbf{k}+\mathbf{G}} exp\left[i\left(\mathbf{k} + \mathbf{G}\right)\mathbf{r}\right], \tag{2.22}$$

these functions are solution of the Schrodinger equation with kinetic energy $E = \frac{\hbar^2}{2m}|\mathbf{k} + \mathbf{G}|^2$. This motivates a cutoff energy for the basis

$$E_{cut} = \frac{\hbar^2}{2m}G_{cut}^2. \tag{2.23}$$

It is important to keep in mind that the energy cutoff should be properly selected and keep the same in order to compare different calculations in a given system.[12] Equation (2.21) is rewritten as

$$\phi_{\mathbf{k}}(\mathbf{r}) = \sum_{|\mathbf{G}+\mathbf{k}|<G_{cut}} c_{\mathbf{k}+\mathbf{G}} exp\left[i\left(\mathbf{k} + \mathbf{G}\right)\mathbf{r}\right], \tag{2.24}$$

The vast majority of crystal calculations involve the integration of periodic functions of a wave vector in the entire BZ or in specific portions. The Monkhorst and Pack scheme is based on the fact that the k-points are distributed homogeneously in the BZ, with rows or columns of k-points that go parallel to the reciprocal network vectors that cover the BZ.[65]

2.5 Introduction to VASP

The Vienna *Ab initio* Simulation Package (VASP) is a computer program used for calculation of electronic structures, molecular dynamics materials at the atomic scale, structural relaxation, linear response to electric fields, optical properties, and others.[66–68] VASP implements DFT to model a many body systems by solving the KS equations self-consistently.

The quantity E_{XC} is improved by a semilocal approach by means of the GGA. In equation

$$E_{XC}^{GGA}[n_\uparrow, n_\downarrow] = \int f(n_\uparrow, n_\downarrow, \nabla n_\uparrow, \nabla n_\downarrow) d^3\mathbf{r}, \tag{2.25}$$

f represents a density gradient expansion for hole XC present around each electron, that is, a deviation from the probability of finding other electrons in the neighborhood. Now, the V_{KS} described in the equation (6) will also be a continuous function of ∇n. The exact potentials are replaced by PAW pseudopotentials. The PAW method is one of the best for dealing with large systems due to its accuracy, computational cost and simple theoretical background.

The Kohn-Sham method starts rewriting the Schródinger equation by $\widehat{\mathbf{H}}_{KS}\psi_i(\mathbf{r}) = \varepsilon_i\psi_i(\mathbf{r})$, where $\psi_i(\mathbf{r})$ and $\widehat{\mathbf{H}}_{KS}$ represents the KS orbitals and the effective KS hamiltonian with a eigenvalues of ε_i. In section 2 found the equation (2.3) for the initial electron density in order to start the calculation of the KS potential in equation (2.6). By solving the Schrödinger equation, and using the results in the equation, it is possible to find a new electron density. In the case of the initial and final density are equal, then the ground state density has been found. Otherwise, a new density must be calculated by minimizing the total energy. The process must be carried out to achieve a consistent density.

In Section 2.4, an expression for $\psi_i(\mathbf{r})$ is presented as a sum of plane waves. In order to speed-up the calculation proposed by KS, the *k*-points are selected using the Monkhorst-Pack scheme within the BZ.

Once the KS equations have been solved, the cartesian atomic coordinates are fixed at the same time that the electronic ground state is calculated. This process results in the optimization of atomic orbitals and electronic density. In this way, the new output density is forwarded for the next iterations of the process (Pulay mixed). To optimize the atomic structure, is applied a damped second-order equation-of-motion for the ions employing the forces of Hellmann-Feynman on atoms and stresses on the unit cell.[69] The Hellmann-Feynman theorem infer an expression for the ionic forces and stress tensor of the electronic fundamental state. The steepest descent mode relaxes the atomic structure while VASP calculate the electronic ground state. Figure 2.4 shows the protocol that VASP follows for solve the KS equations until the total energy and the ionic forces converge around a fixed error.

VASP provides the group of magnetic symmetry according to the initial magnetic moments for spin polarized calculations. This information influences the construction of the reciprocal space necessary for the integration of the BZ. The total charge and spin densities, forces and tensors of each iteration use the same information of the initial magnetic moments. Likewise, periodic structures are routinely optimized
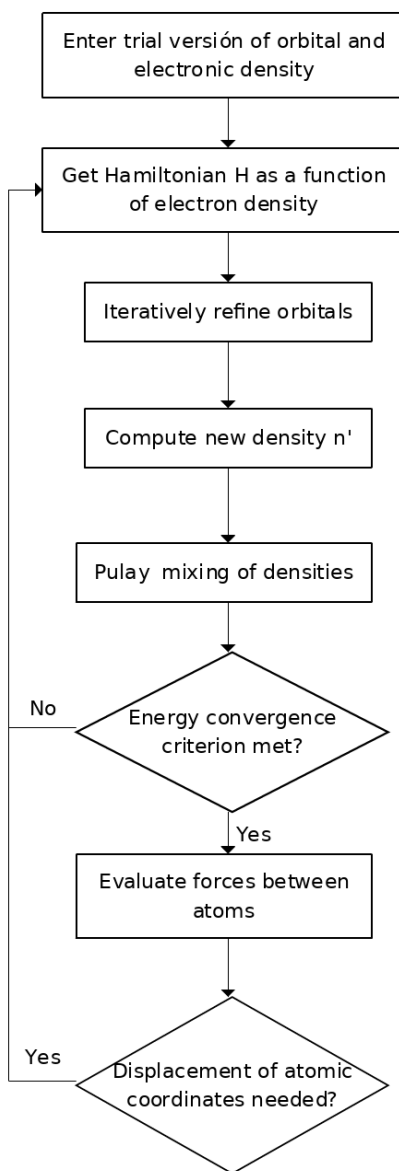
Figure 2.4: Summary of the algorithm used in VASP in order to solve the KS equation.

in VASP using quasi-Newton conjugate gradient schemes.[70] It is important to mention the initial files that are needed to perform the corresponding calculations in VASP.

- The INCAR file with the simulation parameters *e. g.* cutoff energy, functional, initial magnetic moments, and others.

- The POSCAR file that contain the atomic positions and lattice parameters of the atomic structures to be modeled.

- The POTCAR file contains the potentials associated with each type of atom in the system.

- The KPOINTS file that contains the information regarding for k-points in the BZ.

2.6   Characterization Techniques

Characterization techniques are tools that facilitate the study of different types of materials (*e. g.* oxides, carbon-based materials, ceramics, and others), surfaces and nanoparticles.[71–73] In this section, we present three characterization techniques based on irradiating energy on the surface of a sample, electron tunneling, and microscopy.

2.6.1   Ultraviolet Photoelectron Spectroscopy

Ultraviolet photoelectron spectroscopy (UPS) is a type of photoemission spectroscopy (PES). These types of techniques describe important information about the ionization energies of atoms and molecules.[74] The ionization energy is

$$E_I = h\nu - KE - \Phi, \tag{2.26}$$

where $h\nu$ is the photon energy and EK is the kinetic energy of the electron. In the UPS, a monochrome ultraviolet light beam ionizes the molecules or atoms. In general, the range of light used is 58.4 nm equivalent to 21.22 eV. The photons that collide on the surface of the sample create a photoelectric effect thus releasing electrons to the vacuum.[75]

The photoemission process is based on the model of the three steps. In the first process, photoionization was carried out *i.e.* the photon is absorbed and the electron is excited. The next process is the diffusion of the electron through the sample and the probability to reach the surface is related to the inelastic mean free path. Finally; in the third process, the electron escapes from the surface into the vacuum.[76] Another important factor is the cross-section, which refers to the probability of the photon interacting with an

electron in an atom of the material studied.[77] Equation (2.26) represents the energy necessary to release the electron by the energy of the photon.

Finally, photoelectron spectroscopies are classified according to their kinetic energy by means of an energy analyzer, detector, and recorder. The signal obtained is the number of electrons detected at a given kinetic energy.[78] Within this type of characterization technique, there is an important concept called the inelastic mean free path (IMFP). The simplest and most precise definition of this concept is the average distance for an electron to travel within a solid before an inelastic collision occurs. This process involves a loss in energy important for this characterization technique. The IMFP allows one to obtain the emergent intensity of the electron after the interaction within the solid through the following equation

$$I = I_o exp\left(\frac{-z}{\lambda cos\theta}\right), \tag{2.27}$$

where I_o is the incident radiation intensity and $z/cos\theta$ is the length of the path of an electron with a transposition angle θ and a depth of z.[79] Finally, some investigations and simulations have been carried out in order to predict the IMFP of different types of materials.[80–82]

2.6.2   Scanning Tunneling Microscopy

The principle in scanning tunneling microscopy (STM) is the scanning of the surface of interest by a metal tip. This metal tip is fixed to a piezoelectric device which is free to move in all three dimensions. This piezoelectric device undergoes variations of voltages producing the scanning of the studied surface based on the displacement of the metal tip.[83]

The difference in voltage between the tip and the sample influences the tunnel current flowing between the tip and the sample. The Fermi level of the sample rises above the tip by applying a negative voltage $(-V)$ with respect to the tip. In the case of a positive voltage $(+V)$ the Fermi level of the tip rises above the Fermi level of the sample. Due to this potential difference, the electrons migrate to the empty states of the tip or sample depending on the voltage applied.[84]

The elastic tunneling current from the sample to the tip for states with energy ε with respect to E_F is

$$I_{sample \to tip} = -2e \cdot \frac{2\pi}{\hbar} |M|^2 \left(\rho_s\left(\varepsilon\right) \cdot f\left(\varepsilon\right)\right) \left(\rho_t\left(\varepsilon + eV\right) \cdot \left[1 - f\left(\varepsilon + eV\right)\right]\right), \tag{2.28}$$

where the factor 2 is associated with the spin, $-e$ is the electronic charge, $|M|^2$ is the tunneling matrix,
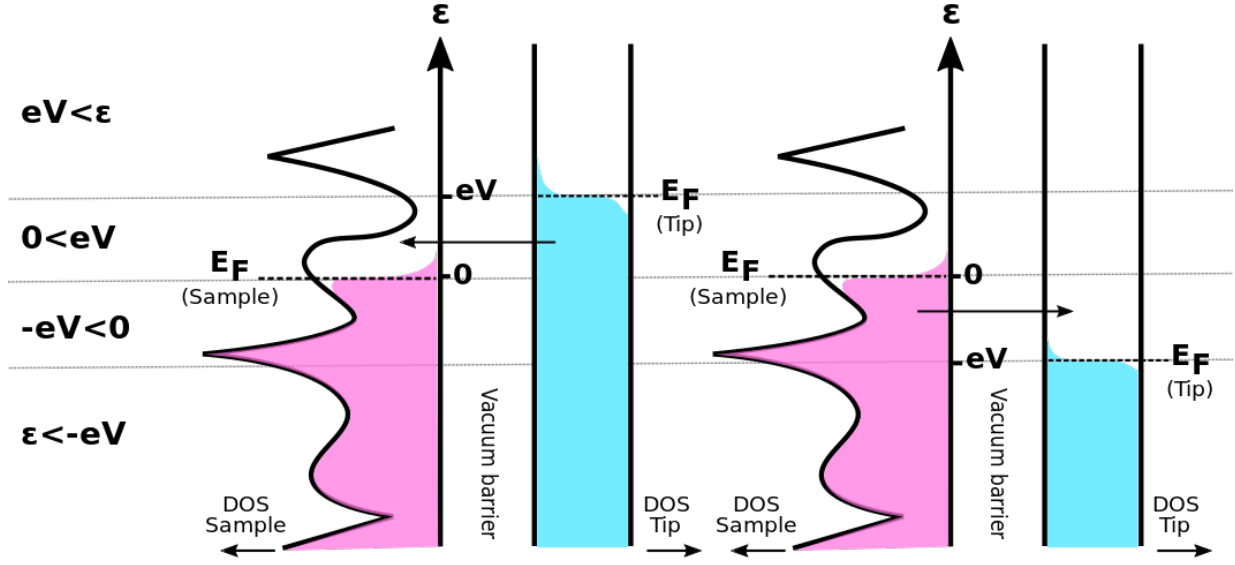
Figure 2.5: Schematic of tip-sample tunneling. The energy is shown along the vertical axis while the density of states (DOS) of the sample and the tip is shown on the horizontal axes. The states occupied in the sample and the tip are represented in violet and light blue, respectively. The positive voltage decreases the Fermi level of the sample with respect to the Fermi level of the tip. The electrons in the occupied states of the tip are able to tunnel towards the tip producing a measurable current.

$f(\varepsilon)$ is the Fermi distribution, $(\rho_s(\varepsilon) \cdot f(\varepsilon))$ represents the filled states of the sample for tunneling from and $(\rho_t(\varepsilon + eV) \cdot [1 - f(\varepsilon + eV)])$ represents the empty states of the tip for tunneling to. This current is not the only one that is generated at the time of scanning, but there is a smaller current generated from tip to sample.[85] Therefore, the above equation can be written as

$$I = -\frac{4\pi e}{\hbar} \int_{-\varepsilon_F}^{\infty} |M|^2 \rho_s(\varepsilon) \rho_t(\varepsilon + eV) \{f(\varepsilon)[1 - f(\varepsilon + eV)] - [1 - f(\varepsilon)]f(\varepsilon + eV)\} d\varepsilon. \qquad (2.29)$$

However, this equation can be approximated by taking into consideration the temperature of measurement, the voltage applied and tip material. In the case of measurements at low temperatures, the Fermi function is cut off abruptly, which allows the integral to be divided according to the energy ranges shown in Figure 2.5. For the case of the voltage applied, the ranges of interest of ε that solve the integral are $-eV < \varepsilon < 0$ for $-V$ and $0 < \varepsilon < eV$ for $+V$. The material of the tip can be considered as a material with a flat density of states in such a way that this can be considered as a constant outside the integral. The equation of the

tunneling current can be expressed as

$$I \approx -\frac{4\pi e}{\hbar} |M|^2 \rho_t(0) \int_0^{eV} \rho_s(\varepsilon) d\varepsilon. \tag{2.30}$$

The probability of creating a tunnel through a barrier of potential is $|M|^2 = e^{-\frac{2s}{\hbar}\sqrt{2m\varphi}}$ where m is the mass of the electron, s is the separation between the tip and the sample, and φ is a mixture of the work functions of the tip and the sample. The higher φ produces a greater tunneling current for a given change in s which leads to a better resolution. Finally, the tunneling current is

$$I \approx \frac{4\pi e}{\hbar} e^{-s\sqrt{\frac{8m\varphi}{\hbar^2}}} \rho_t(0) \int_0^{eV} \rho_s(\varepsilon) d\varepsilon. \tag{2.31}$$

2.6.3 Transmission Electron Microscopy

In the transmission electron microscopy (TEM), an electron beam of uniform density irradiates the samples. The electrons are emitted inside the electron gun by thermionic emission or field emission. The main objectives of the condenser-lens are the variation of the illumination aperture, the area of illumination in the sample and the distribution of the electron intensity after the sample.[86]

The electrons interact strongly with the atoms of the sample by means of elastic and inelastic dispersion. Inelastic scattering has a loss of energy, thus providing information about composition, morphology and crystal structure through the diffraction pattern of the same. In general, samples should have a thickness of 5 nm to 0.5 μm in order to ensure good dispersion and atomic interaction.[87]

Figure 2.6 shows the operation scheme of a TEM. The first primordial structure of a TEM is a source of emission or cathode. The lenses are specialized devices to redirect the transmitted electrons. These lenses operate electrostatically or magnetically. The apertures are metal plates that filter the desired electrons according to the type of focus or technique. Finally, a fluorescent screen is responsible for the visualization and focus of the image.[89]

One advantage of TEM is the elastic diffraction patterns that can be obtained from the crystals or materials of interest. A diffraction pattern (DP) is an image formed by the scattered electrons of the
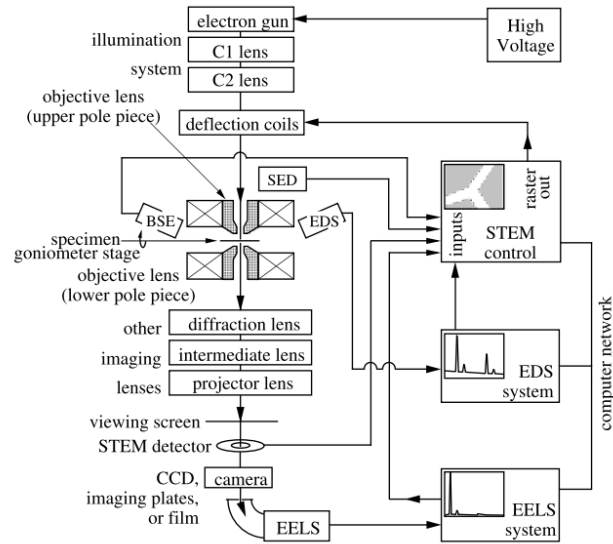
Figure 2.6: Diagram of the functioning and instruments present in TEM together with certain characteristics for STEM. Important instruments are electron gun, lens and detectors Adapted from Ref. 88.

sample. This image provides a lot of important crystallographic information. DPs are of many types and depend to a large extent on the type of equipment, the angle of incidence and other factors. The intensity of scattered electrons decreases with increasing the angle of incidence of the beam. Finally, the intensity of scattering depends to a large extent on the type of material under observation.[77]

Chapter 3

Methodology

The first step towards calculation on the Magnetite system using The Vienna *Ab initio* Simulation Package (VASP) is the determination of both the energy cutoff and k-points mesh. The generalized gradient approximation (GGA) by Perdew-Burke-Ernzerhof revised for solids (PBEsol) was used for the exchange and correlation (XC)-functional [82]. Spin-polarized (SP)DFT with an energy cutoff of 650 eV and k-point separation of 0.035 Å^{-1} (corresponding to a mesh of $(6 \times 6 \times 6)$ of primitive Magnetite (Fe$_3$O$_4$) with symmetry $Fd\bar{3}m$) converge the total energy to < 1 meV/atom. The nucleus and core electrons were described by PAW potentials with valence configuration 3p^6 3d^6 4s^2 for Fe and 2s^2 2p^4 for O. Moreover, the atoms of the system are fully relaxed until all the forces are < 0.02 eV/Å. In the case of surfaces, a vacuum of 15 Å was used to separate the slabs along the z-direction.

Table 3.1: Numerical VASP parameters used for cubic Fe$_3$O$_4$.

Parameter	Initial Value
Energy cutoff value (plane wave basis set)	650 eV
k-points (reciprocal space)	$(6 \times 6 \times 6)$
k-points distance (reciprocal space)	0.035 Å^{-1}
Magnetic moments	5 or -5 μ_B for Fe and 0 μ_B for O

3.1   Calculations in VASP

In this work, we used a energy cutoff of 650 eV and k-point mesh of $(6 \times 6 \times 6)$ to converge the total energy to < 1 meV/fu. (fu. $=$ Fe$_3$O$_4$). Before beginning to study Fe$_3$O$_4$ bulk and the (100) surfaces, the calculations made in VASP require the determination of both the energy cutoff and k-point mesh as convergence parameters for the primitive cell with symmetry $Fd\bar{3}m$. Figure 3.1 shows the processes carried out to find the ground state energy and the optimum volume of the primitive cell of Fe$_3$O$_4$. Table 3.1 presents the converge numerical parameters in VASP used in this initial process.
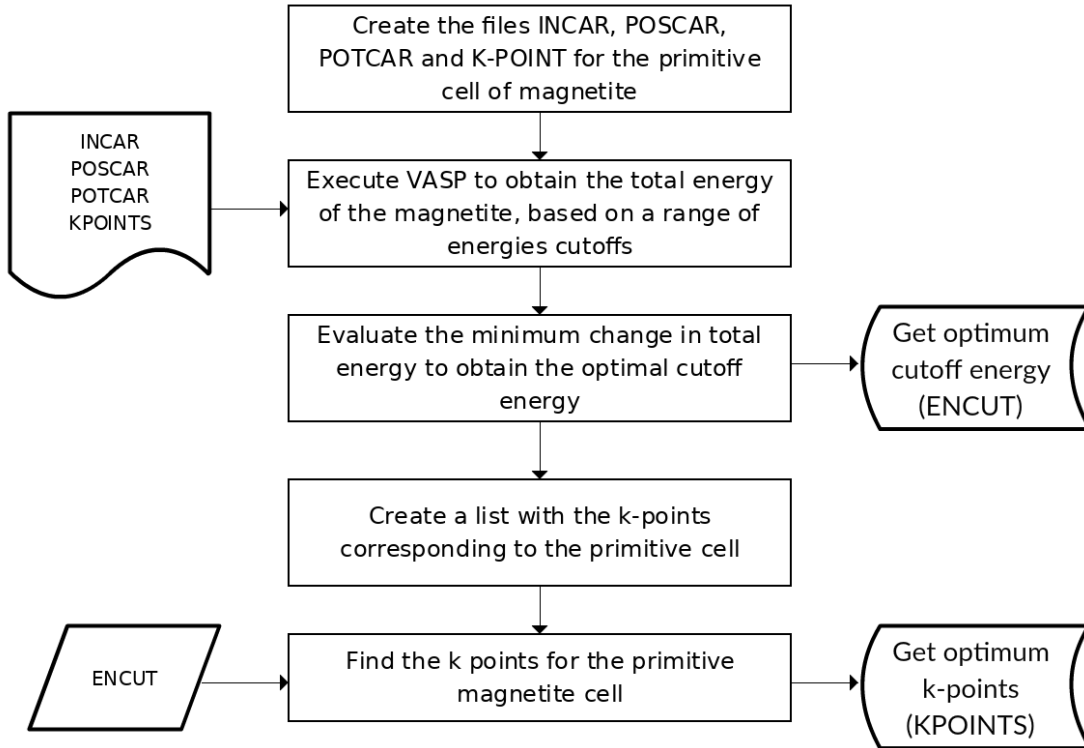

Figure 3.1: Optimization of parameters for calculations in VASP, case of Fe$_3$O$_4$ ferrimagnetic (FiM)-227.

Once we have the data for the primitive cell with symmetry $Fd\bar{3}m$, future calculations are divided into two cases: Fe$_3$O$_4$ symmetry *Pmca* and Fe$_3$O$_4$(100) surfaces . For the symmetry *Pmca*, the process presented in the last image are used for each U correction. For KPOINTS file, the new values of the k-points are $(5 \times 5 \times 2)$ with a separation of 0.032 Å^{-1}. Files POSCAR and POTCAR are changed to
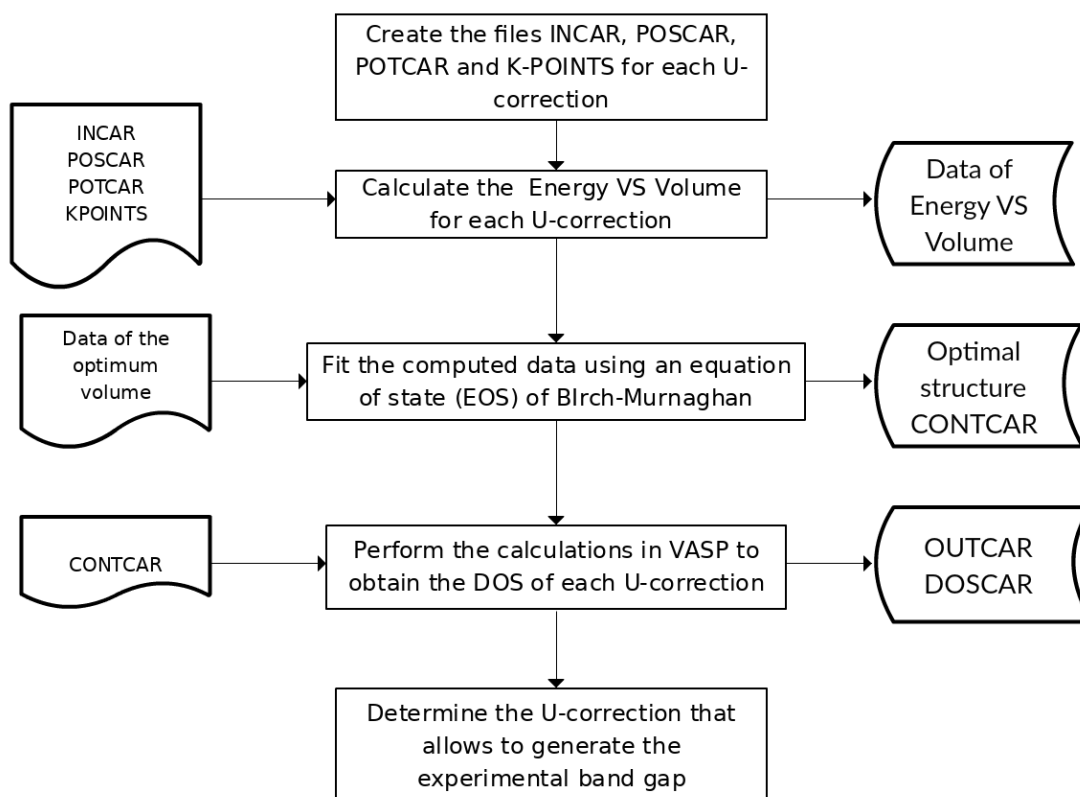
describe properly the new symmetry.

Figure 3.2: Optimization process of Fe$_3$O$_4$ with symmetry *Pmca*.

The next process is summarized in Figure 3.2 where *PBEsol* + *U* is applied only for Fe-3d electrons with *U* = 1, 2, 3, 3.5, 4, 4.5 and 5 V. These corrections are specified in each INCAR file for each *U* value. The calculated results allow determining the equation of state (EOS) for each *U*-correction. With the optimal volumes found it is possible to determine the density of states (DOS) and the band gap (E_g) for each *U*-correction and compared with the experimental value of 0.14 eV to find the *U* correction that best fits the experiment.[8]

Figure 3.3 summarizes the processes carried out to find the DOS for the system with symmetry $F d\overline{3}m$ and *Pmca*. Additionally, the EOS of each system is compared among them to determine the most stable system.

Next is the study of Fe$_3$O$_4$(100) surfaces. Figure 3.4 shows a scheme of the process carried out for
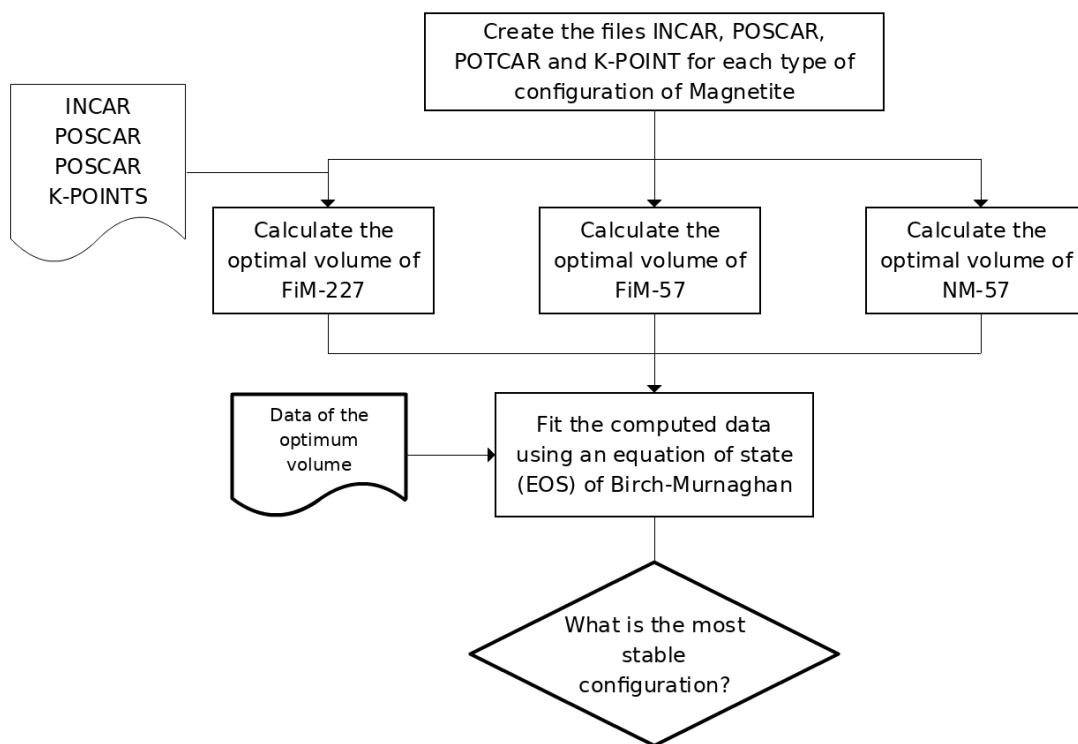
Figure 3.3: Optimization process of bulk Fe_3O_4 with symmetry 227 and 57.

this part of the work. First, it is necessary to adapt the initial VASP files. It is important to mention that the study of surfaces requires dipole corrections along the *z* direction (See Anexo INCAR). The surfaces studied are divided into two types according to the topmost layer of the system. The Section 4.1.3 specifies the type of surface and its structural differences. Figure 3.2 is again useful for calculating the optimal structure and DOS for each surface. However, it is necessary to introduce the determination of the partial density of states (partial density of states (PDOS)). The PDOS shows the electronic contributions of each type of atom of the system. Likewise, the PDOS calculated for a certain number of layers is useful to determine the band gap of the surface.

Surface energy was calculated by an approach presented by Reuter *et al.*[90] where values are easy to obtain by means of density-functional theory (DFT) calculations. In general terms, this energy relates the total energy of the slab, which depends on its volume, the energy of the bulk, the area of slab, the chemical potential of O and finally of the amount of Fe and O atoms. With this equation, you can make a graph
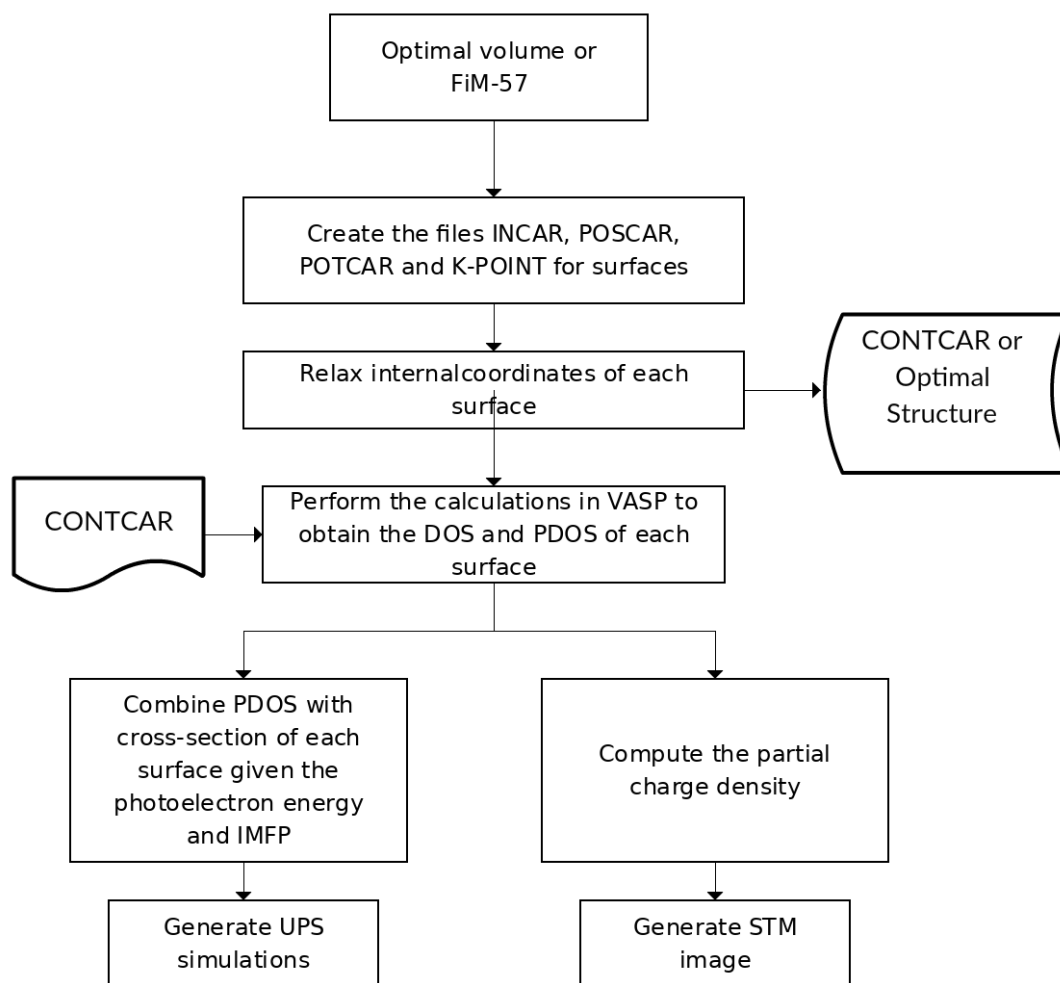
Figure 3.4: Optimization process of $Fe_3O_4(100)$ surfaces study.

based on the potential of O that shows the surfaces most likely to obtain a certain O potential or O_2 gas pressure.

The next part of the work is ultraviolet photoelectron spectroscopy (UPS) simulations. For UPS simulations it is necessary to calculate the inelastic mean free path (IMFP) and photoemission cross-section associated with $Fe_3O_4(100)$ surfaces . The IMFP is obtained following the model proposed by Tanuma.[82] The variables used for these calculations are the number of electrons per formula unit, band gap of the system (data provided by the calculations in VASP), type of atoms and stecheometric coefficient as

well as their density. Once the predictions have been calculated, it is necessary to extrapolate to determine the value of the IMFP. The next step is to take from the database the cross-section value for each orbital of the Fe$_3$O$_4$ atoms. The values of the IMFP and the cross-section are used for perform the UPS simulation.

Finally, scanning tunneling microscopy (STM) simulation was carried out by computing the local density of states (LDOS) from E_F to $E_F + V_{\text{BIAS}}$. The values of LDOS at constant height are then compared to the experimental STM.

3.2   Synthesis of Fe$_3$O$_4$ Nanoparticles

Chemical co-precipitation was the technique used for the synthesis of magnetite nanoparticles (MNPs). Even so, the process used is a variation of several methods of synthesis of MNPs.[21,91,92] The reagents used were salts containing Fe cations (ferrous sulfate heptahydrate), mild oxidant (potassium nitrate), and a base (sodium hydroxide). In the following equation describing the general reaction that takes place

$$3FeSO_4 \cdot 7H_2O + 6NaOH + KNO_3 \rightleftharpoons \mathbf{FeO \cdot Fe_2O_3} + KNO_2 + 3NaSO_4 + 24H_2O. \tag{3.1}$$

The formation of the MNPs followed the following steps. First, potassium nitrate oxidized certain Fe^{2+}, this oxidation resulted in Fe^{3+} cations. Secondly, sodium hydroxide caused the formation of iron (II) hydroxide and iron (III) hydroxide. Finally, the processes of hydrolysis and condensation resulted in nanoparticles. The nanoparticles were obtained from two different solutions of sodium hydroxide. The different concentrations of sodium hydroxide were prepared using the amounts described in Table 3.2 in a 250 ml graduated balloon. The concentrations of the solutions had an important influence on the size of the nanoparticles. The ionic excess is calculated through the following equation

$$\left[Fe^{2+}\right]_{EXC} = [FeSO_4] - \frac{[NaOH]}{2}, \tag{3.2}$$

$$[OH^-]_{EXC} = [NaOH] - 2\left[FeSO_4\right], \tag{3.3}$$

so it is possible to determine these excesses for each sample as shown in the Table 3.1.[93]

The sulfate solution was prepared by dissolving 4.1 g of ferrous sulfate in 20 ml of distilled water.

Table 3.2: Notation, concentration, and quantities of reagents used for the synthesis of MNPs.

Label	Concentration (M)	Grams of NaOH (g)	Grams of KNO$_3$ (g)	$\left[Fe^{2+}\right]_{EXC}$	$\left[OH^-\right]_{EXC}$
Fe$_3$O$_4$ − A	0.134	1.4	0.56	0.007	0.02
Fe$_3$O$_4$ − B	0.194	1.9	0.56	-	0.046

The solution of ferrous sulfate and solutions Fe$_3$O$_4$ − A and Fe$_3$O$_4$ − B were mixed and placed in high-frequency sonication for 30 minutes. The pulses were executed for 0.05 s in intervals of 1 s together with a continuous flow of helium. Subsequently, the solution was subjected to a thermal bath at approximately 60 °C for 90 minutes. After 90 minutes, the nanoparticles were cooled to room temperature, see Table 3.3, then washed with distilled water 5 times. Finally, they dried by two different methods: stove at 50 °C or placed in a vacuum desiccator. Figure 3.5 shows the instruments used throughout the synthesis of MNPs.The nanoparticles after sonication were left before the heat treatment at 50 °C as shown in the Table 3.3.

Table 3.3: Rest time after a different process of the synthesis and type of drying.

Label	After sonication	After thermal bath	Drying time	Type of drying
Fe$_3$O$_4$ − A	1 h	24 h	72 h	Stove
Fe$_3$O$_4$ − B	8 h	5 min	7 h	Stove

The samples were characterized using transmission electron microscopy (TEM) and UPS techniques. The preparation of samples for microscopy is based on the dispersion of the MNPs in 99.99% ethanol in an ultrasound bath (BRANSON 1510) for 20 minutes, then 5 μL of each sample was placed in a Grid for Transmission Electron Microscopy (PELCO Grids F / C Cu, 300 MESH). Finally they were introduced in the TEM, FP 5018/11 - Tecnai G2 Spirit Twin and observed at different magnifications. The diffraction pattern of each of sample were taken. The crystal size was measured from each micrograph and the average size was calculated.
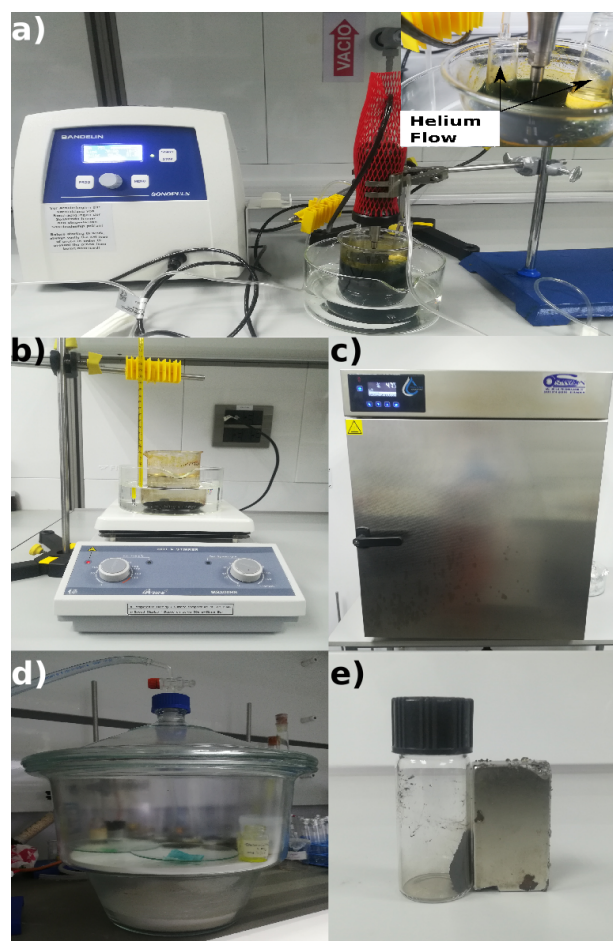
Figure 3.5: Synthesis of the MNPs. a) The solution of ferrous sulfate and sodium hydroxide sonicated for 30 min assisted by a continuous flow of He for the displacement of O b) The MNPs subjected to a thermal bath at approximately 60°C c-d) The MNPs dried in oven at 50°C or vacuum desiccator respectively. e) MNPs attracted by a strong magnet.

Chapter 4

Results & Discussion

4.1   Computational Results

The results obtained are divided into five important topics. First, the primitive cell of Magnetite (Fe_3O_4) with both symmetries $Fd\bar{3}m$ and *Pmca* are considered for obtaining the parameters that converge the total energy to <1 meV/atom and will be used in this work. Second, the results of the *U* corrections with change of symmetry *Pmca* and their comparison with the experimental data are analyzed. Third, the different cases of Fe_3O_4, *i.e.* nonmagnetic and its two types of symmetry, are analyzed by means of a comparison of its equation of states (EOS) and partial density of states (PDOS). Fourth, the surfaces deployed in Figure 3.2 are studied as they present their own PDOS and surface stability. Finally, the results of synthesis of magnetite nanoparticles (MNPs), computed ultraviolet photoelectron spectroscopy (UPS) and the scanning tunneling microscopy (STM) simulations for each surface are discussed.

4.1.1   Convergence Parameters and U-corrections

Figure 4.1 shows the convergence of the spin-polarized (SP) PBEsol computed total energy per atom versus de cutoff energy (E_{cut}) for Fe_3O_4 with both $Fd\bar{3}m$ and *Pmca* symmetries. The results show that for E_{cut} of 650 eV converges the total energy to less than 1 meV/atom for both symmetries. This E_{cut} of 650 eV will be used throughout all subsequent calculations. After finding the appropriate E_{cut}, the next step is to compute the *k*-point that converges the total energy to less than 1 meV/atm, the result is displayed in Figure 4.2;

for that result it is concluded that an appropriated k-point separation of 0.032 Å^{-1}, that corresponds to a k-point mesh of $7 \times 7 \times 7$ ($5 \times 5 \times 2$) for the Fe_3O_4 with symmetry $Fd\bar{3}m$, space group No. 227 (*Pmca*, space group No. 57).
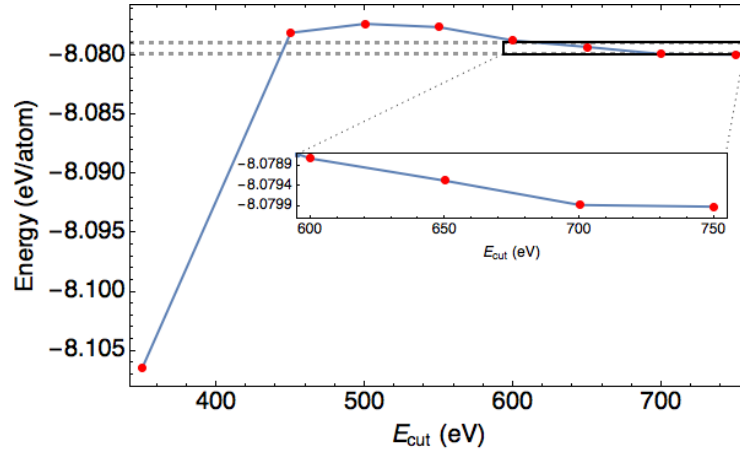

Figure 4.1: Change of the total energy with the energy cutoff for Fe_3O_4 with (a) $Fd\bar{3}m$ and (b) *Pmca* symmetries. The cutoff energy of 650 eV converges the the total energy of Fe_3O_4 was less than 1 meV/atom.
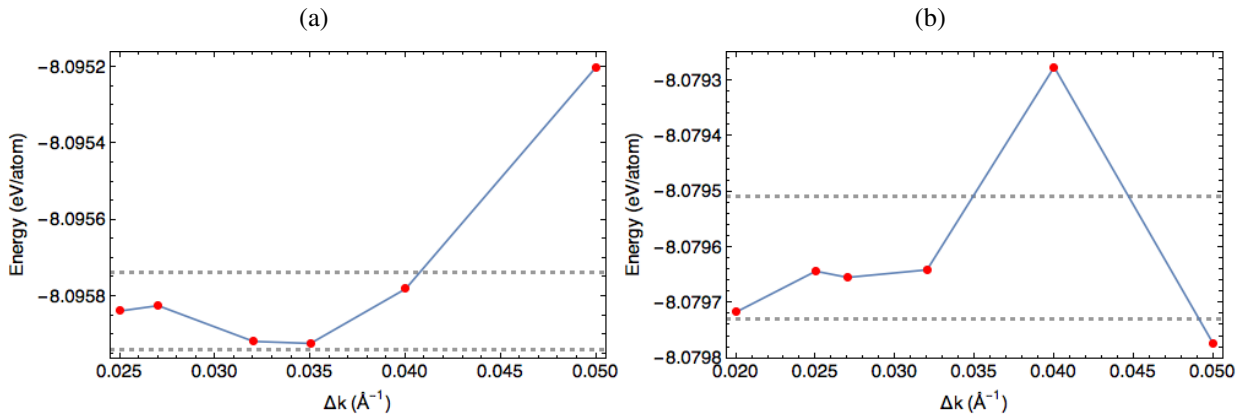

Figure 4.2: Change of the total energy with the k-point mesh for Fe_3O_4 with (a) $Fd\bar{3}m$ and (b) *Pmca* symmetries. The $\Delta k = 0.032$ Å^{-1} converges the total energy to < 1 meV/atom.

Using the above mentioned E_{cut} and k-point mesh that converged the total energy to <1 meV/atom, it is possible to compute the change of the total energy with the volume of the unit cell of Fe_3O_4 with *Pmca*

symmetry. The outcome of the calculation was then fitted to a third order EOS of Birch-Murnagham

$$E(V) = E_0 + \frac{9V_0 B_0}{16} \left\{ \left[\left(\frac{V_0}{V} \right)^{\frac{2}{3}} - 1 \right]^3 B_0' + \left[6 - 4 \left(\frac{V_0}{V} \right)^{\frac{2}{3}} \right] \right\}, \tag{4.1}$$

where V, E_0, V_0, B_0, and B_0' are the cell volume, ground state energy, optimal volume, bulk modulus, and bulk modulus pressure derivative, respectively.[94,95] By definition, $B_0 = \left[V \frac{\partial^2}{\partial V^2} E(V) \right]_{V \to V_0}$, where $E(V)$ comes from the EOS.
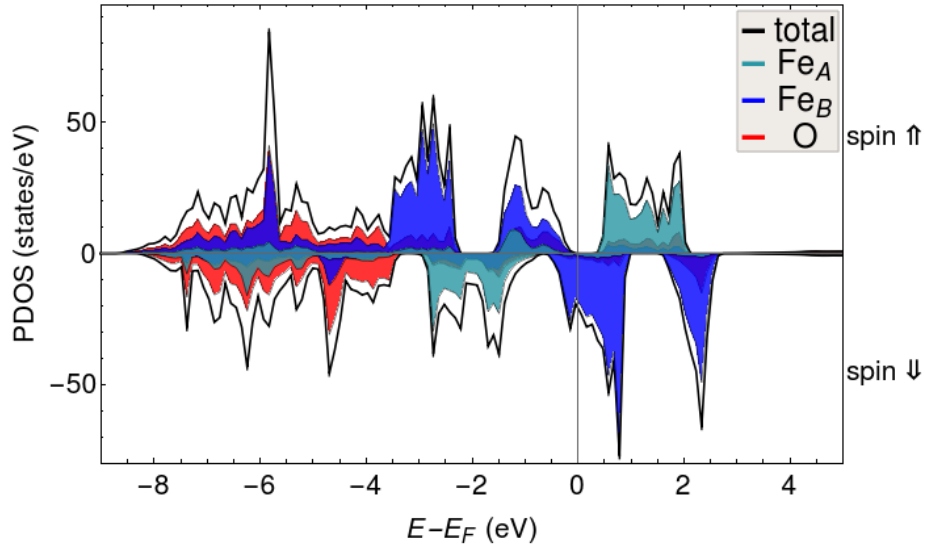

Figure 4.3: PBEsol computed PDOS for the optimal structure of Fe_3O_4 *Pmca* without U-corrections (*i.e.*, $U=0$ eV). The band gap is visualized only in the spin up density of states (DOS). PBEsol predicts the low temperature Fe_3O_4 to be metallic. Positive (negative) values of PDOS is for spin up (down). In this figure, the green, blue and red color corresponds to Fe_A, Fe_B and O states, respectively.

In Figure 4.3, the PDOS correspond to the optimal Fe_3O_4 with symmetry *Pmca* is shown. The density of states indicates the number of quantum states per an interval of energy. In this system, there is no band gap thus PBEsol predicts Fe_3O_4 below T_V with metallic character. However, experimentally it has been measured that the Fe_3O_4 with *Pmca* symmetry has an band gap of 0.14 eV. This results is the reason why U-corrections are used to improve the density-functional theory (DFT) calculations. The range of corrections used was from 0 to 5 eV including 3.5 and 4.5 eV. The U-corrections are applied to reproduce the experimental band gap. Table 4.1 shows some computed physical properties for a given U value. It

is important to stress that for each value of U we computed the EOS and from the corresponding optimal volume, the physical properties were calculated.

Figure 4.4 displays the band gap values found for each U-correction. Those values were interpolated in order to find the value of U=3.85 eV for which the band gap is close to the experimental value. This value of U unfolds throughout the following calculations. In summary, the optimum volume obtained was 590.96 Å^3 and bulk modulus of 182.392 GPa with a band gap ≈ 0.14 eV.
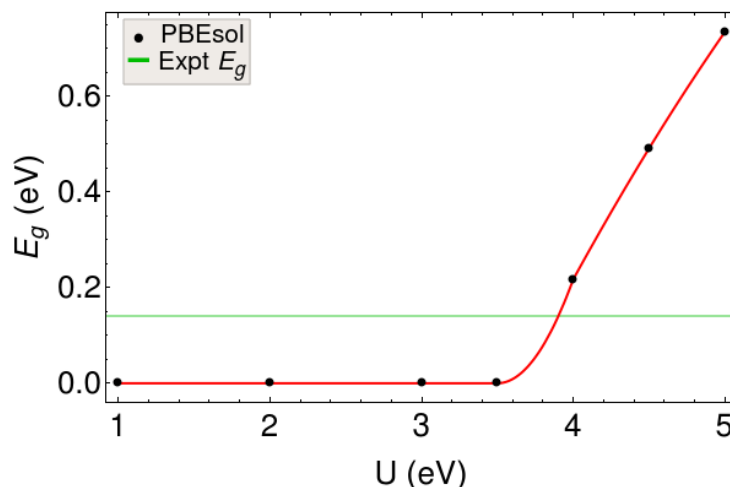

Figure 4.4: Comparison of computational and experimental results for the band gap value E_g of Fe_3O_4 with symmetry Pmca. The interpolation suggests an E_g of 0.14 eV $U = 3.85$ eV.[8]

4.1.2   Stability of Magnetite Phases by the Verwey Transition

In this work we do not intend to explain the mechanism of the Verwey transition, but it is very important to show that PBEsol+U predicts correctly the stability of the system if it is compared the structure below T_V (symmetry *Pmca*, No. 57) with the one above T_V (symmetry $Fd\bar{3}m$, No. 227). In addition it is relevant to check the stability of the magnetic phases. Figure 4.5a shows that ferrimagnetic (FiM) cubic system with $Fd\bar{3}m$ symmetry is energetically more stable than the non-magnetic (NM) system. In the NM case, the total energy was -45.24 eV/fu. (fu.=formula unit Fe_3O_4) for an optimum volume of 63.28 Å^3/fu. while for the FiM case the total energy was -50.70 eV/fu. for an optimum volume of 73.24 Å^3/fu. These values demonstrate that for cubic system with $Fd\bar{3}m$ symmetry the FiM state is -5.46 eV/fu. more stable than the

Table 4.1: Computed PBESol+UEOS for Fe_3O_4 with symmetry *Pmca* for different value of U in eV. In this table, V_0, B_0, E_g, m_{tot} are the optimal volume, the bulk modulus and the total magnetic moment per fu.,respectively.

U(eV)	V_0 (Å^3)	B_0 (GPa)	E_g (eV)	m_{tot} (μ_B/fu.)
0.0	563.789	184.5	0.0	4.0
1.0	572.497	188	0.0	4.0
2.0	580.374	186.2	0.0	4.0
3.0	585.863	186.1	0.0	4.0
3.5	585.863	182.6	0.0	4.0
3.85	590.960	182.4	0.14	4.0
4.0	591.749	180.2	0.22	4.0
4.5	591.749	180.7	0.49	4.0
5.0	591.749	180.7	0.73	4.0

NM state. Experiments at temperatures below T_V shown that the most stable configuration for the Fe_3O_4 is monoclinic with *Pmca* symmetry.

Table 4.2: PBEsol+U(3.85) computed bulk properties for FiM Fe_3O_4 with symmetry 57 and 227 and NM with symmetry 227. Here ΔE is the energy difference with respect to the FiM-57 system.

System	a (Å)	b (Å)	c (Å)	$\alpha = \beta = \gamma$ (°)	V_0 (Å^3/fu.)	B_0 (GPa)	ΔE (eV/fu.)
FiM-57	5.968	5.925	16.713	90	73.87	182.4	0.0
FiM-227	5.917	5.917	5.917	60	73.24	188.1	0.26
NM-227	5.636	5.636	5.636	60	63.28	246.0	5.46

Figure 4.5b shows that the FiM system with *Pmca* symmetry is 0.266 eV/fu., more stable than the FiM cubic system with $Fd\overline{3}m$ symmetry. In the monoclinic system with *Pmca* symmetry, the total energy was -50.962 eV/fu., for an optimum volume of 73.87 Å^3/fu. The system used for the following calculations is the FiM cubic system with $Fd\overline{3}m$ symmetry (FiM-227) because our experimental studies will be performed at room temperature. Table 4.2 shows the values of optimal volume, bulk modulus and the difference in energy between systems.

Figure 4.6 shows the PBEsol + U(3.85) PDOS for the system with symmetry *Pmca*. The band gap is evident for both spin channels. However, PDOS for the FiM cubic system with $Fd\overline{3}m$ symmetry, the band gap disappears as shown in Figure 4.7. In Figure 4.6, the upper valence band (UVB), located between -8.5 to 0 eV, the lower part is mainly composed by Fe_B-3d (Fe_A-3d) states on the spin up (down) channel;
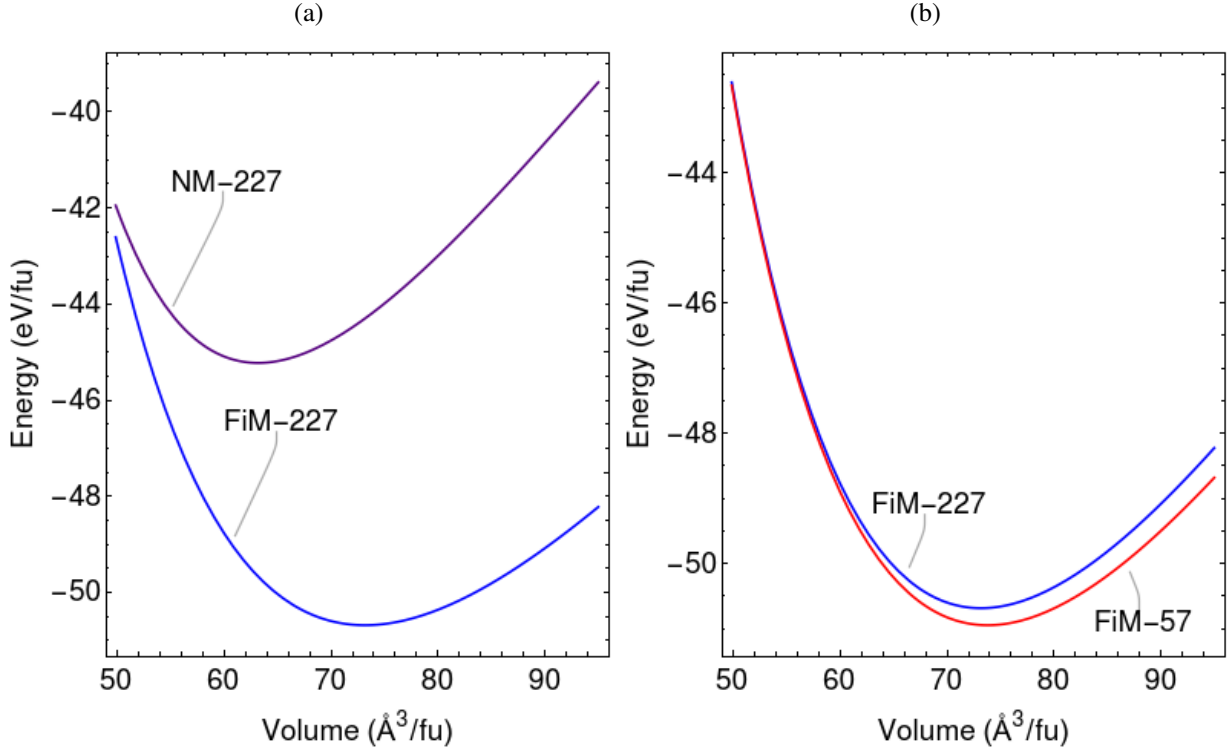
Figure 4.5: Computed PBEsol + U(3.85) EOS for a) NM and FiM Fe_3O_4 both with symmetry $Fd\bar{3}m$; the FiM is 5.46 eV/fu more stable. b) FiM Fe_3O_4 with $Fd\bar{3}m$ (FiM-227) and *Pmca* symmetry (FiM-57), FiM-57 is 0.265 eV/fu more stable.

the states below E_F is composed by Fe_B-3d state on the spin up and O-2p dominates in both channels. At E_F we observe the existence of spin down Fe_B-3d states. The lower conduction band (LCB) is composed mainly by Fe_A-3d (Fe_B-3d) states on the the spin up (down) channel. The electronic structure of FiM with symmetry $Fd\bar{3}m$ is displayed in Figure 4.7; it shows some similarities with the FiM *Pmca*, with the exception of a Fe_B-3d sub-band crossed by the Fermi on the spin down channel.

4.1.3   The Magnetite (100) Surface

Figure 4.8a shows the generic slab with $\left(\sqrt{2} \times \sqrt{2}\right)R45°$ reconstruction obtained by cleaving the unit cell of the FiM-227 system, so the obtained slab is 15 layers thick which are repetitions of the following two main layers: Fe_A and Fe_BO, and this slab has 100 atoms. Additionally, all the models include a 15 Å
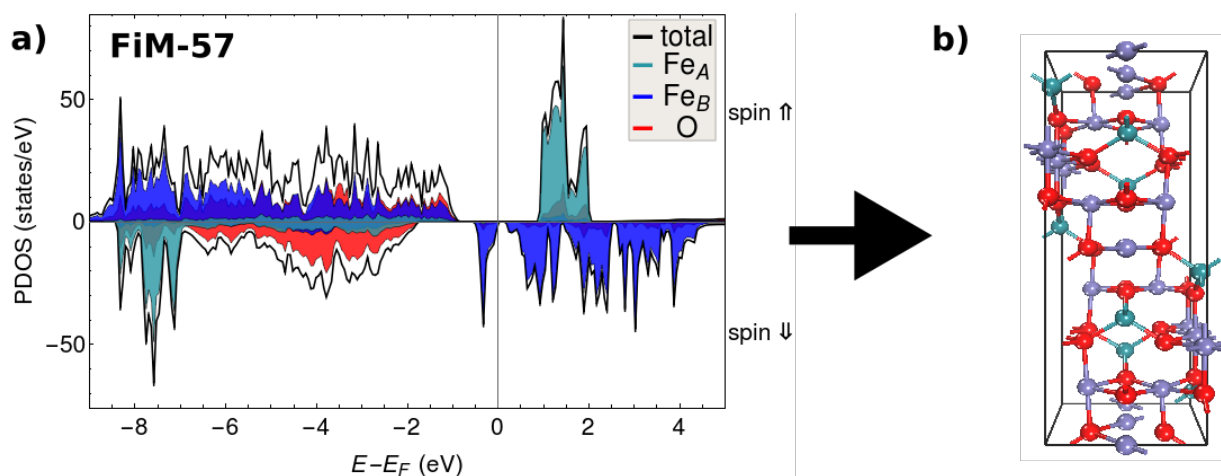
Figure 4.6: PBEsol + $U(3.85)$ computed PDOS for FiM system with *Pmca* symmetry. a) The PDOS shows a clear band gap approximated to 0.14 eV for the spin down and a ~ 2 eV band gap for the spin up. b) Primitive cell of system with symmetry *Pmca*; in this structure the green, blue and red spheres represent the Fe_A, Fe_B and O atoms sites respectively.
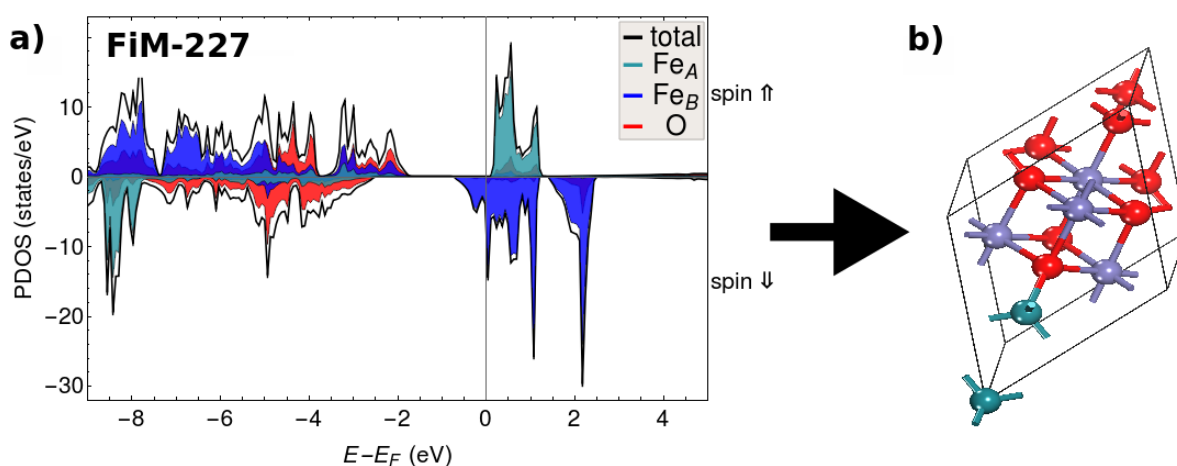

Figure 4.7: PBEsol + $U(3.85)$ computed PDOS for FiM system with $Fd\bar{3}m$ symmetry. The PDOS shows a clear band gap only for the spin up, however the band gap for the spin down is zero. b) Primitive cell of system with symmetry $Fd\bar{3}m$; in this structure the green, blue and red spheres represent the Fe_A, Fe_B and O atoms sites respectively.

vacuum region along the z-axis to neglect the interaction between repeated slabs along the z-direction. In Figure 4.8b, the top view of the slab is instructive to point the surface atomic sites present in the $Fe_3O_4(100)$

surfaces. This slab was modified to create the other cases. From now on the term surface and SFC refers to the first two layers of the system under observation.

Figure 4.9 presents the different cases of surfaces termination according to the type of Fe or O vacancies at the surface. It is important to emphasize that these surface are sketched after full atomic relaxation of the initial systems. The cases studied are divided into two types of surfaces according to the top layers of the system. The first case represents surfaces with termination of Fe_B with and without O vacancies; in this surfaces. All the Fe_A are removed, so the nomenclature used is $SFC - Fe_B$. The variations of this surfaces refer to the two types of O vacancy surface as displayed in Figure 4.8b and Figure 4.9 b-c and named $Fe_B+V_{O_1}$ or $Fe_B+V_{O_2}$. In the Fe_A case, the number of layers is maintained, and the Fe_A are removed or maintained. This case has two variations in which it find one or two Fe_A in the first layer of the surfaces.
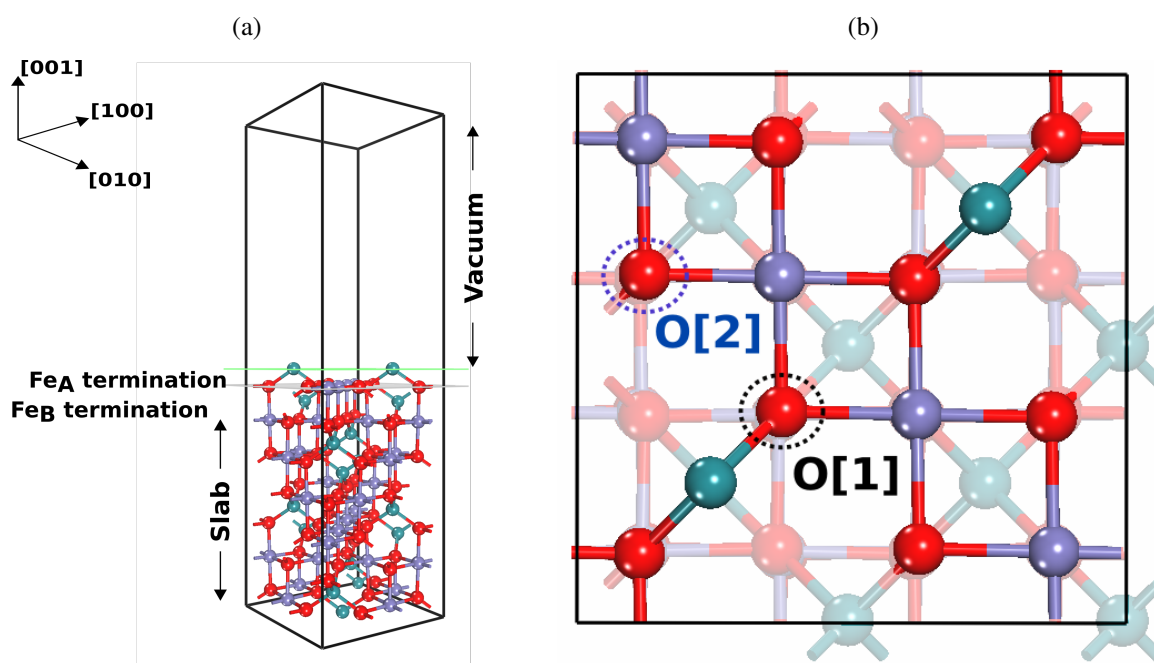

Figure 4.8: Slab model with 15 Å vacuum used to represent the $Fe_3O_4(100)$ with $\left(\sqrt{2} \times \sqrt{2} \right) R45°$ surface reconstruction. a) The total of number layers are 15 where Fe_A layer is represented by green plane while Fe_BO layer is represented by gray plane. b) Top view of the slab showing the four topmost layers of the system. The dotted circles represent the surface oxygen sites that are inequivalent according to whether oxygen binds to one Fe_A and three Fe_B (black circle O1) or only three Fe_B (blue circle O2). Notice that there is one Fe_B atom beneath the oxygen sites.
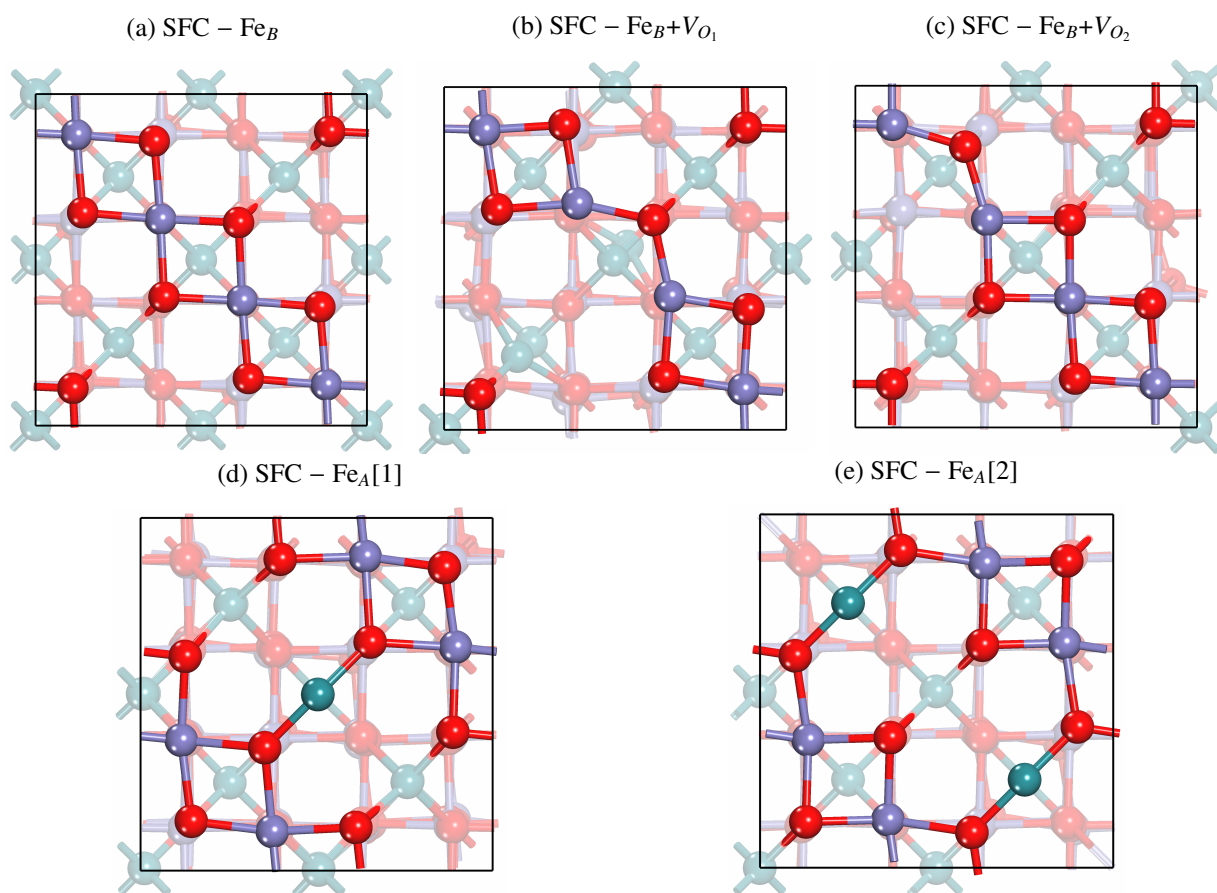
(a) SFC − Fe$_B$ (b) SFC − Fe$_B$+V_{O_1} (c) SFC − Fe$_B$+V_{O_2}

(d) SFC − Fe$_A$[1]   (e) SFC − Fe$_A$[2]

Figure 4.9: Different types of Fe$_3$O$_4$(100) surface; in all figures, the black square line delimits the $\left(\sqrt{2} \times \sqrt{2}\right)R45°$ surface unit cell Fe$_3$O$_4$(100). a-c) Top view of the surface where we notice the termination in Fe$_B$O layer resulting in a slab formed by 13 layers. The type of O vacancy O1, and O2, is present in b) and c) respectively. d-e) Top view of the surface where we noticed the termination in Fe$_A$ layer resulting in a system formed by 15 layers. The surface presents one or two Fe$_A$ respectively.

The nomenclature used is SFC − Fe$_A$[1] for the termination of a single Fe$_A$ and SFC − Fe$_A$[2] for the termination of two Fe$_A$.

Figure 4.10 shows a brief comparison of the PDOS of surfaces studied here. In general terms, the contributions of states include O-2p, O-2s, Fe-3p, Fe-3d and Fe-4s states. In all the cases, the PDOS is computed considering the two topmost layers of the system and from this we can estimate the surface band gap E$_g^{SFC}$. The PDOS for SFC − Fe$_B$ has no band gap, in fact a close look at the Fermi Level we

observe the existence of spin down Fe_B-3d states (See inset of Fig. 4.9 for SFC-Fe_B). The UVB, located between -8.5 to 0 eV, the lower part is mainly composed by Fe_B-3d (Fe_A-3d) states on the spin up (down) channel; the states below E_F is dominated by O-2p states in both channels. The LCB is composed mainly by Fe_A-3d (Fe_B-3d) states on the the spin up (down) channel. The PDOS of $SFC - Fe_B + V_{O_1}$ shows similar characteristics like in $SFC - Fe_B$ except that below E_F we found a sub band formed by spin down Fe_B-3d surface states therefore this system shows a E_g^{SFC}= 0.51 eV (See inset of Fig. 4.9 for SFC-$Fe_B+V_{O_1}$). The PDOS of SFC-$Fe_B+V_{O_2}$ also presents similar composition on the UVB as the $SFC - Fe_B$ but in this case the electronic structure of the UVB below E_F is formed mainly by spin down Fe_B-3d surface states; the E_g^{SFC} observed for this surface is 0.4 eV. The PDOS of $SFC - Fe_A[1]$ also presents similar composition on the UVB as the $SFC - Fe_B$; the E_g^{SFC} observed for this surface is 0.13 eV. Finally, The PDOS of $SFC - Fe_A[1]$ also presents similar composition on the UVB as the $SFC - Fe_B$ with the difference of E_F crosses a band formed by Fe_B-3d surface states, this system is metallic.

$SFC - Fe_B$ is the system with the highest total and surface magnetization. However, in order to better understand this difference, the case of magnetization in surface is discussed. In both cases, $SFC - Fe_A[1]$ and $SFC - Fe_A[2]$, a decrease in magnetization is observed in comparison with $SFC - Fe_B$ because these surfaces have one or two iron cations Fe^{3+} which contributes negatively to the magnetization of the surface.[31] On the other hand, the magnetization of the $SFC - Fe_B+V_{O_1}$ and $SFC - Fe_B+V_{O_2}$ have a small decrease on the surface magnetization compared to $SFC - Fe_B$. This value is explained due to the oxygen vacancy present in these surfaces. The magnetic moment reported by Kurt *et al.* shows values of 1.5 μ_B for the O which would explain the magnetization of $SFC - Fe_B+V_{O_2}$.[96]

Table 4.3: Results of Fe_3O_4(100) surfaces. Here the E_g^{SFC} is obtained from the PDOS of the two topmost layers and m_{SFC} is the SFC magnetic moment of the same layers.

Surface	E_g^{SFC} (eV)	m_{tot} (μ_B)	m_{SFC} (μ_B)
$SFC - Fe_B$	0.0	72	10
$SFC - Fe_B+V_{O_1}$	0.51	72	9.7
$SFC - Fe_B+V_{O_2}$	0.40	68	8.4
$SFC - Fe_A[1]$	0.13	68	6
$SFC - Fe_A[2]$	0.0	64	1
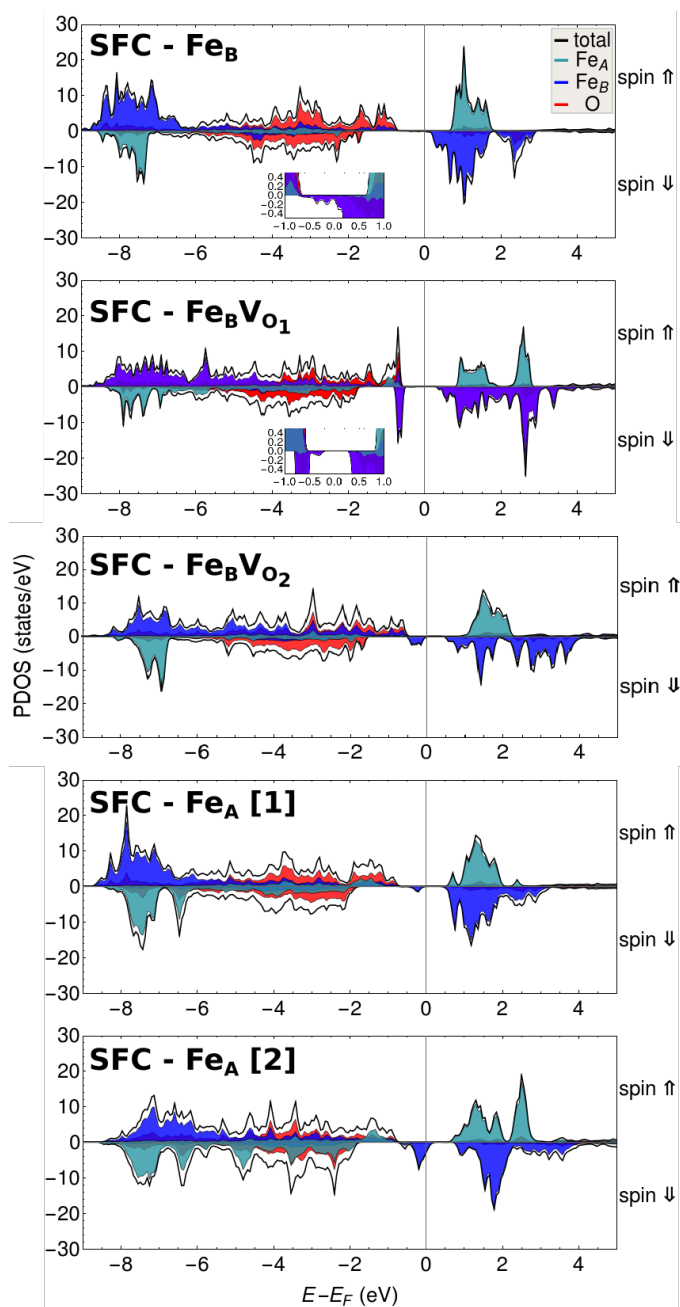
Figure 4.10: PBEsol + $U(3.85)$ computed PDOS for $Fe_3O_4(100)$ surfaces as display in Figure 4.9. In descending order, the PDOS of the different system are shown for $SFC - Fe_B$, $SFC - Fe_B + V_{O_1}$, $SFC - Fe_B + V_{O_2}$, $SFC - Fe_A[1]$, and $SFC - Fe_A[2]$. Notice the zooming around E_F for cases $SFC - Fe_B$ and $SFC - Fe_B + V_{O_1}$. In all the cases, the computed PDOS considers only the two topmost layers.

4.1.4   Surface Free Energy of Magnetite (100)

The surface free energy $\gamma(T, p)$ is defined as the energy related to the formation of a surface from the bulk. In addition, the surface energy includes the interaction with the environment like oxygen. The surface free energy can be simplified considering several factors: i. the surface is in contact with an oxygen atmosphere that acts like a reservoir; ii. the vibrational surface energy is of the order of 10 meV/Å^2;[90] and iii. the fact that there is enough bulk material to act as thermodynamic reservoir thus the chemical potential of Fe and O are related by the Gibbs free energy of the bulk Fe_3O_4.[90] Based in these considerations, in that case the surface free energy can be defined as a function of the oxygen chemical potential μ_O[97]:

$$\gamma(T, p) \approx \frac{1}{2A} \left[E^{slab}(V, N_{Fe}, N_O) - \frac{N_{Fe}}{3} E^{bulk}_{Fe_3O_4}(V) + \left(\frac{4}{3} N_{Fe} - N_O \right) \mu_O(T, p) \right], \qquad (4.2)$$

where E^{slab} and $E^{bulk}_{Fe_3O_4}$ represents the DFT-computed energy of the slab and the bulk material, respectively; N_{Fe} (N_O) represents the number of Fe (O) atoms within the slab.[90] Finally, $\mu_O(T, p)$ represents the O chemical potential and can be related to pressure p and temperature T. For an oxygen environment, if we consider an ideal gas reservoir, it can be expressed as: $\mu_O(T, p) = \mu_O(T, p^\circ) + \frac{1}{2} \ln \left(\frac{p}{p^\circ} \right)$, where $\mu_O(T, p^\circ)$ is the chemical potential at standard pressure $p^\circ = 1$ atm; this values can be computed from tabulated tables from Ref. [D.R. Stull and H. Prophet, JANAF Thermochemical Tables, 2nd ed. U.S. National Bureau of Standards, Washington, DC, 1971], for a detailed description, *e.g.* refer to the work by Reuter *et al*.

Figure 4.11 shows the computed surface energies for models displayed in Figure 4.9 as a function of if the Fe_3O_4(100) surface is interacting with a rich O_2 environment, then the most likely surface to form would depend on the oxygen pressure and temperature that is related to the value of μ_O; in case of a sample prepared at 1 atm at 50 C it would correspond to μ_O=-0.3 eV; *i.e.*, the most likely surface is the $SFC - Fe_B$. This prediction remains beyond the ultra-high vacuum (UHV) ($\approx$-2.5 eV) conditions. Within the range of -2.9 to -2.5 eV for μ_O there is a combination of competing surfaces that is the appearance of $SFC - Fe_B + V_{O_2}$ and $SFC - Fe_A[1]$. Finally, below -2.9 eV the more favorable surface is $SFC - Fe_A[2]$.

4.1.5   Simulation of Ultraviolet Photoelectron Spectroscopy

UPS is related to the occupied density of states of a given sample. The ultraviolet spectral region (UV) radiation of the incident photons can probe efficiently the top layers of the surface making it valuable
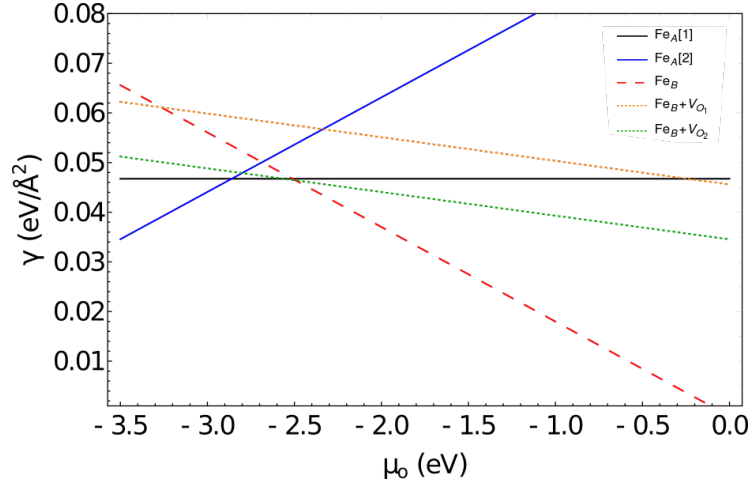
Figure 4.11: Computed surface free energy $\gamma(T, p)$ of the $Fe_3O_4(100)$ surfaces as depicted in Fig. 4.9 and Table 4.3, here the $E_{Fe_3O_4}^{bulk}$ = -50.70 eV and the surface area S = 70.02 Å^2.

for understanding the atomic composition and surface structure. In first approximation, and neglecting possible plasmon effects, the UPS spectrum can be approximated by[90]:

$$I_{\text{UPS}}(E, h\nu) \propto \sum_{i,l} \text{DOS}_{i,l}(E)\sigma_{i,l}(h\nu), \tag{4.3}$$

where E is the photoelectron binding energy, $h\nu$ is the incident photon energy, $\text{DOS}_{i,l}(E)$ are angular-momentum l resolved partial density of states of the ith atom of the unit cell, and $\sigma_{i,l}(h\nu)$ are the angle-integrated, angular-momentum dependent photoionization cross-section. Moreover, in the case of SP systems, the $\text{DOS}_{i,l}(E)$ is the sum of spin-up and -down contributions.
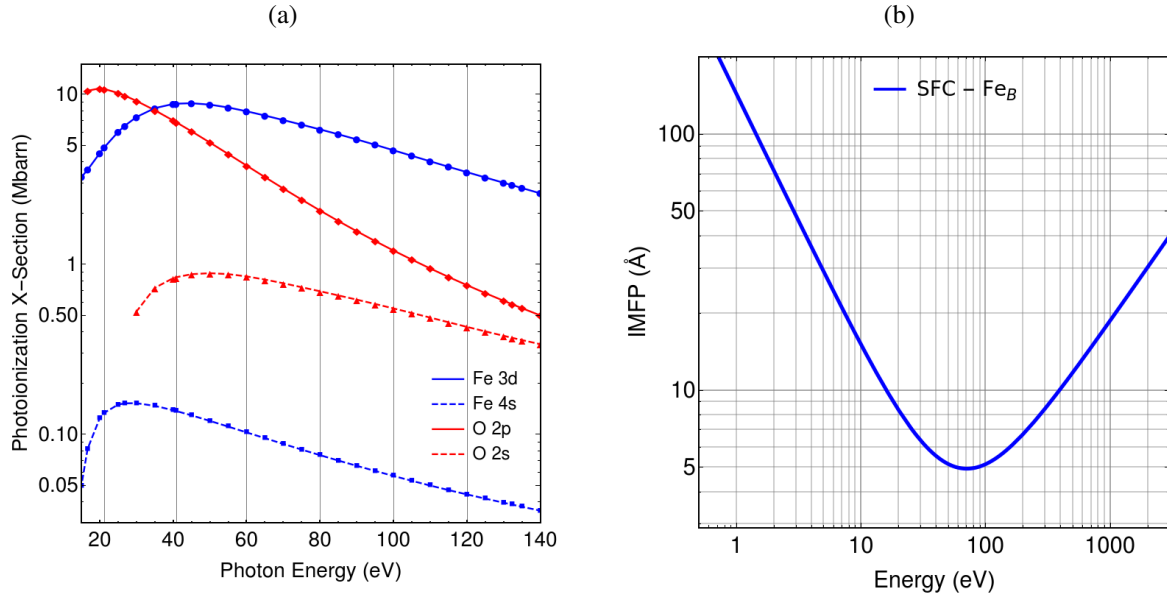
Figure 4.12: a) Photoionization cross-section for Fe-3d, Fe-4s, O-2p and O-2s the X-section corresponding to Fe 3p are not considered since in the upper valence band there is no contribution of these states; adapted from Ref. 98. b) Inelastic mean free path for the SFC−Fe$_B$ system using the model of Tanuma *et al*..[82]

Figure 4.12a shows the values determined by Yeh *et al*. for the photoionization cross-section $\sigma_{i,l}$ for O-2p, O-2s, Fe-3d and Fe-4s for an incident energy interval from 0 to 140 eV.[98] In addition, it is possible to estimate the number of layers that contribute to the DOS$_{i,l}(E)$ by considering the inelastic mean free path (IMFP) for the system under study using the model proposed by Tanuma *et al*.[82]. Figure 4.12b shows the IMFP computed for the system SFC−Fe$_B$. Notice that the maximum surface sensitivity is observed when the photon energy is between 40 and 120 eV and the photoelectrons are generated from a depth of ≈5.5 Å. Similar results for the IMFP was observed for the other slabs.

Figure 4.13 shows the UPS simulation at 21.2 eV. The spectrum shows three important peaks which are located at -7.68, -4.45 and -3.2 eV. The first peak at -7.68 eV receives contributions from the O-2p, Fe$_B$-3d and smaller contribution from the Fe$_A$-3d. Inspecting the PDOS (See Fig. 4.10), the states at -7.68 eV are mainly formed from the Fe-3d states and small contribution of O-2p. The last one is magnified in the UPS (21.2 eV) due to the cross-section value for O-2p at 21.2 eV (See Fig. 4.12a). The second and third peak receive contributions mainly for the O-2p with a minor contribution from the Fe-3d. The peak intensity of the O-2p is greater not only because of the cross-section value but because the O-2p has more

energy states occupied in this energy range (See Fig. 4.10). The rest of the surfaces maintain a similar relationship in terms of the contribution of states for each peak.
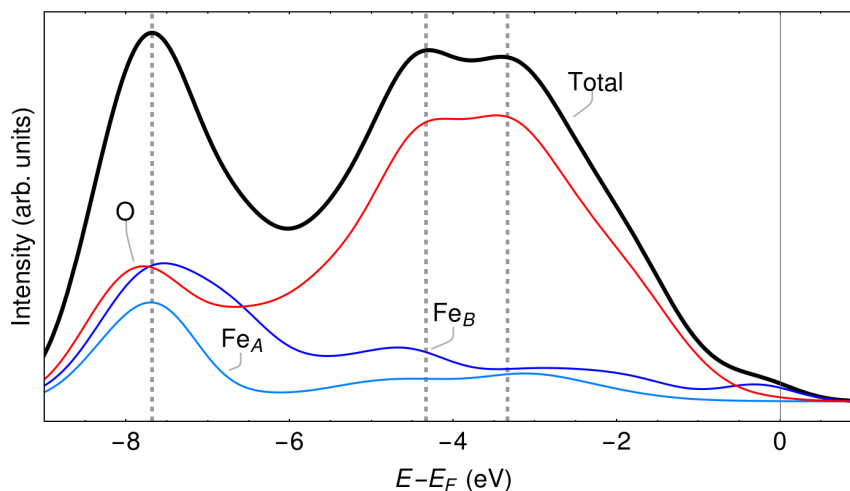

Figure 4.13: Computed UPS for $SFC - Fe_B$ for $hv = 21.1$ eV, the gray lines represent the important peaks in each spectrum.

Figure 4.14 shows the spectra obtained at 40, 60 and 80 eV for each type of surface. Keep in mind that at this energy, the signal is more surface sensitive. Figure 4.14a shows the UPS simulation where it is noticeable three important peaks located at -7.73, -4.4 and -3.2 eV. The first peak at -7.73 eV receives contributions from the electrons Fe-3d and O-2p, but it is the contributions of the Fe that predominate in the spectrum.

Figure 4.14b shows four important peaks at -7.72, -4.25, -3.32 and -0.75 eV for $SFC- Fe_B + V_{O_1}$. The first peak at -7.72 eV presents contributions of both Fe-3d; however, the contribution of the Fe_B-3d is more intense. The second and third peaks shows that Fe-3d contributions are less than O-2p. Once again, the peak at -0.77 eV results from the increase in the intensity of the contributions of Fe_B-3d.

Figure 4.14c shows three important peaks at -7.33, -4.3 and -3 eV for $SFC- Fe_B + V_{O_2}$. The first peak at -7.33 presents contributions mainly from both Fe-3d. The second peak located at -4.3 eV has main O-2p character with a small contribution of Fe-3d. The third peak shows that Fe-3d contributions are less than O-2p. In this case, a shoulder appears instead of a well-defined peak at -0.25 eV due to Fe-3d if it is compared with $SFC - Fe_B + V_{O_1}$.

Figure 4.15a shows two important peaks at -7.5 and -3.75 eV for $SFC-Fe_A[1]$. The first peak at -7.5 eV
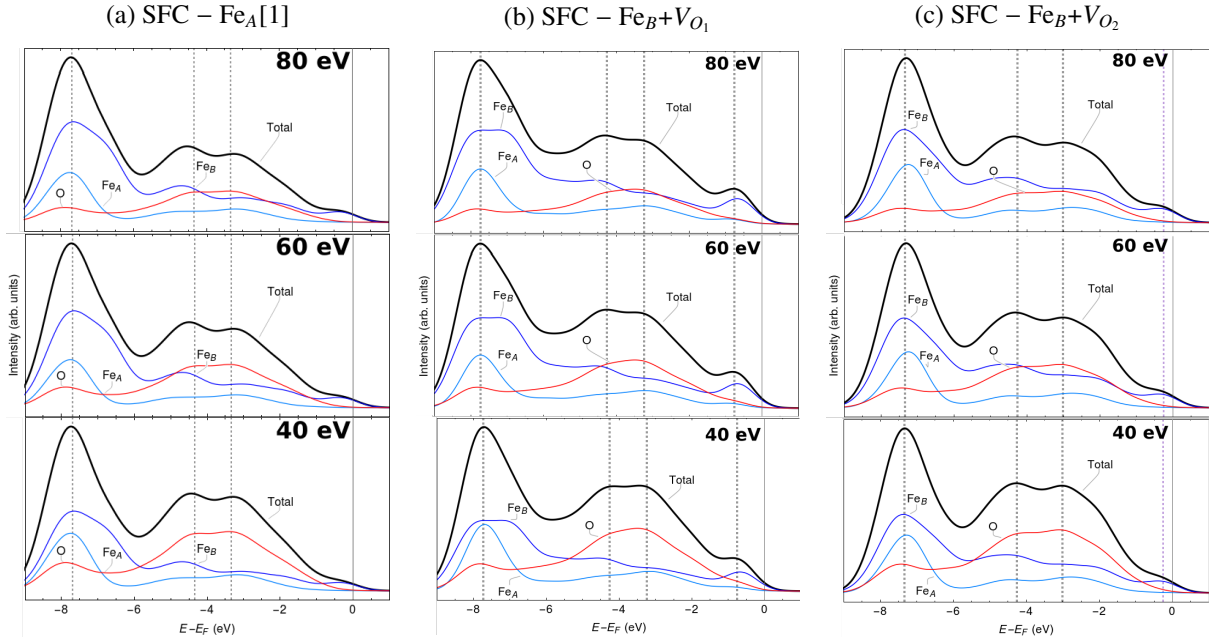
Figure 4.14: Photoemission spectra at 40, 60 and 80 eV for the following surfaces: a) SFC − Fe$_B$ b) SFC − Fe$_B$+V_{O_1}, and c) SFC − Fe$_B$+V_{O_2}. The gray and purple lines represent the important peaks and shoulder, respectively, in each spectrum.

shows a greater contribution from part of the Fe$_A$-3d and Fe$_B$-3d. The peak intensity of Fe$_A$ is comparable to Fe$_B$ due to the last layer of the system (SFC − Fe$_A$[1]). The second peak at -3.75 eV results from the contribution of Fe$_B$-3d and O-2p, it is observed one shoulder at -1.52 eV due to the overlap of less intense peaks of both Fe-3d. A shoulder appears at -0.2 eV as a result of the contribution of Fe$_B$-3d.

Finally, Figure 4.15b shows three important peaks at -7.25, -3.5 and -0.425 eV for SFC− Fe$_A$[2]. A shoulder appear at -6.42 eV. The second peak at -3.5 eV shows that Fe-3d contributions are less than O-2p. The most important feature is the new peak at -0.46 eV due to a greater intensity of the contribution of Fe$_B$-3d.

4.1.6 Simulations of Scanning Tunneling Microscopy

Figure 4.16 shows the simulations carried out with The Vienna *Ab initio* Simulation Package (VASP) and visualized with VESTA to generate the constant height local density of states (LDOS) as obtained with
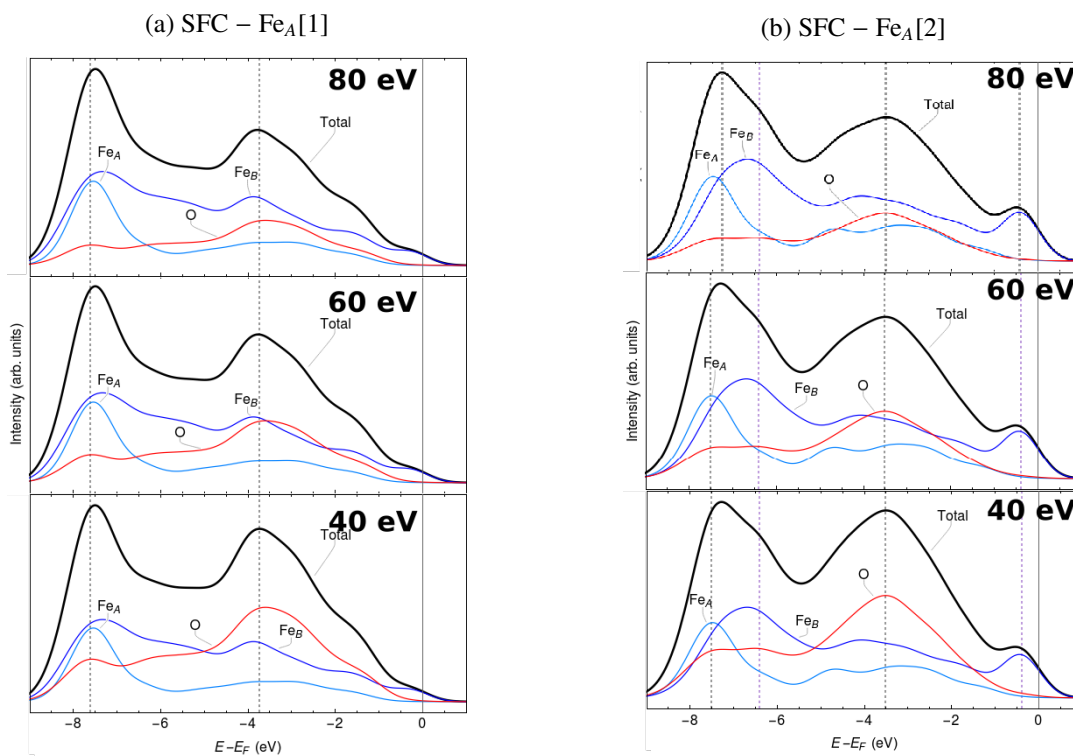
Figure 4.15: Photoemission spectra at 40, 60 and 80 eV for the following surfaces: a) SFC $-$ Fe$_A$[1] and b) SFC $-$ Fe$_A$[2]. The gray and purple lines represent the important peaks and shoulder, respectively, in each spectrum.

VASP from the slab calculations. The presented images come from the LDOS of the unoccupied states of the surface in the interval from the Fermi level (E_F) to E_F+1 eV that is equivalent to a bias voltage (V_{BIAS}) of +1V in the STM experiment. The images are generated at constant height at 4 Å above the topmost surface atom since in STM experiments are expected that tip has an approach of 10 Å.

Figure 4.16a shows the constant height STM image for the SFC-Fe$_B$ for V_{BIAS}=+1 V. In this image, the highest LDOS are located above the surface Fe$_B$ atoms, and it is due to the protrusion towards the vacuum of the Fe$_B$-3d orbitals. However, the PDOS shows the contribution of Fe$_A$ is similar to Fe$_B$, but it does not appear in the simulation. The contribution of the subsurface Fe$_A$-3d to the LDOS is minor since the position is below topmost Fe$_B$ atoms (See Figure 4.9a and Figure 4.10).

Figure 4.16b shows the simulated STM image for SFC-Fe$_B$ + V_{O_2} for V_{BIAS}=+1 V. The primary bright LDOS intensities are located above two surfaces Fe$_B$ that shares one O vacancy, the spots with lower LDOS

intensity are located above the Fe_B sites with no O vacancies, again the origin of this signal is attributed to Fe_B-3d.

Figure 4.16c shows the simulated STM image for SFC−Fe_A[1] for V_{BIAS}=+1 V. The bright spots are located above the surfaces Fe_A sites, and the LDOS is due to the protrusion along with the vacuum of the Fe_A-e_g states. The Fe_B-3d contribution to LDOS is negligible since they are 0.6 Å below the topmost atom. Finally, Figure 4.16d shows the simulated STM image for SFC−Fe_A[2] for V_{BIAS}=+1 V. Similarly to the previous case, the STM image shows bright spots above the surface Fe_A atoms and the LDOS character is mainly Fe-3d e_g.

(a) SFC − Fe$_B$

States/Å^3

3.19E-06
2.90E-06
2.61E-06
2.32E-06
2.03E-06
1.74E-06
1.45E-06
1.16E-06
8.72E-07
5.83E-07
2.93E-07

(b) SFC − Fe$_B$+V_{O_2}

States/Å^3

1.17E-06
1.06E-06
9.46E-07
8.34E-07
7.22E-07
6.10E-07
4.98E-07
3.86E-07
2.74E-07
1.62E-07
5.01E-08

(c) SFC − Fe$_A$[1]

States/Å^3

1.42E-05
1.28E-05
1.41E-05
1.00E-05
8.60E-06
7.19E-06
5.78E-06
4.37E-06
2.96E-06
1.55E-06
1.38E-07

(d) SFC − Fe$_A$[2]

States/Å^3

8.18E-06
7.43E-06
6.68E-06
5.93E-06
5.18E-06
4.43E-06
3.68E-06
2.93E-06
2.19E-06
1.44E-06
6.87E-07
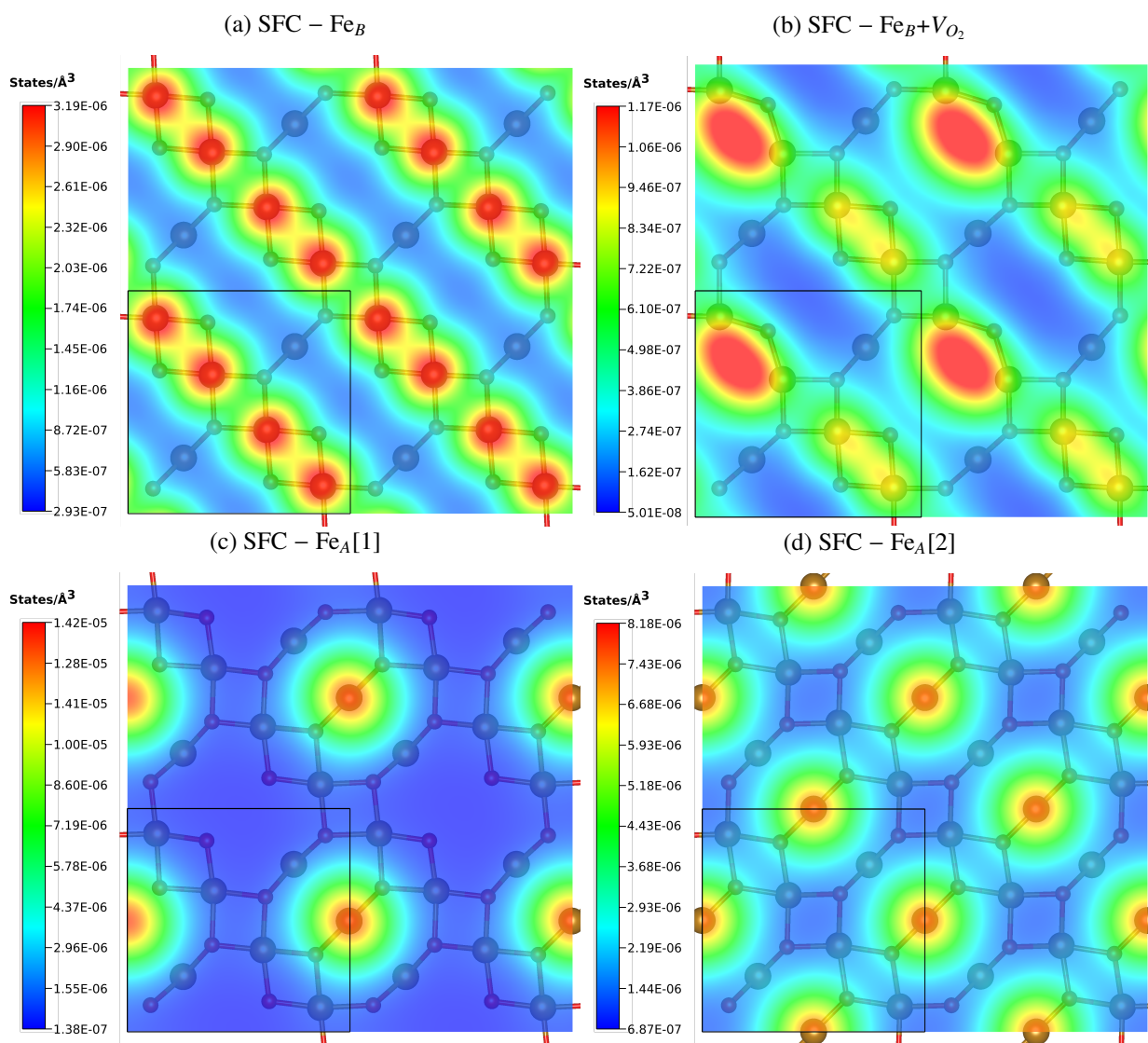
Figure 4.16: Constant high STM image simulation for V$_{BIAS}$ = +1 V (unoccupied states). The color scale shows the LDOS where blue (red) represents the lowest (highest) value. The square in black lines represent the $\left(\sqrt{2} \times \sqrt{2} \right) R45°$ reconstructed structure of each surface.

4.2   Transmission Electron Microscopy

Figure 4.17 shows MNPs from $Fe_3O_4 - A$ and B and the histogram of particle size for $Fe_3O_4 - B$. Figure 4.17a present cubic monocrystalline configurations with uniform and smooth edges and polyhedric configurations with irregular edges. These results agree with the investigations carried out by Vereda *et al.* who uses a similar method with the difference of the origin of Fe cations.[99] According to the image, the MNPs have agglomerated due to the magnetic and van der Waals forces as well as the lack of a coverage agent.[100] The dot diffraction pattern shows that the MNPs are oriented to the direction [100].

Figure 4.18 shows the histogram of the sample particle sizes after a Gaussian adjustment. The average size of the MNPs was 41.75 ± 2 nm with a standard deviation of 0.47 ± 0.07 taking as reference the measured size of the edge of the particle using the ImageJ program. The size of the MNPs is consistent with the investigations of Sugimoto *et al.* and Matijevic *et al.* which indicate that for an excessive concentration of $[OH^-]_{EXC}$=0.046 M, the size of the MNPs should be around 40 nm.[93]

On the other hand, the sample with higher [OH] excess showed a smaller particle size but also the formation of a few goethite particles as shown in Figure 4.17b. The approximate size of these small MNPs was 10 nm. The agglomeration increases due to the little size of the MNPs and the absence of coverage agent.[100] The size of the MNPs is explained by means of a slower direct growth mechanism, as explained in the investigations of Vergés *et al.*[101]

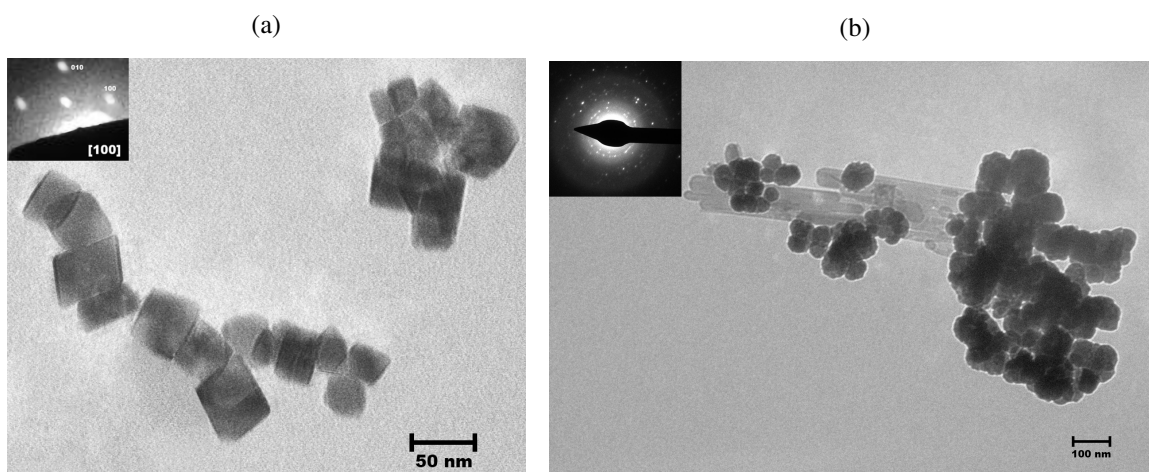(a)   (b)

Figure 4.17: Transmission electron microscopy (TEM) Images for MNPs. a) Image for sample $Fe_3O_4 -$ A b) Image for sample $Fe_3O_4 - B$.
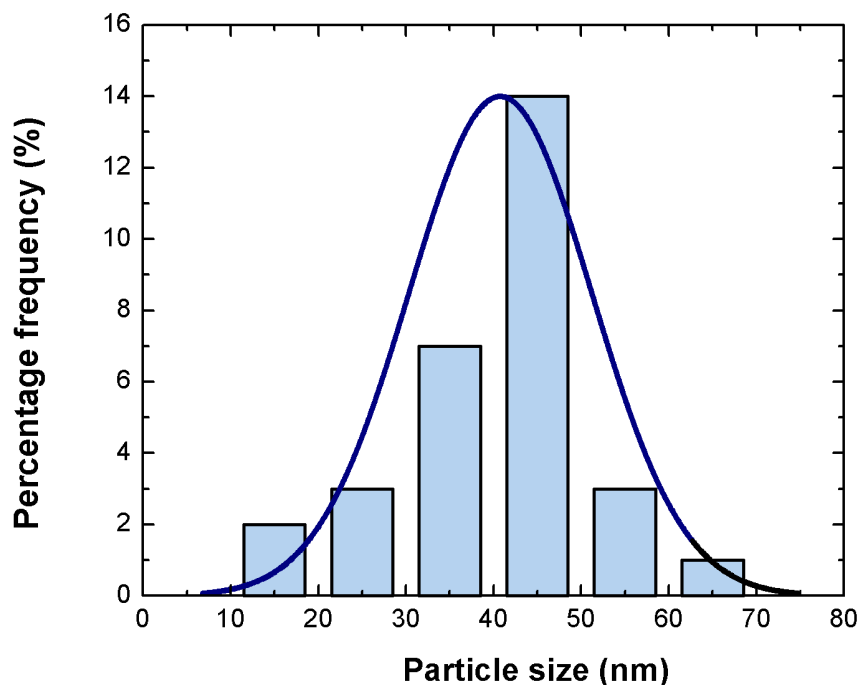
Figure 4.18: Histogram of the size of the $Fe_3O_4 - B$.

4.3   Correlation of computational and experimental data

In this section, the experimental data obtained in the laboratory and recent research are compared with the results obtained in VASP. The comparative results are surface stability, TEM image, UPS spectrum, and STM image. Figure 4.11 shows that $SFC - Fe_B$ is the most stable surface for $\mu_O >$-2.5 eV. This result is in agreement with previous results by Lodziana *et al.*[102] Moreover, according to Santos-Carballal *et al.*, the most energetically likely surface of the Fe_3O_4 are the surfaces (100) next the surfaces (111) and then (110).[15] The synthesis of the MNPs was carried out without O_2 pressure control, but both the results of Figure 4.11 and those presented by Santos-Carballal *et al.* and Ladziana *et al.* agree that the surface (100) is the most favorable above certain oxygen pressures. Figure 4.17a reveals that he morphology of MNPs is observed to have defined edges oriented in the crystallographic direction [100], [010] and [001] (see Fig.4.18). Those surfaces are equivalent to the (100) surfaces studied here. This observation is in agreement with our simulations since that surface is the most likely surface.

The predictions found in section 4.1.5 show great similarity with recent studies. Parkinson *et al.*
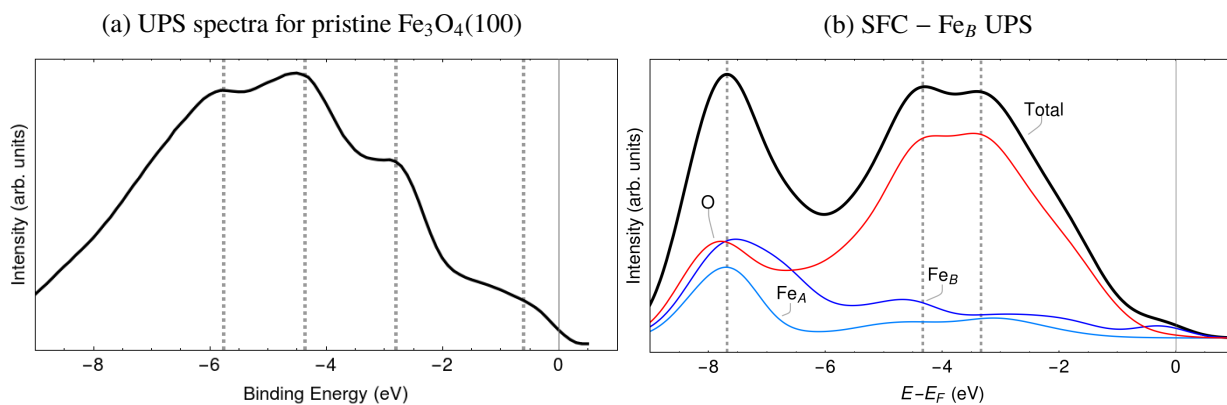
Figure 4.19: Comparison between observed and simulated UPS spectra. a)UPS spectrum for pristine $Fe_3O_4(100)$ for $h\nu = 29$ eV, Adapted from Ref. 103. b) Computed UPS for SCF−Fe_B at 29 eV.

reported a UPS spectrum for pristine $Fe_3O_4(100)$ surface. The sample was annealed in 10^{-6} mbar O_2 at 820 K.[103] The conditions of sample preparation of the Fe_3O_4 surface indicate that the sample is SFC − Fe_B which agrees with Figure 4.11. Figure 4.19a shows the UPS obtained for Parkinson *et al.* with three important peaks at -2.8, -4, and -6 eV and a shoulder located at -0.6 eV. These results agree with Figure 4.19b corresponding to SFC − Fe_B with the only difference of the position of the first peak (around 7 eV) which suffers a right shift of 1.69 eV.

Figures 4.20a and Figures 4.20b show two STM images by Subagyo *et al.*[104] and Mariotto *et al.*[105] for the study of $Fe_3O_4(100)$. Figure 4.20a shows the STM image of a sample growth in O_2 with pressure of between 7.0×10^{-7} and 1.0×10^{-6} mbar and temperature of 523 K. On the other hand, Figure 4.20b shows the STM image of a sample growth in O_2 with pressure remained below 5.0×10^{-10} mbar and temperature of 990 ± 50 K. Figure 4.20c, 4.20d shows the simulations for SFC − Fe_B and SFC − $Fe_B + V_{O_2}$. The STM simulation topology shows a close agreement with the experimental ones as reported by Subagyo *et al.* and Mariotto *et al.*

These results obtained in this section shows the reliability of the DFT calculations made throughout this work. The surface energy depends primarily on the DFT calculations made for each surface. These results allowed us to use the equation proposed by Reuter *et al.* to predict the most stable surface according to the oxygen potential. At the same time, photoemission spectra simulations depend completely on the DOS obtained in VASP. Also the type of surface completely influences the obtaining of the spectrum. The STM simulation depends on the LDOS computed within VASP, the same ones that were carried out once
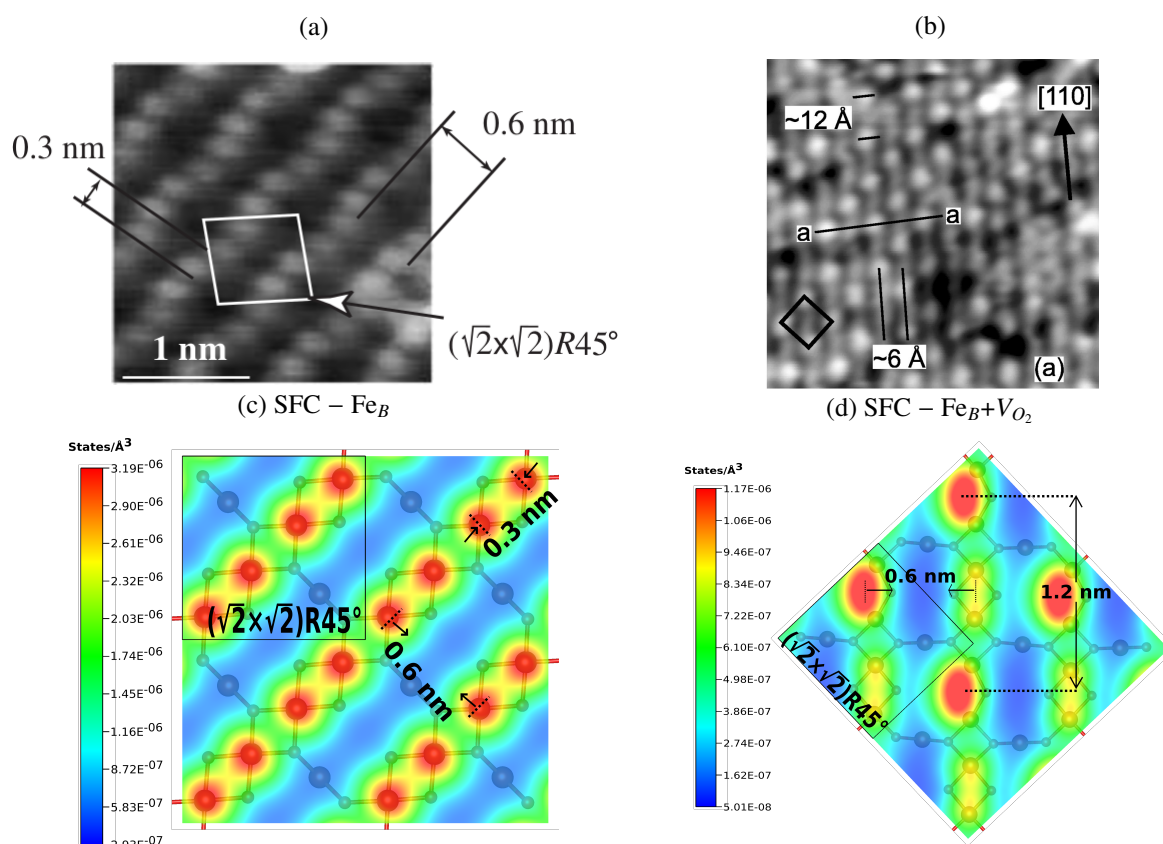
Figure 4.20: Comparison between STM image simulations and experimental results for $Fe_3O_4(100)$. a) experimental STM image obtained for V_{BIAS} = +0.7 V, Adapted from Ref. 104. b) experimental STM for image obtained for V_{BIAS} = +1.0V, Adapted from Ref. 105. c) and d) computed STM image corresponding to $SFC - Fe_B$ and $SFC - Fe_B + V_{O_2}$, respectively.

the electronic and structural properties of Fe_3O_4 surfaces were fully relaxed. Finally, the experimental results show a great congruence with the computational results which demonstrates the veracity of the DFT calculations as well as the possibility of predicting results before the synthesis of $Fe_3O_4(100)$ surfaces.

Chapter 5

Conclusions & Outlook

In this work the study of the electronic properties of Magnetite (Fe_3O_4) bulk and (100) surface were carried out using DFT; and implications in the manufacture of magnetic nanoparticles by a chemical co-precipitation process were analyzed. The electronic properties of bulk Fe_3O_4 and (100) surface were computed using spin-polarized (SP)density-functional theory (DFT) as implemented in The Vienna *Ab initio* Simulation Package (VASP). The PBEsol functional with Hubbard-U corrections, PBEsol+U, proved to be appropriate for the study of Fe_3O_4. The convergence parameters used throughout the work were 650 eV for the cutoff energy and a Δk separation of 0.032 Å^{-1} for the *k*-points. The U correction used was 3.85 eV that reproduces a 0.14 eV band gap as observed for the low temperature Fe_3O_4 with *Pmca* symmetry. The total magnetization for this correction was 4 μ_B/fu., in turn, the optimal volume and bulk modulus were 590.96 Å^3 and 182.39 GPa , respectively.

   The stability of Fe_3O_4 was studied by comparing the total energy per formula unit of different configurations of the Fe_3O_4 including the non-magnetic case. The total energy of the non-magnetic (NM) cubic, ferrimagnetic (FiM) cubic and orthorhombic state were -45.24, -50.7 and -50.96 eV/fu., respectively. The orthorhombic *Pmca* symmetry demonstrates greater stability than the cubic $Fd\bar{3}m$ case. However, the latter is the room temperature phase, making it appropriate for surface studies. Fe_3O_4 surfaces were created by cleaving the unit cell with symmetry $Fd\bar{3}m$ along the plane orientation (100). The SFC-Fe$_B$ and SFC-Fe$_A$[2] present a metallic state while the SFC-Fe$_B$ + V_{O_1}, SFC-Fe$_B$ + V_{O_2} and SFC-Fe$_A$[1] have a band gap. The magnetization on the surface varies between 1 to 10 μ_B/su. The SFC-Fe$_B$, SFC-Fe$_B$ + V_{O_1}, SFC-Fe$_B$ + V_{O_2} border the 10 μ_B/su., while the SFC-Fe$_A$[1] and SFC-Fe$_A$[2] have values of 6 and 1 μ_B/su.,

respectively.

The surface energy for $SFC - Fe_A[1]$ was found to be independent of the chemical potential because it is stoichiometric. The $SFC - Fe_B$ is obtained preferably under rich O_2 conditions. The $SFC - Fe_A[2]$ is synthesized at low O_2 conditions which reinforces the fact of its terminations in Fe_A. At around $\mu_O = -2.6$ eV, there are competitive faces to appear: the $SFC\text{-}Fe_B$, $SFC\text{-}Fe_A[1]$ and $SFC\text{-}Fe_B + V_{O_2}$.

An important part of this work consists in the proper assignation and identification of the simulated ultraviolet photoelectron spectroscopy (UPS) spectra and scanning tunneling microscopy (STM) images with the experimental data. The images provided by Subagyo *et al.*[104] and Mariotto *et al.*[105] show an important relationship with simulations for $SFC - Fe_B$ and $SFC - Fe_B + V_{O_2}$ respectively. The UPS spectra provided by Parkinson *et al.* agrees with $SFC - Fe_B$.[103] The morphology of the magnetite nanoparticles (MNPs) synthesized by the co-precipitation method agrees with the surface energy predictions, *i.e.*, the MNPs show a cubic like structure that involves $Fe_3O_4(100)$ surfaces. However, we presume that the synthesis of MNPs might also involve the formation of some coated thin layer of some O-rich phase of iron oxide around the MNPs as well as the presence of Fe_3O_4 (111) surface on the corner of them. These new factors are interesting to analyze in a future work using DFT calculations to explore the properties of MNPS based on Fe_3O_4.

Appendix A

Results of DFT calculations

(a) U = 0 eV

(b) U = 1 eV

(c) U = 2 eV

(d) U = 3 eV
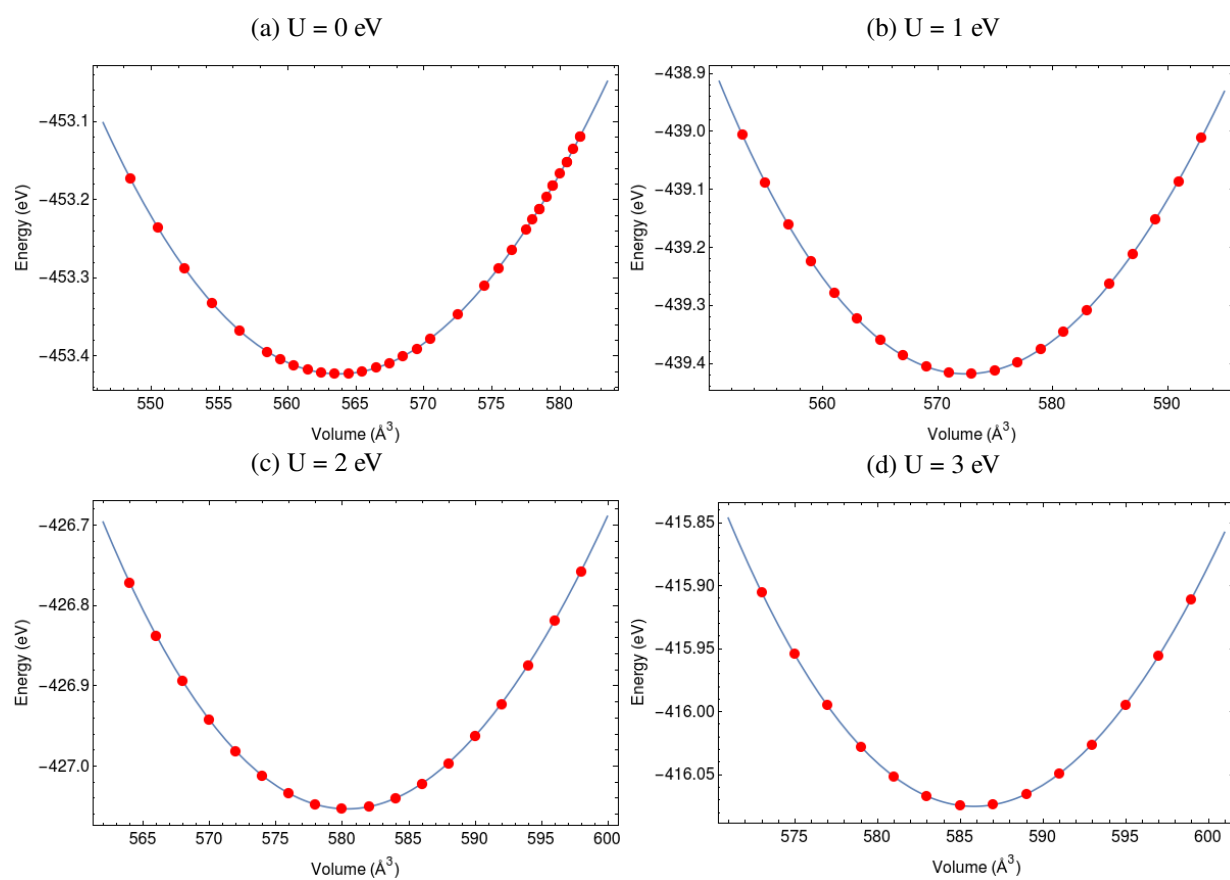
Figure A.1: Adjustment of EOS for each U value in the case of Magnetite (Fe_3O_4) symmetry *Pmca*.
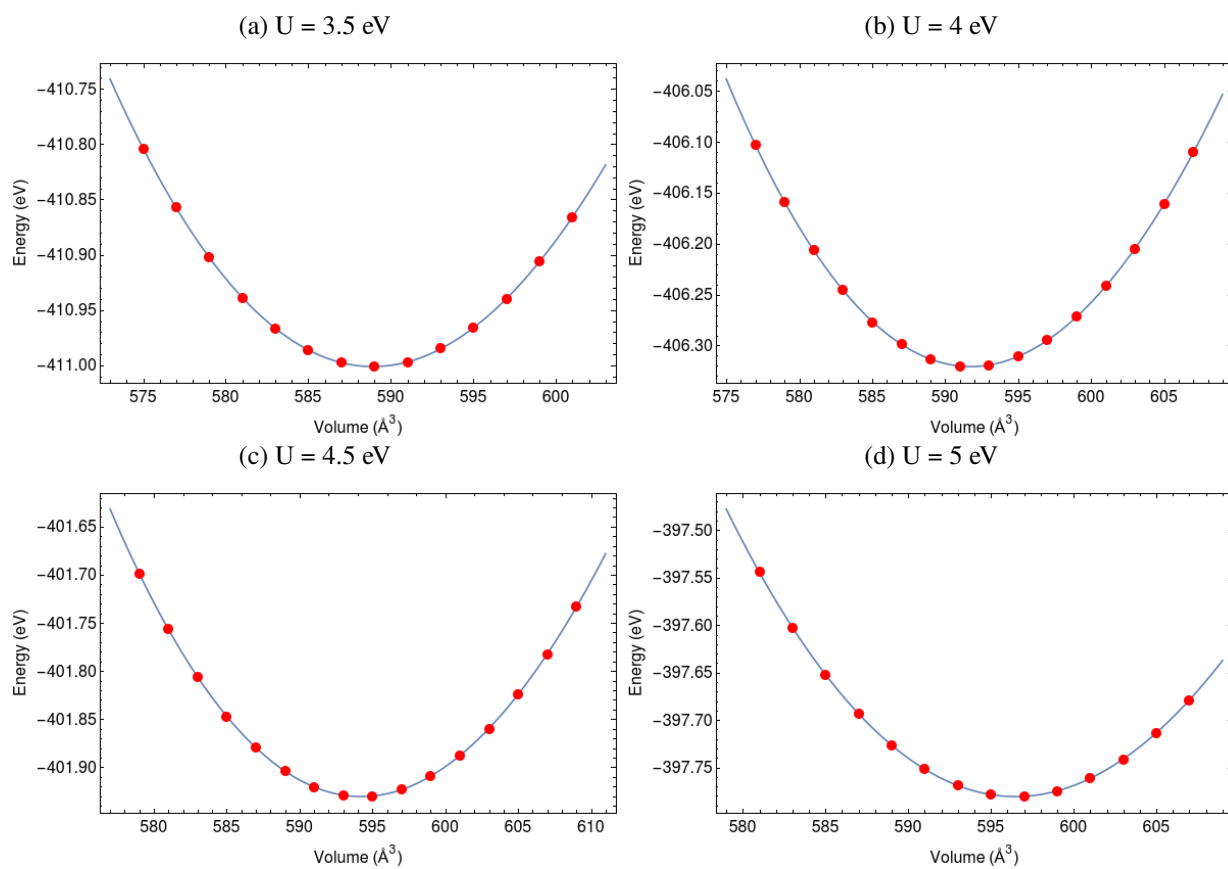
Figure A.2: Adjustment of EOS for each U value in the case of Fe$_3$O$_4$ symmetry *Pmca*.
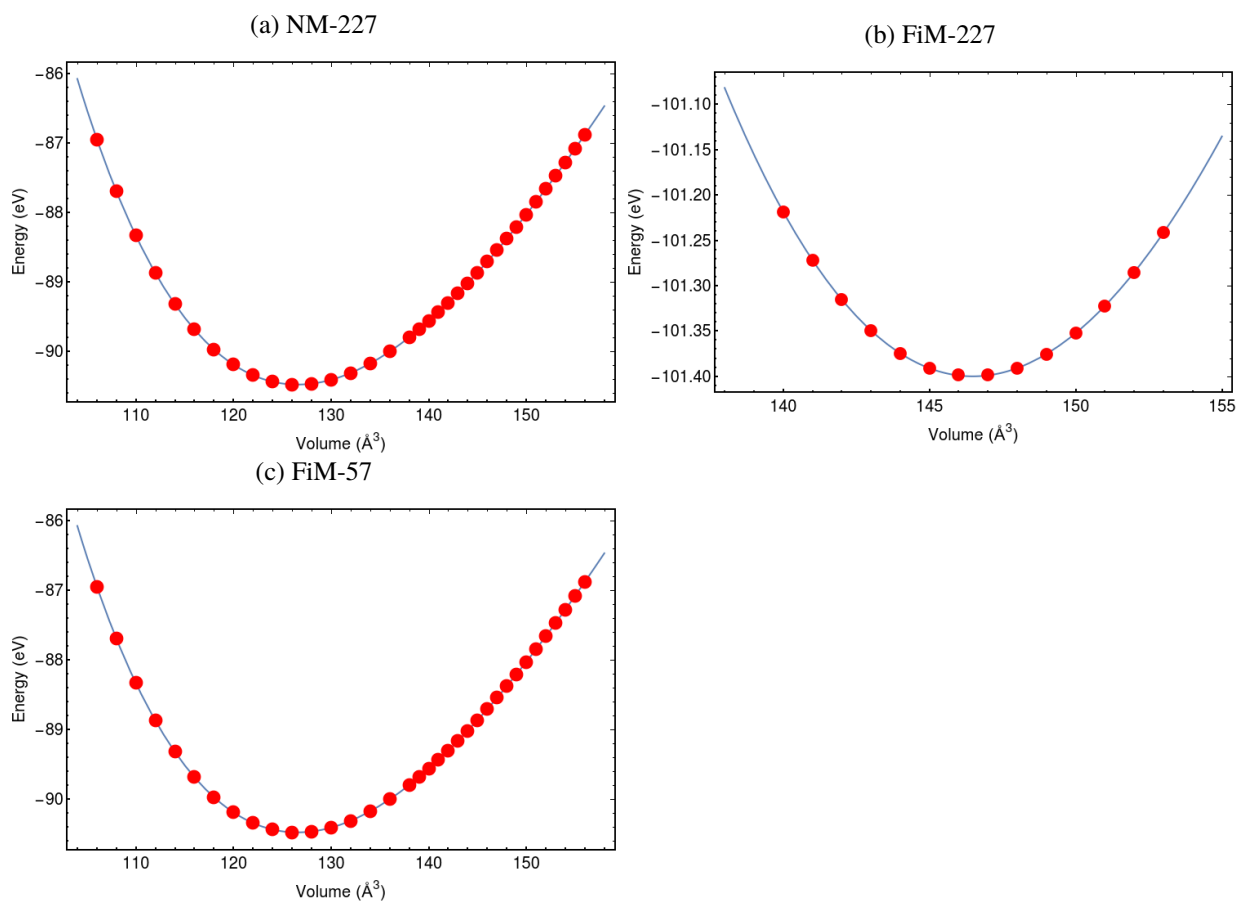
Figure A.3: Adjustment of EOS for different magnetic state for Fe_3O_4. a) NM symmetry $Fd\overline{3}m$ b) FiM symmetry $Fd\overline{3}m$ c) FiM symmetry $Pmca$

(a)

$Fe_A - e_g$

(b)

$Fe_A - t_{2g}$

(c)

$Fe_B - e_g$

(d)

$Fe_B - t_{2g}$
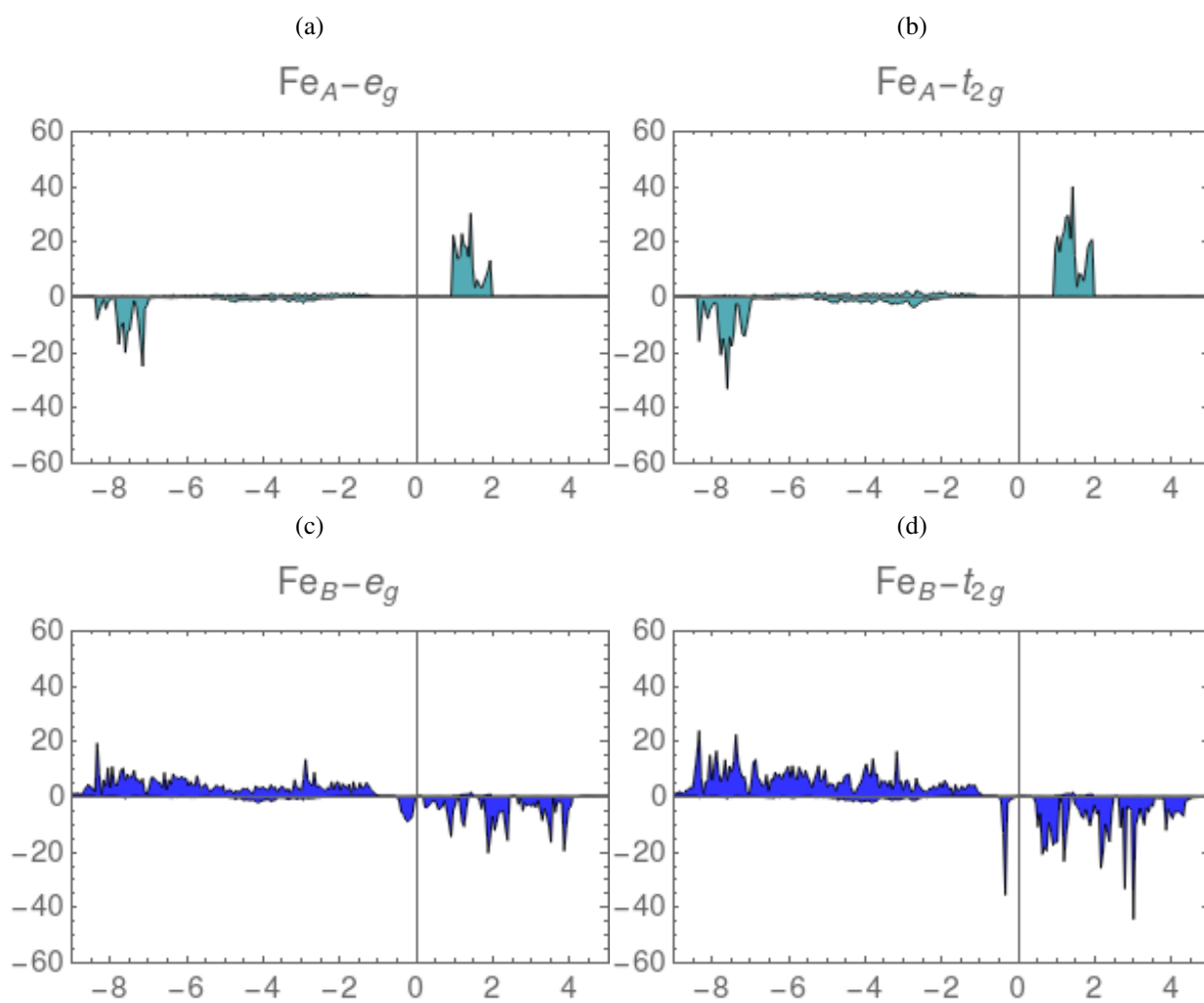
Figure A.4: PDOS of the orbitals of the Fe in the case FiM-57

(a)   (b)

O–px   O–py

(c)

O–pz
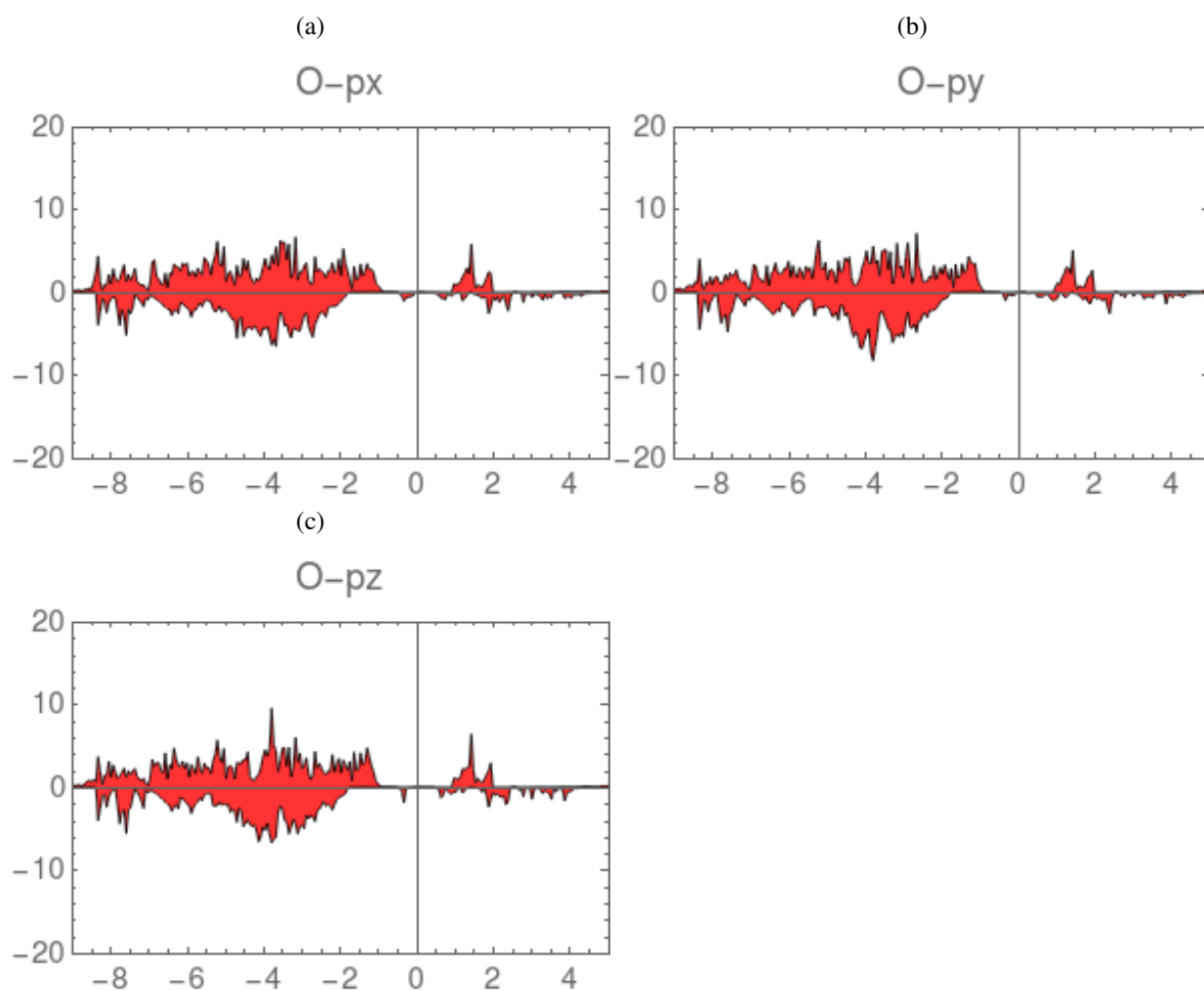
Figure A.5: PDOS of the orbitals of the O in the case FiM-57
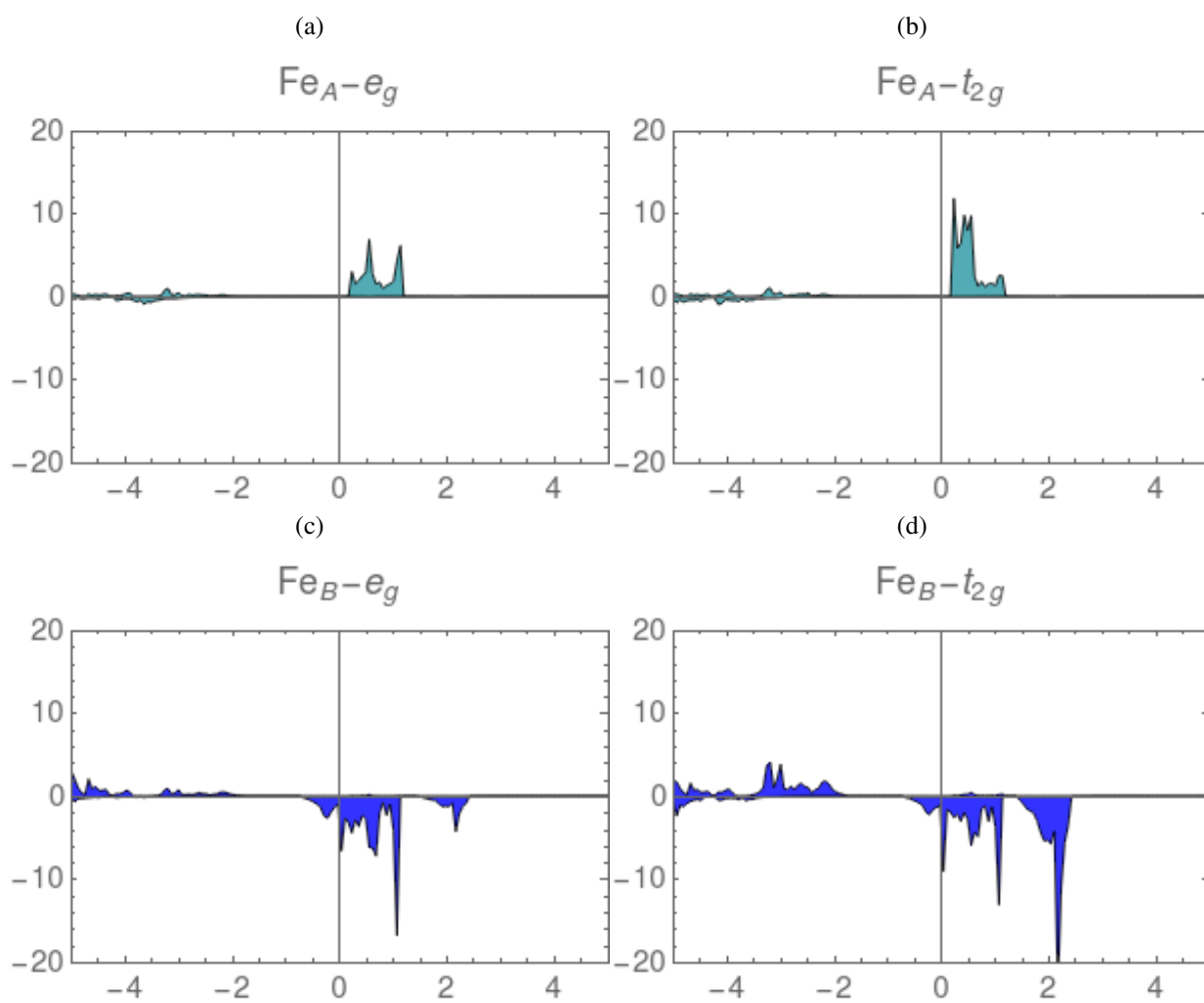
Figure A.6: PDOS of the orbitals of the Fe in the case FiM-227

(a)

(b)

O–px

O–py

O–pz

(c)
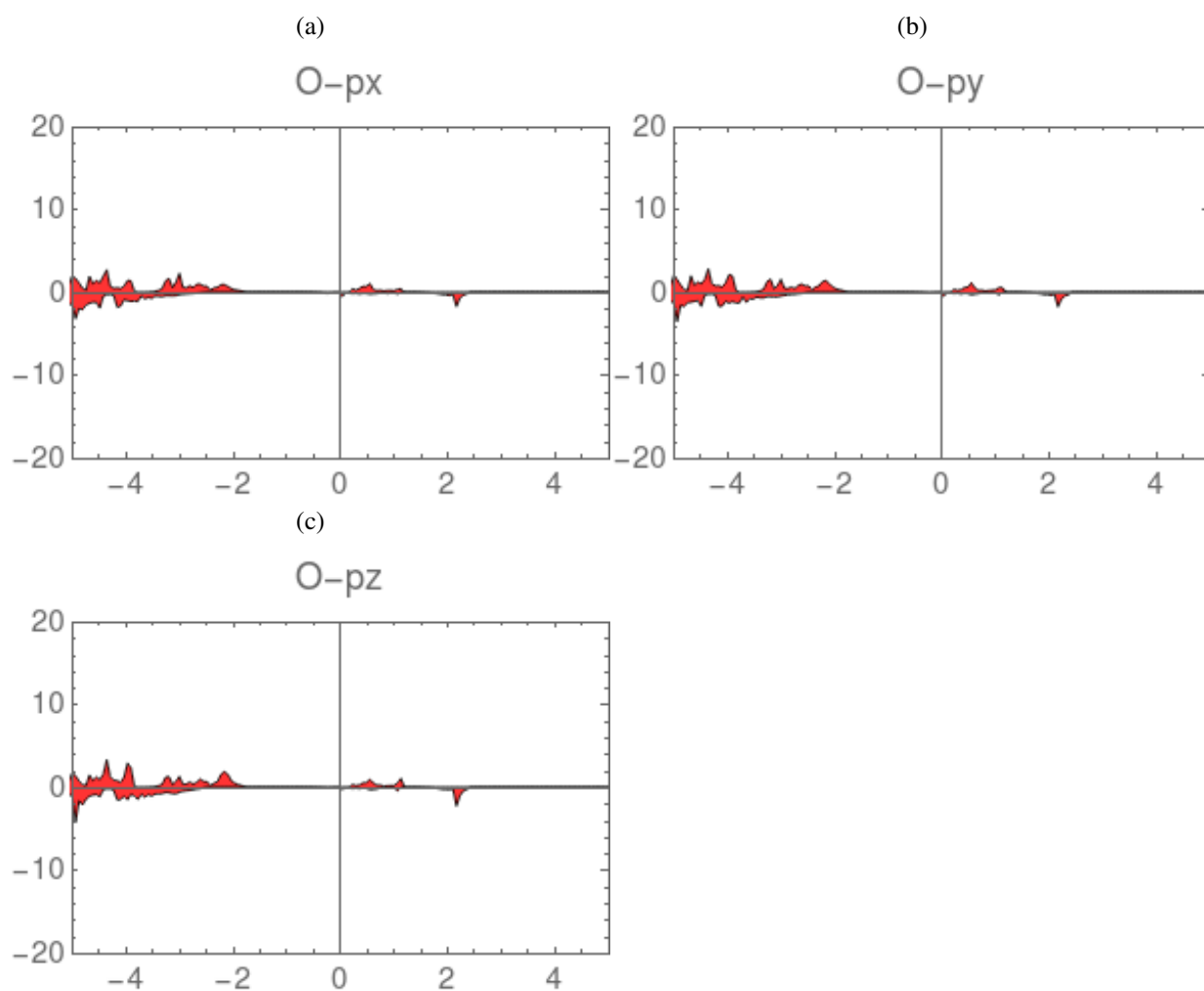
Figure A.7: PDOS of the orbitals of the O in the case FiM-227

Appendix B

Initial file for VASP

Table B.1: INCAR sample.

ELECTRONIC RX	
ISMEAR	-5
SIGMA	0.1
LREAL	auto
PREC	Accurate
ENCUT	650 eV
ALGO	F
FUNCTIONAL	
GGA	PS
SPIN	
ISPIN	2
MAGMOM	2*-5 4*5 8*0
DFT+U	
LDAU	T
LDAUTYPE	2 -1
LDAUL	2 LDAUU
3.0 0.0	
LDAUJ	0.0 0.0
LDAUPRINT	2
LMAXMIX	4
LASPH	T

Table B.2: INCAR sample.

FOR PDOS	
LORBIT	11
NEDOS	900
EMIN	-25
EMAX	15
RELAXATION	
NELMIN	4
MAXMIX	30
IBRION	2
ISIF	4
NSW	50
EDIFFG	-0.02
ADDGRID	T

Bibliography

[1] García, J.; Subías, G. The Verwey transition—a new perspective. *Journal of Physics: Condensed Matter* **2004**, *16*, R145.

[2] Rao, C. N. R.; Gopalakrishnan, J. *NEW DIRECTIONS IN SOLID STATE CHEMISTRY. Edition en anglais*; Cambridge University Press, 1997.

[3] Dunitz, J.; Orgel, L. Electronic properties of transition-metal oxides—I: Distortions from cubic symmetry. *Journal of Physics and Chemistry of Solids* **1957**, *3*, 20–29.

[4] Yuan, C.; Wu, H. B.; Xie, Y.; Lou, X. W. Mixed transition-metal oxides: design, synthesis, and energy-related applications. *Angewandte Chemie International Edition* **2014**, *53*, 1488–1504.

[5] Meyer, J.; Hamwi, S.; Kröger, M.; Kowalsky, W.; Riedl, T.; Kahn, A. Transition metal oxides for organic electronics: energetics, device physics and applications. *Advanced Materials* **2012**, *24*, 5408–5427.

[6] Barsan, N.; Koziej, D.; Weimar, U. Metal oxide-based gas sensor research: How to? *Sensors and Actuators B: Chemical* **2007**, *121*, 18–35.

[7] Sawa, A. Resistive switching in transition metal oxides. *Materials today* **2008**, *11*, 28–36.

[8] Pinto, H.; Elliott, S. Mechanism of the Verwey transition in magnetite: Jahn–Teller distortion and charge ordering patterns. *Journal of Physics: Condensed Matter* **2006**, *18*, 10427.

[9] Walz, F. The Verwey transition-a topical review. *Journal of Physics: Condensed Matter* **2002**, *14*, R285.

[10] Wright, J. P.; Attfield, J. P.; Radaelli, P. G. Charge ordered structure of magnetite Fe 3 O 4 below the Verwey transition. *Physical Review B* **2002**, *66*, 214422.

[11] Runge, E.; Gross, E. K. Density-functional theory for time-dependent systems. *Physical Review Letters* **1984**, *52*, 997.

[12] Sholl, D.; Steckel, J. A. *Density functional theory: a practical introduction*; John Wiley & Sons, 2011.

[13] Carchini, G.; Almora-Barrios, N.; Revilla-López, G.; Bellarosa, L.; García-Muelas, R.; García-Melchor, M.; Pogodin, S.; Błoński, P.; López, N. How theoretical simulations can address the structure and activity of nanoparticles. *Topics in Catalysis* **2013**, *56*, 1262–1272.

[14] Aschauer, U.; Selloni, A. Adsorption of biomedical coating molecules, amino acids, and short peptides on magnetite (110). *The Journal of chemical physics* **2015**, *143*, 044705.

[15] Santos-Carballal, D.; Roldan, A.; Grau-Crespo, R.; de Leeuw, N. H. A DFT study of the structures, stabilities and redox behaviour of the major surfaces of magnetite Fe 3 O 4. *Physical Chemistry Chemical Physics* **2014**, *16*, 21082–21097.

[16] Coey, M. Condensed-matter physics: Charge-ordering in oxides. *Nature* **2004**, *430*, 155.

[17] Li, Y.; Yao, K.; Liu, Z. Structure, stability and magnetic properties of the Fe3O4 (1 1 0) surface: Density functional theory study. *Surface science* **2007**, *601*, 876–882.

[18] Zhu, L.; Yao, K.; Liu, Z. First-principles study of the polar (111) surface of Fe 3 O 4. *Physical Review B* **2006**, *74*, 035409.

[19] Piekarz, P.; Parlinski, K.; Oleś, A. M. Origin of the Verwey transition in magnetite: Group theory, electronic structure, and lattice dynamics study. *Physical Review B* **2007**, *76*, 165124.

[20] Daou, T.; Pourroy, G.; Bégin-Colin, S.; Greneche, J.; Ulhaq-Bouillet, C.; Legaré, P.; Bernhardt, P.; Leuvrey, C.; Rogez, G. Hydrothermal synthesis of monodisperse magnetite nanoparticles. *Chemistry of Materials* **2006**, *18*, 4399–4404.

[21] Mascolo, M.; Pei, Y.; Ring, T. Room temperature co-precipitation synthesis of magnetite nanoparticles in a large pH window with different bases. *Materials* **2013**, *6*, 5549–5567.

[22] Lee, J.; Zhang, S.; Sun, S. High-temperature solution-phase syntheses of metal-oxide nanocrystals. *Chemistry of Materials* **2013**, *25*, 1293–1304.

[23] Awwad, A. M.; Salem, N. M. A green and facile approach for synthesis of magnetite nanoparticles. *Nanoscience and Nanotechnology* **2012**, *2*, 208–213.

[24] Martínez-Mera, I.; Espinosa-Pesqueira, M.; Pérez-Hernández, R.; Arenas-Alatorre, J. Synthesis of magnetite (Fe3O4) nanoparticles without surfactants at room temperature. *Materials Letters* **2007**, *61*, 4447–4451.

[25] Si, S.; Kotal, A.; Mandal, T. K.; Giri, S.; Nakamura, H.; Kohara, T. Size-controlled synthesis of magnetite nanoparticles in the presence of polyelectrolytes. *Chemistry of Materials* **2004**, *16*, 3489–3496.

[26] Roca, A.; Morales, M.; O'Grady, K.; Serna, C. Structural and magnetic properties of uniform magnetite nanoparticles prepared by high temperature decomposition of organic precursors. *Nanotechnology* **2006**, *17*, 2783.

[27] others,, *et al.* In vitro and in vivo experiments with iron oxide nanoparticles functionalized with DEXTRAN or polyethylene glycol for medical applications: magnetic targeting. *Journal of Biomedical Materials Research Part B: Applied Biomaterials* **2014**, *102*, 860–868.

[28] Wiesendanger, R.; Shvets, I.; Bürgler, D.; Tarrach, G.; Güntherodt, H.; Coey, J.; Gräser, S. Topographic and magnetic-sensitive scanning tunneling microscope study of magnetite. *Science* **1992**, *255*, 583–586.

[29] Bishop, S.; Kemeny, P. Photoemission study of the electronic structure of magnetite. *Solid State Communications* **1974**, *15*, 1877–1880.

[30] Andrés, J.; Gracia, L.; Gouveia, A. F.; Ferrer, M. M.; Longo, E. Effects of surface stability on the morphological transformation of metals and metal oxides as investigated by first-principles calculations. *Nanotechnology* **2015**, *26*, 405703.

[31] Kong, L. B.; Liu, L.; Yang, Z.; Li, S.; Zhang, T.; Wang, C. *Magnetic, Ferroelectric, and Multiferroic Metal Oxides*; Elsevier, 2018; pp 287–311.

[32] Spaldin, N. A. *Magnetic materials: fundamentals and applications*; Cambridge University Press, 2010.

[33] Smart, J. S. The Néel theory of ferrimagnetism. *American Journal of Physics* **1955**, *23*, 356–370.

[34] NEEL, L. CITATION CLASSIC-MAGNETIC-PROPERTIES OF FERRITES-FERRIMAGNETISM AND ANTIFERROMAGNETISM. *CURRENT CONTENTS/PHYSICAL CHEMICAL & EARTH SCIENCES* **1984**, 18–18.

[35] Fleet, M. E. The structure of magnetite: Symmetry of cubic spinels. *Journal of Solid State Chemistry* **1986**, *62*, 75–82.

[36] Fleet, M. The structure of magnetite. *Acta Crystallographica Section B: Structural Crystallography and Crystal Chemistry* **1981**, *37*, 917–920.

[37] Fonin, M.; Pentcheva, R.; Dedkov, Y. S.; Sperlich, M.; Vyalikh, D. V.; Scheffler, M.; Rüdiger, U.; Güntherodt, G. Surface electronic structure of the Fe 3 O 4 (100): evidence of a half-metal to metal transition. *Physical Review B* **2005**, *72*, 104436.

[38] Poddar, P.; Fried, T.; Markovich, G. First-order metal-insulator transition and spin-polarized tunneling in Fe 3 O 4 nanocrystals. *Physical Review B* **2002**, *65*, 172405.

[39] Landfester, K.; Ramirez, L. P. Encapsulated magnetite particles for biomedical application. *Journal of Physics: Condensed Matter* **2003**, *15*, S1345.

[40] Mürbe, J.; Rechtenbach, A.; Töpfer, J. Synthesis and physical characterization of magnetite nanoparticles for biomedical applications. *Materials Chemistry and Physics* **2008**, *110*, 426–433.

[41] Eerenstein, W.; Palstra, T.; Saxena, S.; Hibma, T. Spin-polarized transport across sharp antiferromagnetic boundaries. *Physical review letters* **2002**, *88*, 247204.

[42] Majewski, P.; Thierry, B. Functionalized magnetite nanoparticles synthesis, properties, and bio-applications. *Critical Reviews in Solid State and Materials Sciences* **2007**, *32*, 203–215.

[43] Wang, S. X.; Bae, S.-Y.; Li, G.; Sun, S.; White, R. L.; Kemp, J. T.; Webb, C. D. Towards a magnetic microarray for sensitive diagnostics. *Journal of Magnetism and Magnetic Materials* **2005**, *293*, 731–736.

[44] Yang, D.; Hu, J.; Fu, S. Controlled synthesis of magnetite- silica nanocomposites via a Seeded Sol-gel approach. *The Journal of Physical Chemistry C* **2009**, *113*, 7646–7651.

[45] others,, *et al.* Polypyrrole-interface-functionalized nano-magnetite epoxy nanocomposites as electromagnetic wave absorbers with enhanced flame retardancy. *Journal of Materials Chemistry C* **2017**, *5*, 5334–5344.

[46] Barnakov, Y. A.; Scott, B.; Golub, V.; Kelly, L.; Reddy, V.; Stokes, K. Spectral dependence of Faraday rotation in magnetite-polymer nanocomposites. *Journal of Physics and Chemistry of Solids* **2004**, *65*, 1005–1010.

[47] Bruce, I. J.; Taylor, J.; Todd, M.; Davies, M. J.; Borioni, E.; Sangregorio, C.; Sen, T. Synthesis, characterisation and application of silica-magnetite nanocomposites. *Journal of Magnetism and Magnetic Materials* **2004**, *284*, 145–160.

[48] Sen, T.; Sebastianelli, A.; Bruce, I. J. Mesoporous silica- magnetite nanocomposite: fabrication and applications in magnetic bioseparations. *Journal of the American Chemical Society* **2006**, *128*, 7130–7131.

[49] Rajput, S.; Pittman Jr, C. U.; Mohan, D. Magnetic magnetite (Fe3O4) nanoparticle synthesis and applications for lead (Pb2+) and chromium (Cr6+) removal from water. *Journal of colloid and interface science* **2016**, *468*, 334–346.

[50] Patterson, J. D.; Bailey, B. C. *Solid-state physics: introduction to the theory*; Springer Science & Business Media, 2007.

[51] Gilbert, T. Hohenberg-Kohn theorem for nonlocal external potentials. *Physical Review B* **1975**, *12*, 2111.

[52] Pople, J. A.; Gill, P. M.; Johnson, B. G. Kohn—Sham density-functional theory within a finite basis set. *Chemical physics letters* **1992**, *199*, 557–560.

[53] Geerlings, P.; De Proft, F.; Langenaeker, W. Conceptual density functional theory. *Chemical reviews* **2003**, *103*, 1793–1874.

[54] Dobson, J. F. Harmonic-potential theorem: Implications for approximate many-body theories. *Physical review letters* **1994**, *73*, 2244.

[55] Kümmel, S.; Kronik, L. Orbital-dependent density functionals: Theory and applications. *Reviews of Modern Physics* **2008**, *80*, 3.

[56] Ceperley, D. M.; Alder, B. Ground state of the electron gas by a stochastic method. *Physical Review Letters* **1980**, *45*, 566.

[57] Fiolhais, C.; Nogueira, F.; Marques, M. A. *A primer in density functional theory*; Springer Science & Business Media, 2003; Vol. 620.

[58] Perdew, J. P.; Burke, K.; Ernzerhof, M. Generalized gradient approximation made simple. *Physical review letters* **1996**, *77*, 3865.

[59] Zhu, J.; Wang, X.; Louie, S. G. First-principles pseudopotential calculations of magnetic iron. *Physical Review B* **1992**, *45*, 8887.

[60] Wang, L.; Maxisch, T.; Ceder, G. Oxidation energies of transition metal oxides within the GGA+ U framework. *Physical Review B* **2006**, *73*, 195107.

[61] Phillips, J. C. JC Phillips and L. Kleinman, Phys. Rev. 116, 287 (1959). *Phys. Rev.* **1959**, *116*, 287.

[62] Finocchi, F. Density Functional Theory for Beginners: Basic Principles and Practical Approaches. 2011.

[63] Kantorovich, L. *Quantum theory of the solid state: an introduction*; Springer Science & Business Media, 2004; Vol. 136.

[64] Al-Jalali, M. A.; Mouhammad, S. A. Phonons Bloch-gruneisen function and its applications to noble metals resistivity, Part I. *International Journal of Pure and Applied Mathematics* **2015**, *102*, 233–245.

[65] Monkhorst, H. J.; Pack, J. D. Special points for Brillouin-zone integrations. *Physical review B* **1976**, *13*, 5188.

[66] Gong, S.-J.; Duan, C.-G.; Zhu, Y.; Zhu, Z.-Q.; Chu, J.-H. Controlling Rashba spin splitting in Au (111) surface states through electric field. *Physical Review B* **2013**, *87*, 035403.

[67] Nath, P.; Chowdhury, S.; Sanyal, D.; Jana, D. Ab-initio calculation of electronic and optical properties of nitrogen and boron doped graphene nanosheet. *Carbon* **2014**, *73*, 275–282.

[68] Kumagai, T.; Izumi, S.; Hara, S.; Sakai, S. Development of bond-order potentials that can reproduce the elastic constants and melting point of silicon for classical molecular dynamics simulation. *Computational materials science* **2007**, *39*, 457–464.

[69] Feynman, R. P. Forces in molecules. *Physical Review* **1939**, *56*, 340.

[70] Hafner, J. Ab-initio simulations of materials using VASP: Density-functional theory and beyond. *Journal of computational chemistry* **2008**, *29*, 2044–2078.

[71] Fernandez-Garcia, M.; Martinez-Arias, A.; Hanson, J.; Rodriguez, J. Nanostructured oxides in chemistry: characterization and properties. *Chemical Reviews* **2004**, *104*, 4063–4104.

[72] Yadav, R.; Dixit, C. Synthesis, characterization and prospective applications of nitrogen-doped graphene: A short review. *Journal of Science: Advanced Materials and Devices* **2017**, *2*, 141–149.

[73] Sikalidis, C. *Advances in Ceramics: Synthesis and Characterization, Processing and Specific Applications*; BoD–Books on Demand, 2011.

[74] Rao, C. N. R.; Basu, P.; Hegde, M. Systematic organic UV photoelectron spectroscopy. *Applied Spectroscopy Reviews* **1979**, *15*, 1–193.

[75] Hüfner, S. *Photoelectron spectroscopy: principles and applications*; Springer Science & Business Media, 2013.

[76] Koyama, R. Y.; Smith, N. V. Photoemission properties of simple metals. *Physical Review B* **1970**, *2*, 3049.

[77] Williams, D. B.; Carter, C. B.; Microscopy, C. T. E. A textbook for Materials Science. 1996.

[78] Eland, J. H. D. *Photoelectron spectroscopy: an introduction to ultraviolet photoelectron spectroscopy in the gas phase*; Elsevier, 2013.

[79] Oura, K.; Lifshits, V.; Saranin, A.; Zotov, A.; Katayama, M. *Surface science: an introduction*; Springer Science & Business Media, 2013.

[80] Tan, Z.; Xia, Y.; Zhao, M.; Liu, X. Electron stopping power and inelastic mean free path in amino acids and protein over the energy range of 20–20,000 eV. *Radiation and environmental biophysics* **2006**, *45*, 135–143.

[81] Zemek, J.; Houdkova, J.; Jiricek, P.; Jablonski, A.; Jurka, V.; Kub, J. Determination of electron inelastic mean free paths for poly [methyl (phenyl) silylene] films. *Polymer* **2009**, *50*, 2445–2450.

[82] Tanuma, S.; Powell, C.; Penn, D. Calculations of electron inelastic mean free paths. IX. Data for 41 elemental solids over the 50 eV to 30 keV range. *Surface and Interface Analysis* **2011**, *43*, 689–713.

[83] Binnig, G.; Rohrer, H. Scanning tunneling microscopy. *Surface science* **1983**, *126*, 236–244.

[84] Hansma, P. K.; Tersoff, J. Scanning tunneling microscopy. *Journal of Applied Physics* **1987**, *61*, R1–R24.

[85] Tersoff, J.; Hamann, D. Theory of the scanning tunneling microscope. *Physical Review B* **1985**, *31*, 805.

[86] Ruska, E. The early development of electron lenses and electron microscopy. *Microscopica acta. Supplement* **1980**, 1–140.

[87] Reimer, L. *Transmission electron microscopy: physics of image formation and microanalysis*; Springer, 2013; Vol. 36.

[88] Fultz, B.; Howe, J. M. *Transmission electron microscopy and diffractometry of materials*; Springer Science & Business Media, 2012.

[89] Williams, D. B.; Carter, C. B. *Transmission electron microscopy*; Springer, 1996; pp 3–17.

[90] Reuter, K.; Scheffler, M. Composition, structure, and stability of RuO 2 (110) as a function of oxygen pressure. *Physical Review B* **2001**, *65*, 035406.

[91] Wu, W.; He, Q.; Jiang, C. Magnetic iron oxide nanoparticles: synthesis and surface functionalization strategies. *Nanoscale research letters* **2008**, *3*, 397.

[92] Laurent, S.; Forge, D.; Port, M.; Roch, A.; Robic, C.; Vander Elst, L.; Muller, R. N. Magnetic iron oxide nanoparticles: synthesis, stabilization, vectorization, physicochemical characterizations, and biological applications. *Chemical reviews* **2008**, *108*, 2064–2110.

[93] Sugimoto, T.; Matijević, E. Formation of uniform spherical magnetite particles by crystallization from ferrous hydroxide gels. *Journal of Colloid and Interface Science* **1980**, *74*, 227–243.

[94] Fu, C.-L.; Ho, K.-M. First-principles calculation of the equilibrium ground-state properties of transition metals: Applications to Nb and Mo. *Physical Review B* **1983**, *28*, 5480.

[95] Birch, F. Finite elastic strain of cubic crystals. *Physical review* **1947**, *71*, 809.

[96] Kurt, O.; Phipps, T. The magnetic moment of the oxygen atom. *Physical Review* **1929**, *34*, 1357.

[97] Woicik, J.; Nelson, E.; Kronik, L.; Jain, M.; Chelikowsky, J. R.; Heskett, D.; Berman, L.; Herman, G. Hybridization and Bond-Orbital Components in Site-Specific X-Ray Photoelectron Spectra of Rutile T i O 2. *Physical review letters* **2002**, *89*, 077401.

[98] Yeh, J.; Lindau, I. Atomic subshell photoionization cross sections and asymmetry parameters: 1 Z 103. *Atomic data and nuclear data tables* **1985**, *32*, 1–155.

[99] Vereda, F.; Rodríguez-González, B.; de Vicente, J.; Hidalgo-Álvarez, R. Evidence of direct crystal growth and presence of hollow microspheres in magnetite particles prepared by oxidation of Fe (OH) 2. *Journal of colloid and interface science* **2008**, *318*, 520–524.

[100] Mahmed, N.; Heczko, O.; Lancok, A.; Hannula, S. The magnetic and oxidation behavior of bare and silica-coated iron oxide nanoparticles synthesized by reverse co-precipitation of ferrous ion (Fe2+) in ambient atmosphere. *Journal of Magnetism and Magnetic Materials* **2014**, *353*, 15–22.

[101] Vergés, M. A.; Costo, R.; Roca, A.; Marco, J.; Goya, G.; Serna, C.; Morales, M. Uniform and water stable magnetite nanoparticles with diameters around the monodomain–multidomain limit. *Journal of Physics D: Applied Physics* **2008**, *41*, 134003.

[102] Łodziana, Z. Surface Verwey transition in magnetite. *Physical review letters* **2007**, *99*, 206402.

[103] Parkinson, G. S.; Mulakaluri, N.; Losovyj, Y.; Jacobson, P.; Pentcheva, R.; Diebold, U. Semiconductor–half metal transition at the Fe 3 O 4 (001) surface upon hydrogen adsorption. *Physical Review B* **2010**, *82*, 125413.

[104] Subagyo, A.; Sueoka, K. Defect-induced charge freezing on epitaxial Fe3O4 (001) film surfaces studied by spin-polarized scanning tunneling microscopy. *Japanese journal of applied physics* **2005**, *44*, 5447.

[105] Mariotto, G.; Murphy, S.; Shvets, I. Charge ordering on the surface of Fe 3 O 4 (001). *Physical Review B* **2002**, *66*, 245426.

Abbreviations

AFM antiferromagnetic 5

BZ Brillouin zone 14–16, 18

CO charge ordering 1, 2, 7

DFT density-functional theory viii, 1–3, 8, 9, 12, 14, 15, 26, 33, 42, 52–55
DOS density of states 2, 20, 25, 26, 33, 52
DP diffraction pattern 21, 22

EOS equation of states 31, 33–36

Fe$_3$O$_4$ Magnetite vii, viii, xii, 1–3, 5–8, 12, 23–29, 31–42, 50–55, 57, 58
FiM ferrimagnetic viii, 1, 5, 24, 34–37, 54
FM ferromagnetic 4, 5

GGA generalized gradient approximation 2, 12, 13, 16, 23

IMFP inelastic mean free path 19, 27, 28, 44

KS Kohn-Sham 9–11, 13, 15–17

LCB lower conduction band 36, 40
LDA local density approximation 11, 12
LDOS local density of states 46–49, 52

MNPs magnetite nanoparticles viii, 2, 3, 7, 8, 28–31, 50, 51, 55

NM non-magnetic 34–36, 54

PAW projector-augmented wave 13, 16

PDOS partial density of states 26, 31, 33, 35, 37, 39–41, 44, 47

PES photoemission spectroscopy 18

SP spin-polarized 12, 23, 31, 43, 54

STM scanning tunneling microscopy viii, 2, 3, 19, 28, 31, 47–49, 51–53, 55

TEM transmission electron microscopy viii, 2, 21, 29, 50, 51

TMOs transition metal oxides 1, 5

UHV ultra-high vacuum 42

UPS ultraviolet photoelectron spectroscopy viii, 2, 3, 18, 27–29, 31, 42–45, 51, 52, 55

UV ultraviolet spectral region 42

UVB upper valence band 35, 40

VASP The Vienna *Ab initio* Simulation Package 15–17, 23, 24, 26, 27, 46, 52, 54

XC exchange and correlation 2, 10–12, 23